

THIRD QUARTERLY REPORT  
VAPOR-CHAMBER FIN STUDIES

prepared for  
National Aeronautics and Space Administration

April 1966

Contract NAS3-7622

Technical Management  
NASA Lewis Research Center  
Space Power System Division  
Nuclear Power Technology Branch  
Cleveland, Ohio  
Martin Gutstein

Written by

L. S. Langston

L. S. Langston, Asst. Proj. Engr.

A. Sherman

A. Sherman, Sen. Anal. Engr.

B. H. Hilton

B. H. Hilton, Anal. Engr.

Approved by

H. R. Kunz

H. R. Kunz, Program Manager

W. J. Lueckel

W. J. Lueckel, Chief, Space  
Power Systems

**Pratt & Whitney Aircraft**

DIVISION OF UNITED AIRCRAFT CORPORATION



EAST HARTFORD, CONNECTICUT

## FOREWORD

This report describes the work conducted from December 1, 1965 to February 28, 1966 by the Pratt & Whitney Aircraft Division of United Aircraft Corporation, East Hartford, Connecticut on Contract NAS3-7622, Exploratory Investigation of Vapor-Chamber Fin Concept for Space Radiators, for the Lewis Research Center of the National Aeronautics and Space Administration.

The work reported was conducted by H.R. Kunz, J. Barnes and the authors.



## TABLE OF CONTENTS

	<u>Page</u>
Foreword	ii
Table of Contents	iii
List of Figures	v
I. Summary	1
II. Introduction	2
III. Wicking Materials	3
A. Description of Wicking Materials	3
1. Sintered Screen Materials	3
2. Sintered Powder Materials	4
3. Sintered Fiber Materials	8
B. Properties of Wicking Materials	11
1. Porosity	11
2. Pore Size Distribution	13
3. Free-Flow Area Ratio	31
C. Porous Material Machining	34
D. Summary	37
IV. Wicking Rise Tests - Task 1	38
A. Objective	38
B. Description of Wicking Rise Apparatus	38
C. Wicking Rise Test Procedure	41
D. Test Results	42
E. Summary	61
V. Permeability Tests - Task 1	
A. Objective	62
B. Description of Permeability Apparatus	63
1. Wick Samples	63
2. Test Assembly	63
C. Test Results	63
D. Accuracy of Permeability Results	70
E. Summary	75

## TABLE OF CONTENTS (Cont'd)

	<u>Page</u>
VI. Wick Boiling Tests - Task 2	76
A. Objective	76
B. Description of Boiling Apparatus	76
1. Overall Design	76
2. Sample - Heater Assembly	76
3. Changes Since Last Report	79
4. Instrumentation	81
5. Power Supplies	83
6. Test Procedure	83
C. Test Results	83
1. Boiling Phenomena	83
2. Test Results	85
D. Summary	97
VII. Fin Studies - Tasks 3 and 4	100
A. Objective	100
B. Fin Operation	100
C. General Experimental and Design Considerations	101
D. Calculations Based on Analytical Model	107
VIII. Future Work	111
A. Task 1 - Wicking Studies	111
B. Task 2 - Boiling Studies	111
Appendix A - Test Procedure for Boiling Apparatus	112

## LIST OF FIGURES

<u>Number</u>	<u>Title</u>	<u>Page</u>	<u>Number</u>	<u>Title</u>	<u>Page</u>
1	Cross-Sectional View of 100-Mesh Sintered Nickel Screen Sample M8	5	30	Water Wicking Curve for Sintered Nickel Powder Sample M4	44
2	Top View of 100-Mesh Sintered Nickel Screen Sample M8	5	31	Water Wicking Curve for Sintered Nickel Powder Sample M5	45
3	Cross-Sectional View of Sintered Nickel Powder Sample M4	7	32	Water Wicking Curve for Sintered Nickel Powder Sample M6	45
4	Top View of Sintered Nickel Powder Sample M4	7	33	Water Wicking Curve for Sintered Nickel Screen Sample M7	46
5	Cross-Sectional View of Sintered Nickel Fiber Sample H1	9	34	Water Wicking Curve for Sintered Nickel Screen Sample M8	46
6	Top View of Sintered Nickel Fiber Sample H1	9	35	Water Wicking Curve for Sintered Nickel Screen Sample M9	47
7	Cross-Sectional View of Sintered Nickel Fiber Sample H12	10	36	Water Wicking Curve for Sintered Nickel Screen Sample M10	47
8	Top View of Sintered Nickel Fiber Sample H12	10	37	Water Wicking Curve for Sintered Nickel Fiber Sample H1	48
9	Pore Size Distribution Curve	16	38	Water Wicking Curve for Sintered Nickel Fiber Sample H2	48
10	Mercury Intrusion Porosimeter Curve for Sample H1	18	39	Water Wicking Curve for Sintered Nickel Fiber Sample H3	49
11	Mercury Intrusion Porosimeter Curve for Sample H2	19	40	Water Wicking Curve for Sintered Nickel Fiber Sample H4	49
12	Mercury Intrusion Porosimeter Curve for Sample H3	20	41	Water Wicking Curve for Sintered Nickel Fiber Sample H6	50
13	Mercury Intrusion Porosimeter Curve for Sample H6	21	42	Water Wicking Curve for Sintered Nickel Fiber Sample H7	50
14	Mercury Intrusion Porosimeter Curve for Sample M10	22	43	Water Wicking Curve for Sintered Nickel Fiber Sample H8	51
15	Mercury Intrusion Porosimeter Curve for Sample H11	24	44	Water Wicking Curve for Sintered Nickel Fiber Sample H9	51
16	Mercury Intrusion Porosimeter Curve for Sample H12	25	45	Water Wicking Curve for Sintered Nickel Fiber Sample H10	52
17	Mercury Intrusion Porosimeter Curve for Sample H13	26	46	Water Wicking Curve for Sintered Stainless Steel Fiber Sample H11	52
18	Mercury Intrusion Porosimeter Curve for Sample M2	27	47	Water Wicking Curve for Sintered Stainless Steel Fiber Sample H12	53
19	Mercury Intrusion Porosimeter Curve for Sample M4	28	48	Water Wicking Curve for Sintered Stainless Steel Fiber Sample H13	53
20	Mercury Intrusion Porosimeter Curve for Sample M6	29	49	Freon 113 Wicking Curve for Sintered Nickel Powder Sample M1	54
21	Mercury Intrusion Porosimeter Curve for Sample M8	30	50	Freon 113 Wicking Curve for Sintered Nickel Powder Sample M4	54
22	Cross-Sectional View of Sintered Nickel Fiber Sample H4 Cut by Grinding Method	35	51	Freon 113 Wicking Curve for Sintered Nickel Powder Sample M6	55
23	Cross-Sectional View of Sintered Nickel Fiber Sample H4 Cut by Electrical Discharge Method	35	52	Freon 113 Wicking Curve for Sintered Nickel Fiber Sample H1	55
24	Cross-Sectional View of Sintered Nickel Fiber Sample H4 Cut by Electrochemical Machining Method	36			
25	Wicking Apparatus with Samples Installed	39			
26	Wick Apparatus No. 2 without Samples	40			
27	Water Wicking Curve for Sintered Nickel Powder Sample M1	43			
28	Water Wicking Curve for Sintered Nickel Powder Sample M2	43			
29	Water Wicking Curve for Sintered Nickel Powder Sample M3	44			

## LIST OF FIGURES (Cont'd)

<u>Number</u>	<u>Title</u>	<u>Page</u>	<u>Number</u>	<u>Title</u>	<u>Page</u>
53	Freon 113 Wicking Curve for Sintered Nickel Fiber Sample H2	56	78	Planar Wick Vapor-Chamber Fin Model	100
54	Freon 113 Wicking Curve for Sintered Nickel Fiber Sample H3	56	79	Pressure of Saturated Vapor as Function of Temperature for Water and Freon 113	102
55	Freon 113 Wicking Curve for Sintered Nickel Fiber Sample H6	57	80	Condenser Heat Flux as Function of Fin Temperature and Sink Temperature for Radiation-Cooled Fin	103
56	Dimensions of Permeability Samples	64	81	Condenser Heat Flux as Function of Fin Temperature and Heat Transfer Coefficient for Convection-Cooled Fin	104
57	Schematic Diagram of Permeability Apparatus	65	82	Evaporator Heat Flux as Function of Fin Temperature and Condenser-Evaporator Area Ratio for Radiative Heat Transfer	105
58	Wick Friction Factor vs Flow Rate per Unit Area for Sintered Nickel Screen Samples	67	83	Evaporator Heat Flux as Function of Fin Temperature and Condenser-Evaporator Area Ratio for Convective Heat Transfer	106
59	Wick Friction Factor vs Flow Rate per Unit Area for Sintered Nickel Powder Samples	67	84	Condenser Length as Function of Condenser Heat Flux and Wick Properties. Computed from Equation (26)	109
60	Wick Friction Factor vs Flow Rate per Unit Area for Sintered Nickel Fiber Samples	68			
61	Wick Friction Factor vs Flow Rate per Unit Area for Sintered 430 Stainless Steel Fiber Samples	68			
62	Wick Friction Factor vs Temperature for Sintered Metal Wicks	70			
63	Wick Friction Factor for Sample M4 vs Flow Rate Using an Internal and External Sample Length	71			
64	Photograph and Sketch of Wick Permeability Sample Holder Showing Pressure Taps	72			
65	Cutaway View of Boiling Test Apparatus	77			
66	Wick Boiling Experimental Test Setup Showing Control Panel, Primary Tank, and Secondary Tank	78			
67	Boiling Test Sample M9. 150-Mesh Sintered Nickel Screen	80			
68	Boiling Apparatus during 45-Degree Angle Test	82			
69	Heat Flux and Heat Transfer Coefficient vs $\Delta T$ for Water at 14.7 psia Boiling on a Chromel C Wire 0.040 Inch in Diameter	84			
70	Flat-Plate Boiling Test Sample	87			
71	Heat Flux vs $\Delta T_{sat}$ for Horizontal Flat Plate	88			
72	Heat Flux vs $\Delta T_{sat}$ for 150-Mesh Sintered Nickel Screen	89			
73	150-Mesh Sintered Nickel Screen. Tests at Angle to Horizontal	92			
74	Heat Flux vs $\Delta T_{sat}$ for 50-Mesh Sintered Nickel Screen Sample M7	95			
75	Heat Flux vs $\Delta T_{sat}$ for Sintered Nickel Powder Wick Sample M2	96			
76	Comparison of Heat Flux vs $\Delta T_{sat}$	96			
77	Comparison of Heat Flux vs $\Delta T_{sat}$ for Wick Samples	98			

31939

## I. SUMMARY

This report describes the work completed during the third quarter of an experimental and theoretical program for the study of the vapor-chamber fin. This program consists of preliminary evaluation of the wicking ability, permeability, and boiling characteristics of various porous metallic materials, followed by the testing of vapor-chamber fins using materials found to have the most promising capillary properties. The data from the fin tests will enable analytical models of fin performance to be evaluated, using the measured characteristics obtained in the preliminary tests. During the third quarter the wicking rise tests were completed, the permeability and boiling tests were continued, and fin design work was started.

Twenty-three porous metal samples were studied. The porosity and free-flow area ratio of each of these samples was determined, as well as the pore size distribution of twelve of the twenty-three samples.

Wicking rise tests were conducted on twenty-two of the samples, using water and Freon 113. The equilibrium height of the water front was found to vary from 2.10 inches in a sintered screen sample to 21.0 inches in a sintered powder sample. Equilibrium heights with Freon 113 were lower, due primarily to its lower surface tension.

The wick friction factor of thirteen of the twenty-three samples was measured in permeability tests utilizing water. This factor was found to be independent of flow rate for low flow rates, and independent of liquid temperature.

The boiling heat transfer characteristics of a flat plate, two sintered screen samples and a sintered powder sample were measured. All three of the porous samples had lower heat transfer coefficients than the flat plate. This was attributed to the premature occurrence of film boiling, caused by the entrapment of vapor bubbles in the wick matrix.

Preliminary design work was conducted on experimental models of the vapor-chamber fin. The upper limit on internal fin pressure was set at 150 psia, corresponding to a maximum fin temperature of 358°F for water and 288°F with Freon 113. A convectively-cooled fin model was found to have definite advantages over a fin model cooled by radiation. These advantages include a smaller fin size and a wider range of heat fluxes.

*Author*

## II. INTRODUCTION

The present program to investigate the operation of the vapor-chamber fin is divided into a study of basic properties of wicking materials and a study of the vapor-chamber fin itself.

This third quarterly report deals with the measurement and interpretation of various properties of wicking materials, and with the preliminary design of an experimental model of the vapor-chamber fin.

The properties of the wicking materials under consideration are described in Sections III to VI. Included in these sections is a discussion of the geometric properties, the wicking ability, the permeability, and the boiling heat transfer characteristics of porous materials. Preliminary design work on experimental models of vapor-chamber fins is treated in Section VII. Future work is outlined in Section VIII.

### III. WICKING MATERIALS

#### A. Description of Wicking Materials

A wick can be defined as a porous material whose pores are of such size that a liquid can be moved through it by the action of capillary forces. The pores must also be highly interconnected rather than separate and discrete. The pore sizes should fall into a range where a favorable balance exists between the capillary forces and the frictional forces associated with the motion of a liquid.

The wicking materials considered in this study for use in vapor-chamber fins were narrowed down to three classes of metallic porous materials. They are:

- 1) sintered screen materials
- 2) sintered powder materials
- 3) sintered fiber materials

The reasons for selecting these materials were given in the first quarterly report<sup>1</sup>, and include ease of fabrication, dimensional stability, isotropy and thermal conductivity.

The following is a detailed description of each class of porous material.

#### 1. Sintered Screen Materials

The four sintered screen samples that have been studied are listed in Table 1.

TABLE 1

Sintered Screen Samples

<u>Sample No.</u>	<u>Material</u>	<u>Mesh Size, (wires per inch)</u>	<u>Wire Diameter, inches</u>
M7	nickel	50	0.0090
M8	nickel	100	0.0045
M9	nickel	150	0.0030
M10	nickel	200	0.0022

<sup>1</sup>First Quarterly Report, Vapor-Chamber Fin Studies, NASA CR-54882, PWA-2698, Contract NAS3-7622, September 1965

The sintered screen samples consist of layers of nickel screen that have been pressed against a nickel foil backing and sintered together at points of contact in a furnace with an ammonia atmosphere. The mesh referred to is the number of wires per linear inch in either the warp wire direction or the woof wire direction. The wire diameter given is that of both the warp and woof wires.

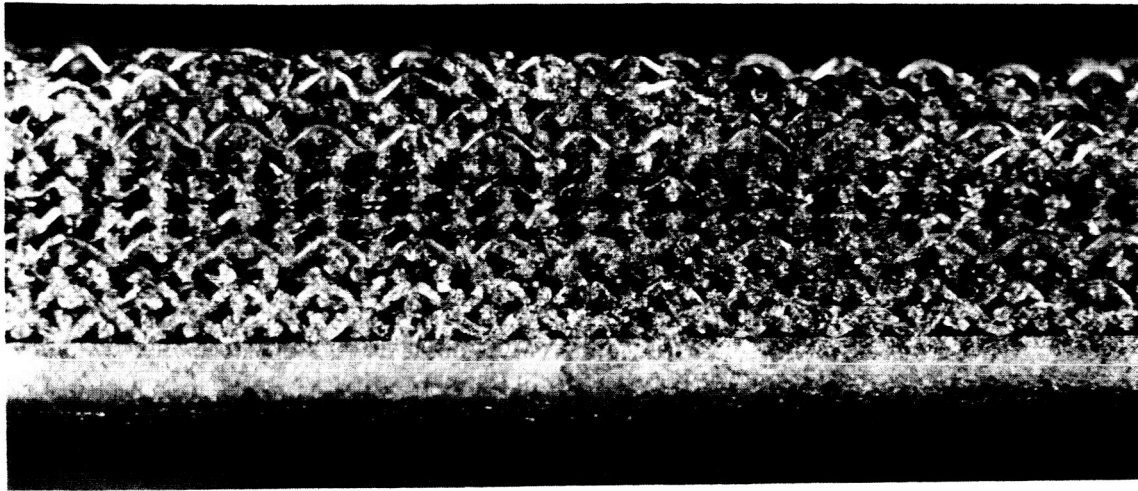
A typical screen sample (in this case 100 mesh) is shown in cross-section in Figure 1 and in plan in Figure 2. The solid structure at the bottom of the sample in Figure 1 is the nickel backup foil to which the screens are sintered. The porous material of this sample is 0.0675 inch thick and the backup foil is 0.0248 inch thick. These photomicrographs exhibit a number of features of sintered screens as porous materials. For instance, as the screens are stacked in Figure 1, it would probably be incorrect to characterize the pore size of the material based solely on the spacing of the wires in one layer of screen. The photomicrographs show that screen layers (at least in the two top layers) are stacked in such a way that alternate layers are displaced from one another by one-half a wire spacing. This means that wherever there is a square opening (or pore) formed by two warp and two woof wires in one screen layer, there is a crimped wire elbow protruding into the center of the opening from the screen layer immediately below the first. This results in a smaller pore size and a denser structure. Also noteworthy is the lack of any relatively large pores that are continuous from the backup foil to the free surface of the porous material.

Comparison of Figures 1 and 2 also shows that sintered screen samples are not strictly isotropic. However, because of the interlocking of the screen layers, (i. e., the displaced stacking discussed above) the departure from isotropy is not great.

## 2. Sintered Powder Materials

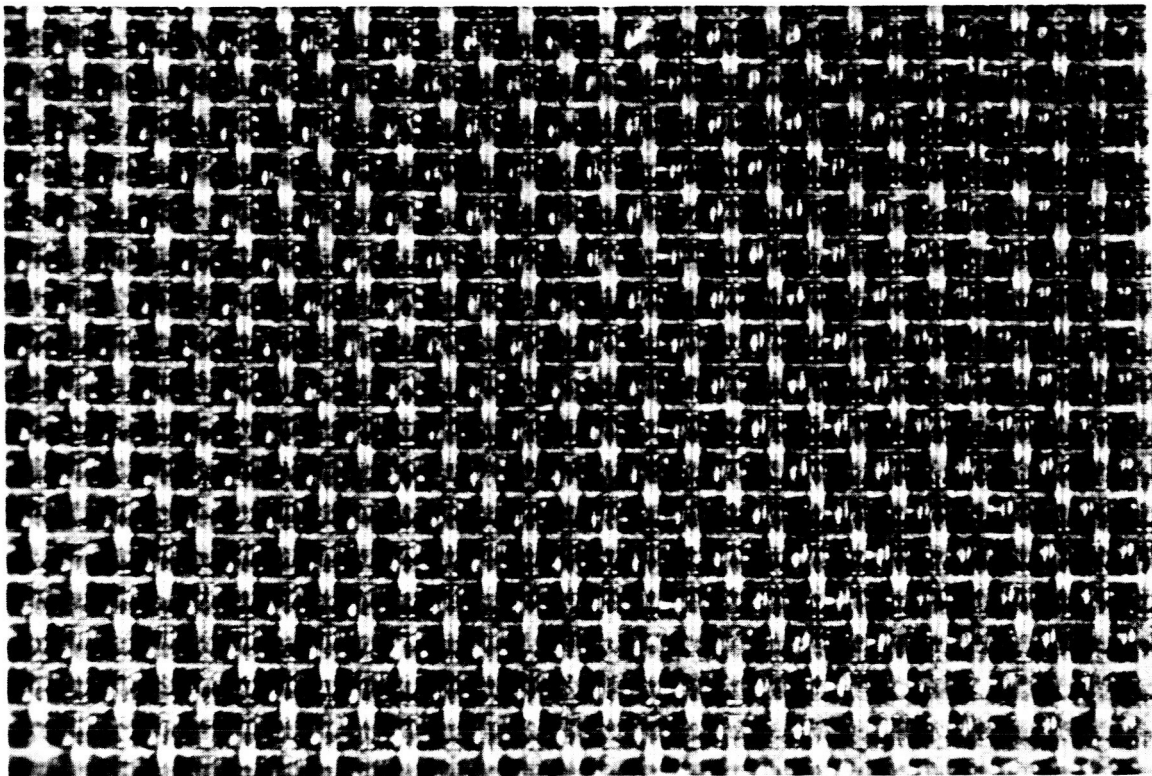
The six sintered nickel powder samples investigated are listed in Table 2.





Mag: 21X

Figure 1 Cross-Sectional View of 100-Mesh Sintered Nickel Screen Sample M8



Mag: 21X

Figure 2 Top View of 100-Mesh Sintered Nickel Screen Sample M8

TABLE 2

## Sintered Powder Samples

<u>Sample No.</u>	<u>Material</u>	<u>Powder Size Range, Microns</u>
M1	nickel	150-297
M2	nickel	150-297
M3	nickel	297-841
M4	nickel	297-841
M5	nickel	297-841
M6	nickel	297-841

As described in the second quarterly report<sup>1</sup>, these porous materials are constructed of an irregular nickel powder. The samples were made by compressing the nickel powder against a nickel backup foil, using a die. This "green" material was then placed in a furnace with an ammonia atmosphere, where the nickel powder was sintered to itself and to the nickel backup foil.

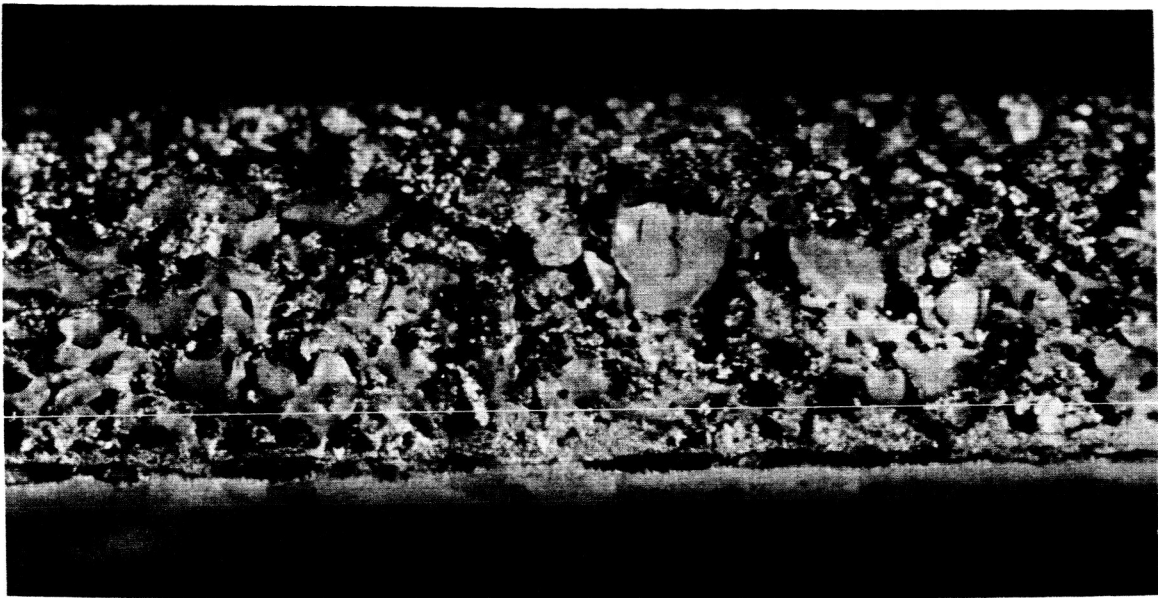
One of the sintered powder samples, M4, is shown in cross-section in Figure 3 and in plan in Figure 4. The solid structure at the bottom of the sample in Figure 3 is the nickel backup foil. The porous sintered nickel powder is 0.0873 inch thick and the nickel backup foil is 0.0248 inch thick.

The irregularity of the pore structure shown in Figures 3 and 4 is in contrast to the relatively regular structure exhibited by the sintered screen samples. At some locations the powder seems to have melted in sintering and coalesced into large globules.

The range of pore sizes is apparently greater in Sample M4 than for the sintered screens. As shown in Figure 4, the pores on the surface range from voids of dimensions comparable to the diameter of the smallest powder used, to large voids that could more aptly be termed craters. Figure 3 also shows that there is a significant number of large interconnected pores of relatively low tortuosity running from the backup foil to the free surface of the porous material. Such a pore geometry is necessary for good boiling heat transfer characteristics, as will be shown in Section VI.

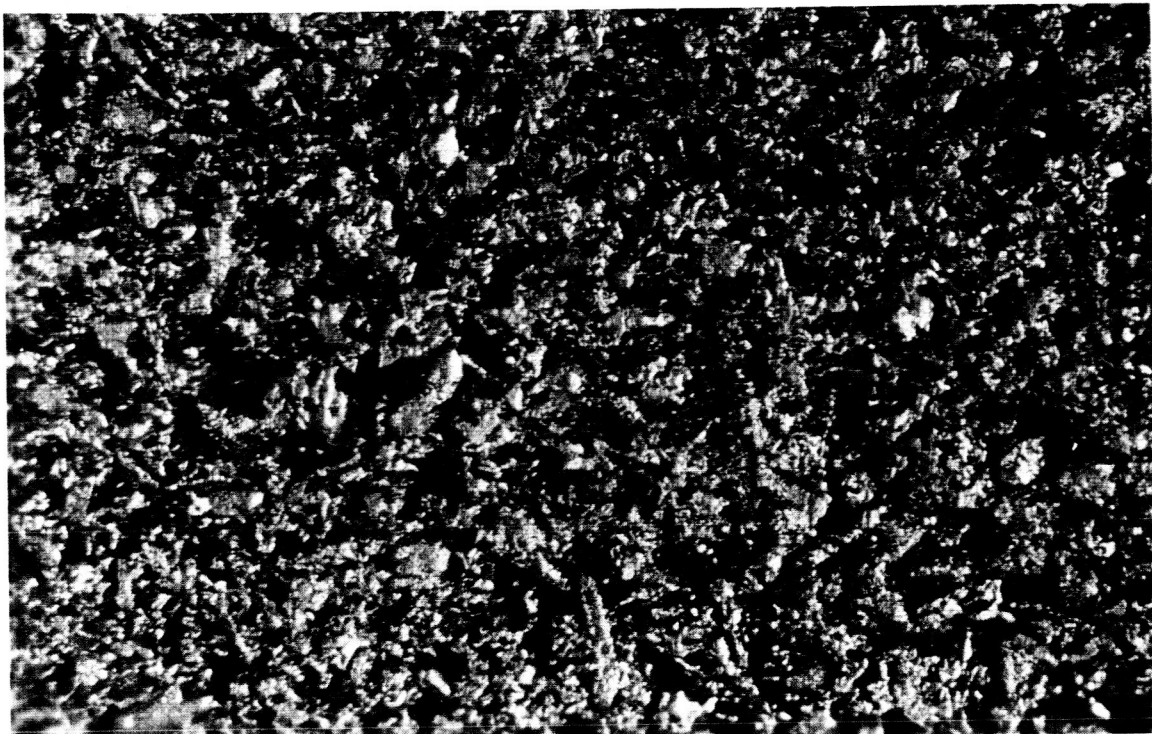
---

<sup>1</sup>Second Quarterly Report, Vapor-Chamber Fin Studies, NASA CR-54922, PWA-2773, Contract NAS3-7622, January 1966



Mag: 21X

Figure 3 Cross-Sectional View of Sintered Nickel Powder Sample M4



Mag: 21X

Figure 4 Top View of Sintered Nickel Powder Sample M4

### 3. Sintered Fiber Materials

The thirteen sintered metal fiber samples studied are listed in Table 3.

TABLE 3  
Sintered Fiber Samples

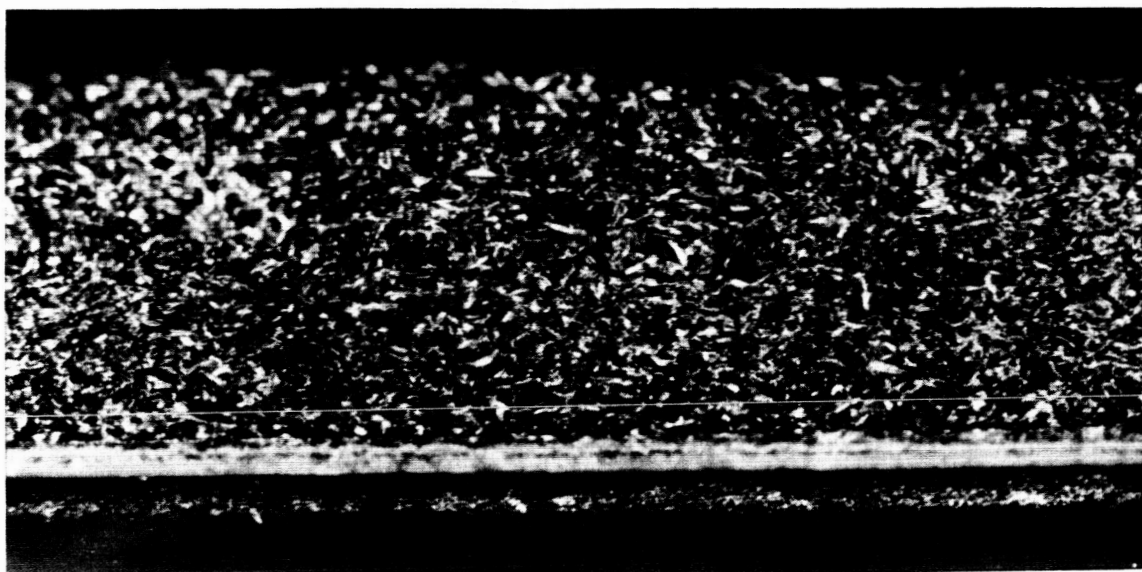
<u>Sample No.</u>	<u>Material</u>	<u>Mean Fiber Diameter, Inches</u>
H1	nickel	0.0004
H2	nickel	0.0004
H3	nickel	0.0004
H4	nickel	0.0004
H5	nickel	0.0006
H6	nickel	0.0006
H7	nickel	0.0006
H8	nickel	0.0006
H9	nickel	0.0006
H10	nickel	0.0006
H11	430 stainless steel	0.0013
H12	430 stainless steel	0.0013
H13	430 stainless steel	0.0030

As shown in the table, these sintered fiber samples were made from nickel or stainless steel. In each case the backup foil to which the porous material is sintered was the same material as the porous structure.

The metallic fibers making up the porous material had a length-to-diameter ratio in the range of 10 to 1000. The fibers were felted to produce a randomly interlocked structure. The latter was pressed against a backup foil and then sintered in a controlled-atmosphere furnace to produce bonds at points where the fibers touch one another and the foil backing.

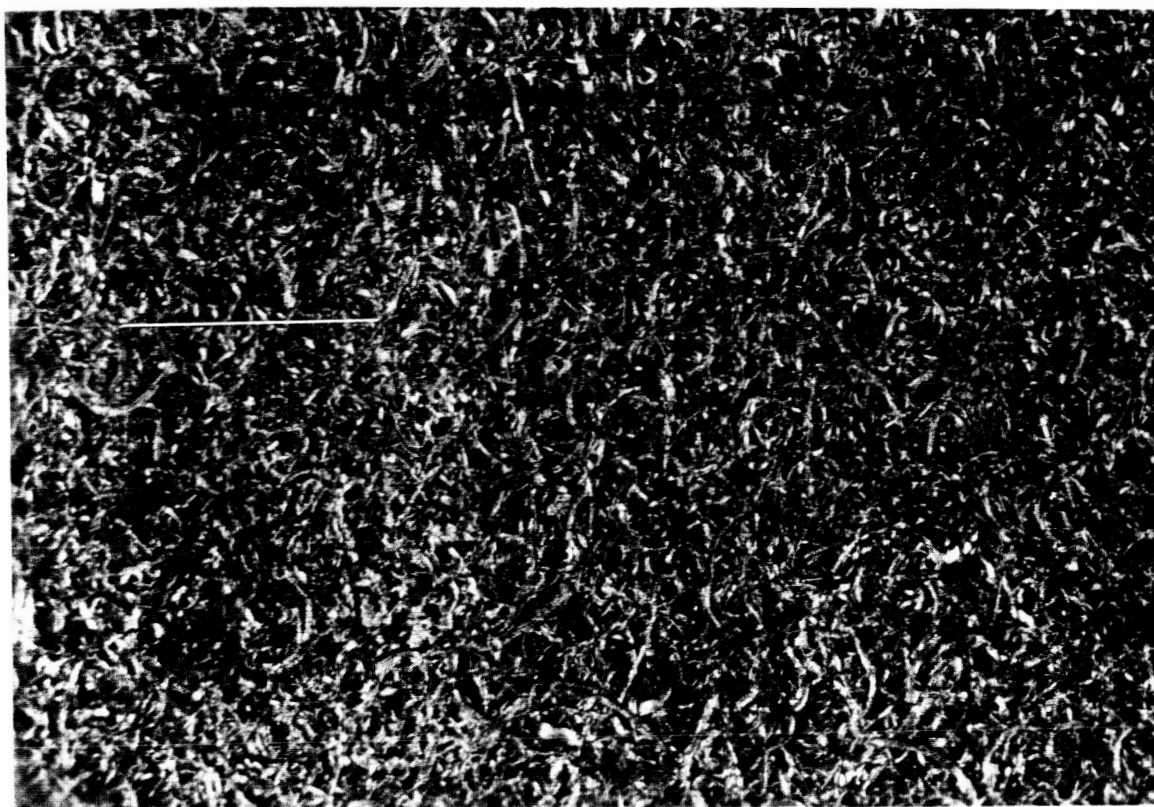
A sintered nickel fiber sample, H1, is shown in cross-section in Figure 5 and in plan in Figure 6. The nickel fiber structure is 0.0825 inch thick and the nickel backup foil is 0.0218 inch thick.

Photomicrographs of a sample (H12) composed of stainless steel fibers of a much larger diameter are shown in Figures 7 and 8. In this case, the stainless steel fiber structure shown is 0.0991 inch thick and the stainless steel backup foil is 0.0218 inch thick.



Mag: 21X

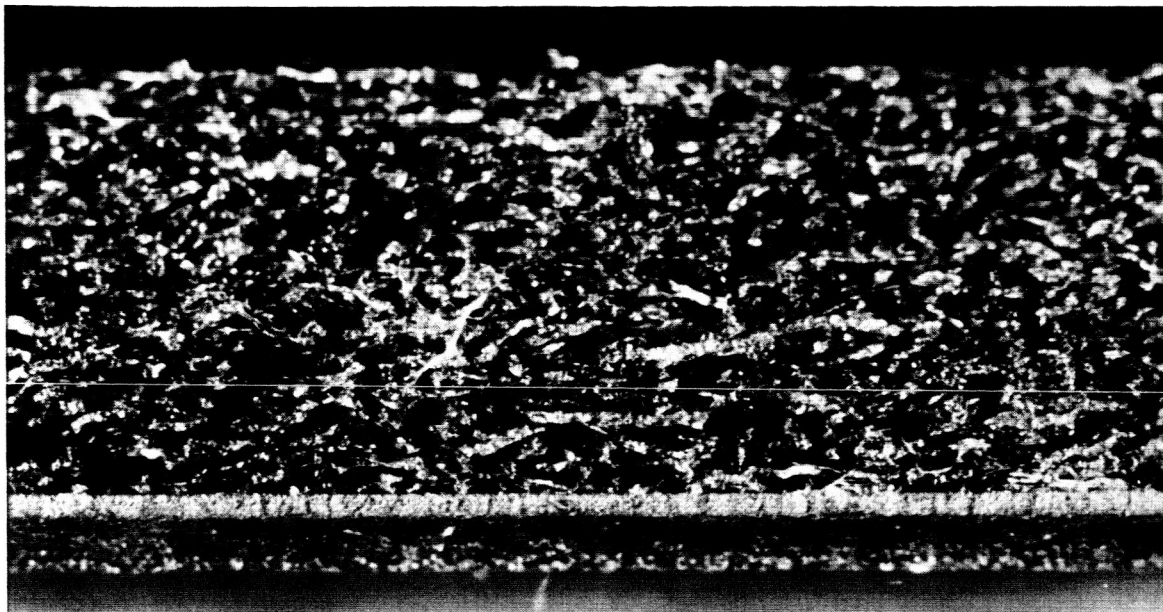
Figure 5 Cross-Sectional View of Sintered Nickel Fiber Sample H1



Mag: 21X

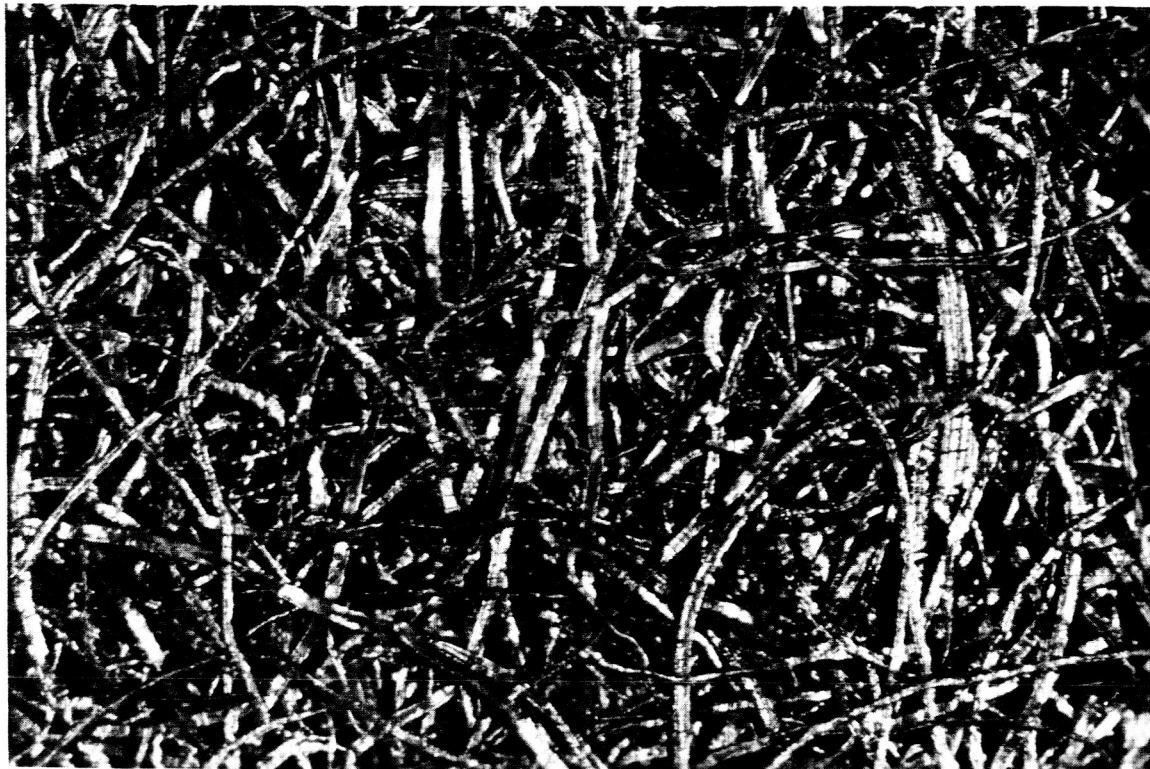
Figure 6 Top View of Sintered Nickel Fiber Sample H1





Mag: 21X

Figure 7 Cross-Sectional View of Sintered Nickel Fiber Sample H12



Mag: 21X

Figure 8 Top View of Sintered Nickel Fiber Sample H12

An examination of the photomicrographs in Figures 5 through 8 shows that there is an abundance of pores present in the fiber mat. In addition, there is a large degree of interconnectiveness associated with the pore structure. Because of their structure the sintered fiber metals offer the widest range of pore sizes and porosity of any of the porous materials that have been considered so far.

## B. Properties of Wicking Materials

Knowledge of the porosity and the way in which the pore space is distributed through a porous solid is essential to any study of porous material. A description of the quantities necessary to evaluate the porosity, the pore size distribution, and the free-flow area ratio is presented in the following sections.

### 1. Porosity

The porosity  $\epsilon$  of a material is defined as the total pore volume of a sample divided by the total volume of the sample itself. Thus a porosity of zero per cent denotes a solid substance containing no pores or voids, while one of 100 per cent denotes a complete void. While the porosity accounts for all pores or voids in a sample, the effective porosity is based upon the interconnected (as opposed to separate or noninterconnected) pore space within the sample.

The study of the flow of a fluid through a pore system in a material should be based on the effective porosity rather than the porosity. By examining Figures 1, 2, 5 and 6 it can be seen that the pores of both the sintered screens and the sintered fibers are for the most part interconnected. Thus the effective porosity of each of these materials can be taken as equal to the porosity.

The powders used in making the sintered powder samples were composed of solid particles that contained no voids. However, in compacting the powder, isolated voids can form. This compacting was kept to a minimum during the fabrication of the sintered powder samples, represented by Figures 3 and 4, by compressing the powder before sintering as little as possible. Thus, in all samples considered in this study, the effective porosity will be taken as equal to the porosity  $\epsilon$ .

The porosity of each of the samples described in Section III. A. was measured and is tabulated in Table 4.

TABLE 4

## Porosity of Porous Material Samples

	<u>Sample No.</u>	<u>Porosity, %</u>		<u>Sample No.</u>	<u>Porosity, %</u>
Sintered Powder Samples	M1	59.7	Sintered Fiber Samples	H1	86.8
	M2	65.8		H2	82.5
	M3	47.7		H3	68.9
	M4	54.0		H4	62.8
	M5	69.1		H5	91.8
	M6	69.6		H6	88.0
Sintered Screen Samples	M7	62.5		H7	82.0
	M8	67.9		H8	82.8
	M9	67.8		H9	62.6
	M10	67.6		H10	70.9
				H11	91.6
				H12	80.8
				H13	82.2

In calculating the porosity values listed in Table 4 the basic definition of porosity was used in the form

$$\epsilon = \frac{V_T - W_T / \rho_s}{V_T} \quad (1)$$

where  $V_T$  = total volume of the porous region of the sample

$W_T$  = total weight of the porous region of the sample

$\rho_s$  = density of the solid (8.90 gm/cc for nickel and 7.70 gm/cc for 430 stainless steel)

The weight of each sample was determined by using a triple-beam balance, while the volume was determined by taking many measurements of the dimensions of each sample with micrometers. In all measurements and computations, the fact that the samples were backed with a solid nickel or stainless steel foil was taken into account. Confidence intervals were calculated for each porosity measurement. The maximum uncertainty (confidence interval based on odds of 20 to 1) for any of the sintered screen samples was calculated to be  $\pm 2.6$  per cent while that of the sintered powder and sintered fiber samples was  $\pm 1.3$  per cent. These measured porosity values not only provide a measure of the total pore space in a given sample, but also tell something about the structure of the porous material. For instance, if the sintered powder samples were composed of perfectly spherical



powders, the maximum porosity that each sample could have would be 47.84 per cent. However, the substantially higher values of porosity listed in Table 4 show that the combined effect of irregular powders and loose packing lead to a structure that is less dense than an equivalent spherical packing.

The maximum porosity that a perfectly stacked screen structure can assume was calculated in the second quarterly report to be about 61 per cent. This configuration was termed a square stacking. The measured porosity values of Table 4, ranging from 62.5 to 67.9 per cent, indicate that the screen samples in this study probably approximate the square stacking. Although Figure 1 shows that many of the layers follow the square configuration, there are many layers that are much more closely stacked. The higher porosity values that were measured indicate that some of the screen layers may be imperfectly sintered, thus producing a greater void volume in the sample.

The sintered fibers have a much higher porosity than the other two classes of porous material, due to their structure. In one case the randomly interlocked fiber structure produced a porosity of 91.8 per cent. This is about the practical upper limit on rigid sintered fiber materials, for this sample (H5) tended to deform easily. The porosity of any of these samples, be they sintered screen, powder, or fiber, could be decreased by rolling and compressing the sample.

## 2. Pore Size Distribution

The manner in which the pore space is distributed in a porous material is given by the pore size distribution function. This function,  $\alpha(r)$ , is defined by the equation

$$dV = - \alpha(r)dr \quad (2)$$

where  $dV$  is the volume of the pores with radius between  $r$  and  $r + dr$ . For purposes of the following discussion,  $V$  itself will be defined as the volume of all pores with radius equal to or greater than  $r$ .

The porous materials described in Section III. A. have pore diameters falling in the range of 0.1 to 1000 microns. For this range of pore diameters the best method available for determining the pore size distribution function is to use a mercury intrusion porosimeter. This instrument employs the injection of non-wetting mercury into the pore system of a sample, and recording the pressure necessary to accomplish the injection. By measuring the volume of the mercury in the porous material as a function of

pressure, the pore size distribution can be calculated. An explanation of the operation of the device is presented in the following paragraphs.

When a liquid is introduced into the pore system of a porous material, the liquid will form menisci whose curvature is determined by the shape and size of the pores in the material. If the liquid is a non-wetting fluid such as mercury, a positive pressure will be necessary to force the liquid into the pore system. For a given size of pore, this positive pressure is given by the Laplace - Young equation

$$\Delta P = \sigma \left( \frac{1}{R_1} + \frac{1}{R_2} \right)$$

where  $\Delta P$  is the pressure drop across the liquid-vapor interface,  $\sigma$  is the liquid-vapor surface tension, and  $R_1$  and  $R_2$  are the two principle radii of curvature necessary to describe the liquid-vapor interface. If the pore system has been evacuated prior to the introduction of the liquid and if the vapor pressure of the liquid is small (e.g., mercury at room temperature), then

$$P \approx \Delta P \quad (3)$$

where  $P$  is the pressure of the liquid.

It is assumed here that  $R_1$  and  $R_2$  completely describe the entire liquid-vapor interface in the pore. Up to now the terms pore radius and pore diameter have been used without precise definition. An examination of the photomicrographs, Figures 1 to 8, shows that it would be quite unrealistic to assume that the pores are cylindrical in the materials under study. Their pore shape and structure are quite irregular. However an equivalent pore radius can be defined as

$$r_e = 2 \left( \frac{\text{cross-sectional area of pore}}{\text{perimeter of pore}} \right) \quad (4)$$

In fluid mechanics terminology this equivalent pore radius can also be called a hydraulic radius. As  $r_e$  is defined, Equation (4) reduces to the radius of a cylinder for the case of a cylindrical pore. Hereafter the term pore radius and  $r$  will be taken as equivalent to the definition given by Equation (4).

Using Equation (3), a force balance on the miniscus in the pore yields

$$(F_\sigma) (\text{perimeter of pore}) = (P) (\text{cross-sectional area of pore}) \quad (5)$$

where  $F_\sigma$  is the surface tension force per unit length of interfacial

boundary. The latter is given by

$$F_{\sigma} = \sigma \cos \theta \quad (6)$$

where  $\sigma$  is the surface tension and  $\theta$  is the contact angle.

Combining Equations (4) and (5) yields

$$Pr = 2 \sigma \cos \theta \quad (7)$$

For constant values of surface tension and contact angle, this equation directly relates  $r$ , the pore radius, to  $P$ , the measured pressure necessary to force the non-wetting liquid (in this case mercury) into the pore. It should be noted that the expression is independent of the measured volume of liquid,  $V$ . If  $\theta$  and  $\sigma$  are constant, Equation (7) can be differentiated to obtain

$$rdP + Pdr = 0 \quad (8)$$

By combining Equations (2), (7) and (8) an expression for the pore size distribution function is obtained

$$\alpha(r) = \frac{P^2}{(2 \sigma \cos \theta)} \frac{dV}{dP} \quad (9)$$

- where
- $\alpha(r)$  = pore size distribution function
  - $P$  = pressure required to force mercury into evacuated pores of radius  $r$
  - $V$  = volume of all pores in the sample with radius equal to or greater than  $r$
  - $\sigma$  = surface tension
  - $\theta$  = contact angle

Thus to evaluate  $\alpha(r)$  for a given porous material, both  $P$  and  $V$  must be measured. This is done with the mercury intrusion porosimeter by measuring the pressure  $P$  necessary to force a given volume  $V$  of mercury into the evacuated sample. Knowing this,  $\alpha(r)$  can be calculated from Equation (9) and  $r$  can be found from Equation (6), where  $\sigma$  is taken to be 473 dynes/cm for mercury and the contact angle is 130 degrees. The latter value has been found to be valid for most mercury-metal systems. The derivative  $dV/dP$  is calculated by taking the slope of a plot of  $P$  vs  $V$ .

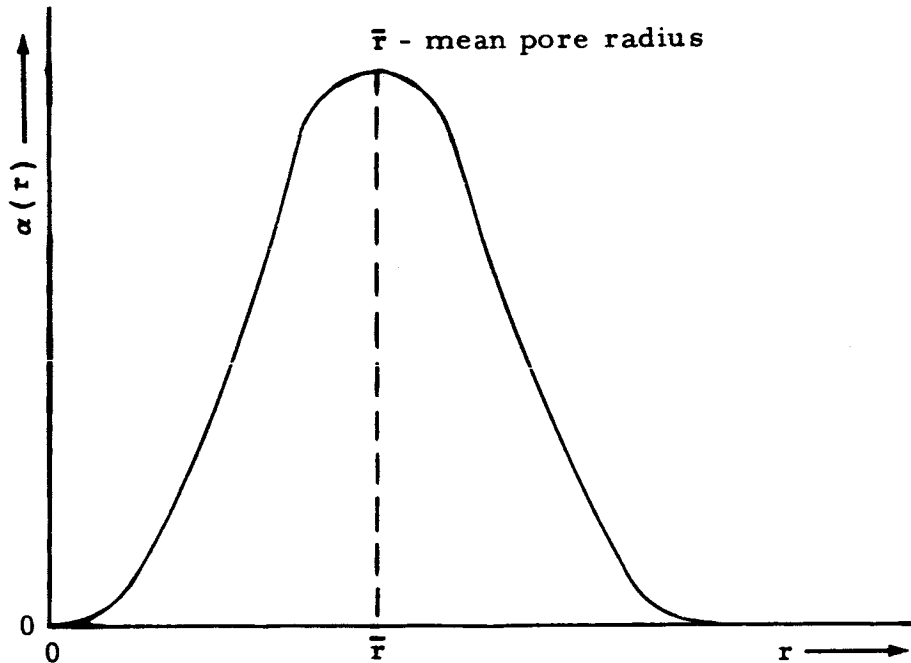


Figure 9 Pore Size Distribution Curve

A typical pore size distribution curve is shown in Figure 9, where  $\bar{r}$  is defined as the mean pore radius, i. e., the pore size that occupies more of the total pore volume than any other pore size. It should also be noted that as defined,  $\alpha(r)$  is dependent on the actual size of the sample.

The V-P data necessary to calculate  $\alpha(r)$  was obtained for twelve of the most promising porous material samples described in Section III. A. These were samples H1, H2, H3, H6, H10, H11, H12, H13, M2, M4, M6, and M8. At least two pieces of each porous material sample were tested in a mercury intrusion porosimeter made by the American Instrument Company. Each sample was placed in the porosimeter container which was evacuated before the mercury was introduced into the sample. All samples were cleaned using the procedure outlined in the Section IV. C. The most complete V-P curve for each of twelve samples is shown in Figures 10 through 21. These plots show volume as a function of pressure and volume as a function of pore diameter. From Equation (7) the pore diameter is given by

$$D = \frac{4 \sigma \cos \theta}{P} \quad (10)$$

where

- $D$  = diameter of pore, i. e. , twice the pore radius  
given by Equation (4)
- $P$  = Pressure required to force mercury into a pore  
of diameter  $D$
- $\sigma$  = surface tension of mercury = 473 dynes/cm
- $\theta$  = contact angle between mercury and solid material =  
130 degrees

Figures 10 through 21 present essentially the same information that a plot of the pore size distribution would show, for they illustrate the measurable range of pore sizes in each sample and the volume occupied by each pore size. To replace the mean pore radius  $\bar{r}$  in Figure 9, the median pore diameter has been chosen to characterize the pore space of each sample. The median pore diameter  $D_{med}$  is defined as the pore size at which 50 per cent of the connected pore space is filled with mercury. From the V-P curve it can be seen that the value of  $D_{med}$  does not differ significantly from the value of the mean pore diameter. Both occur in the region of maximum slope of the V-P curve.

Fairly complete pore spectra were obtained for samples H1, H2, H3, H6 and M10, with pore diameters falling between 0.5 and 100 microns (Figures 10 to 14). These samples were four of the sintered fiber samples of finest fiber and one sintered powder sample. The range of pore sizes that occupies the greatest portion of the total pore volume occurs in the region of the maximum slope of the V-P curve. For sample H3 (Figure 12) this portion of the total volume occurs for pore sizes between 15 and 35 microns. For this sample the median pore diameter  $D_{med}$  can be calculated by noting that at a pore volume of 0.08 cc (equal to 50 per cent of the connected pore volume) the pressure as read from the V-P curve of Figure 12 is about 6.6 psia. Using Equation (10), or using the pore diameter scale in Figure 12,  $D_{med}$  is found to be 26.5 microns. Figure 12 also shows that the pore diameters ranging from 10 to 35 microns contain 90 per cent of the connected pore volume of the sample. Similar conclusions can be drawn from Figures 10, 11, 13, and 14.

Because of the construction of the mercury intrusion porosimeter, pressures less than 2.5 psia could not be read. This pressure, using Equation (10), corresponds to a pore size of 70 microns. Thus, if a sample had pore structure in which most of the pore space was contained in pores of diameter greater

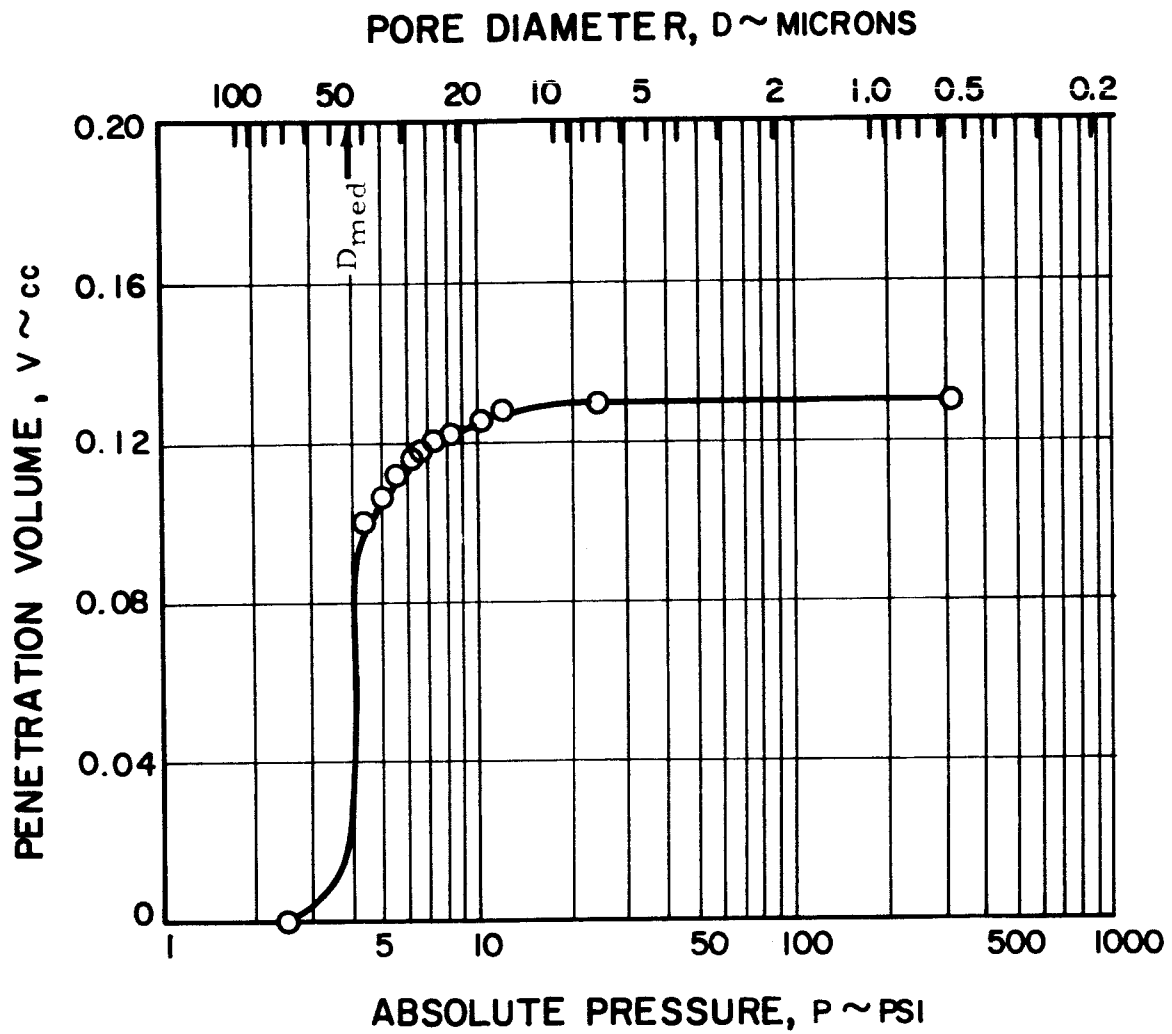


Figure 10 Mercury Intrusion Porosimeter Curve for Sample H1

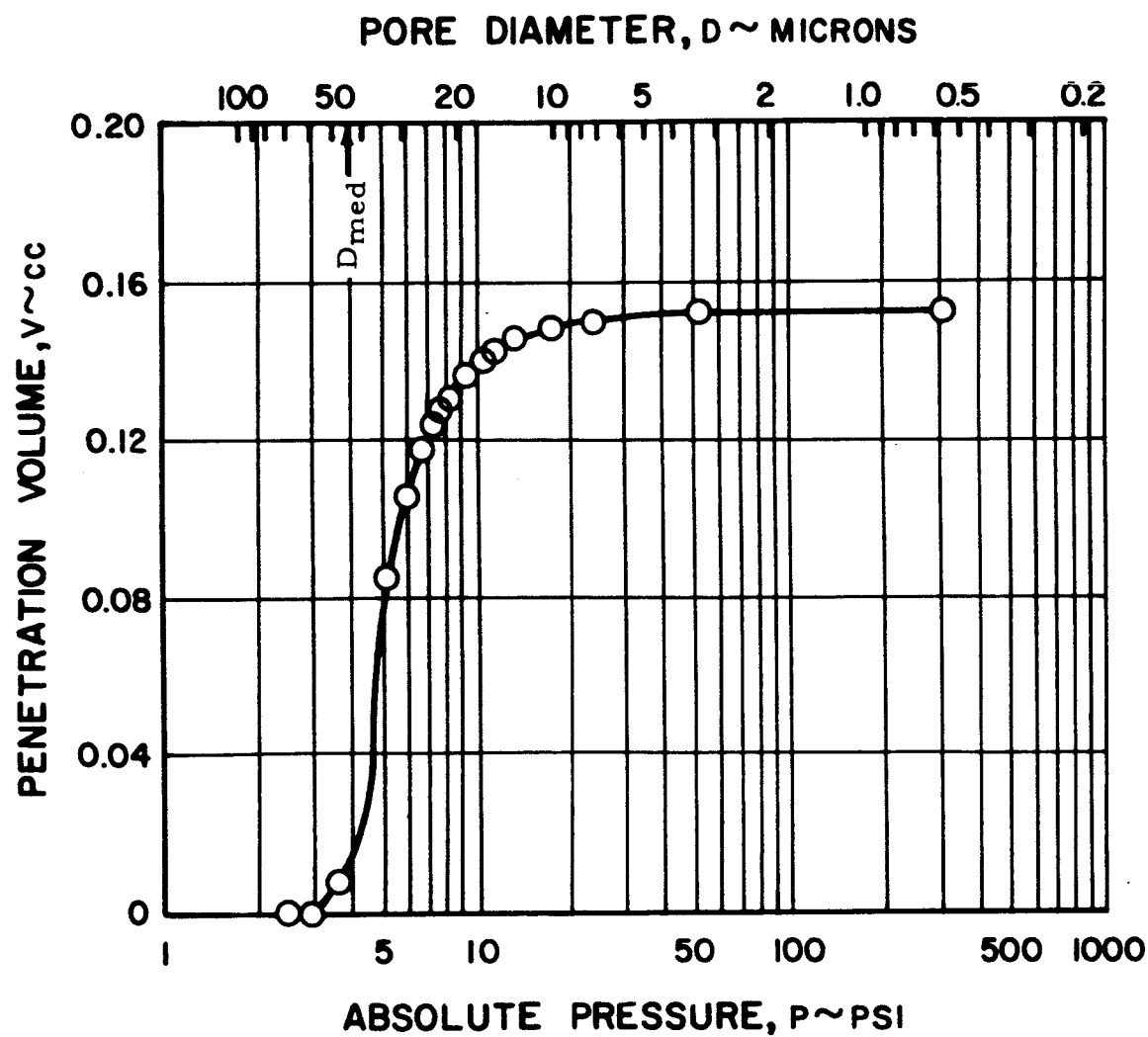


Figure 11 Mercury Intrusion Porosimeter Curve for Sample H2

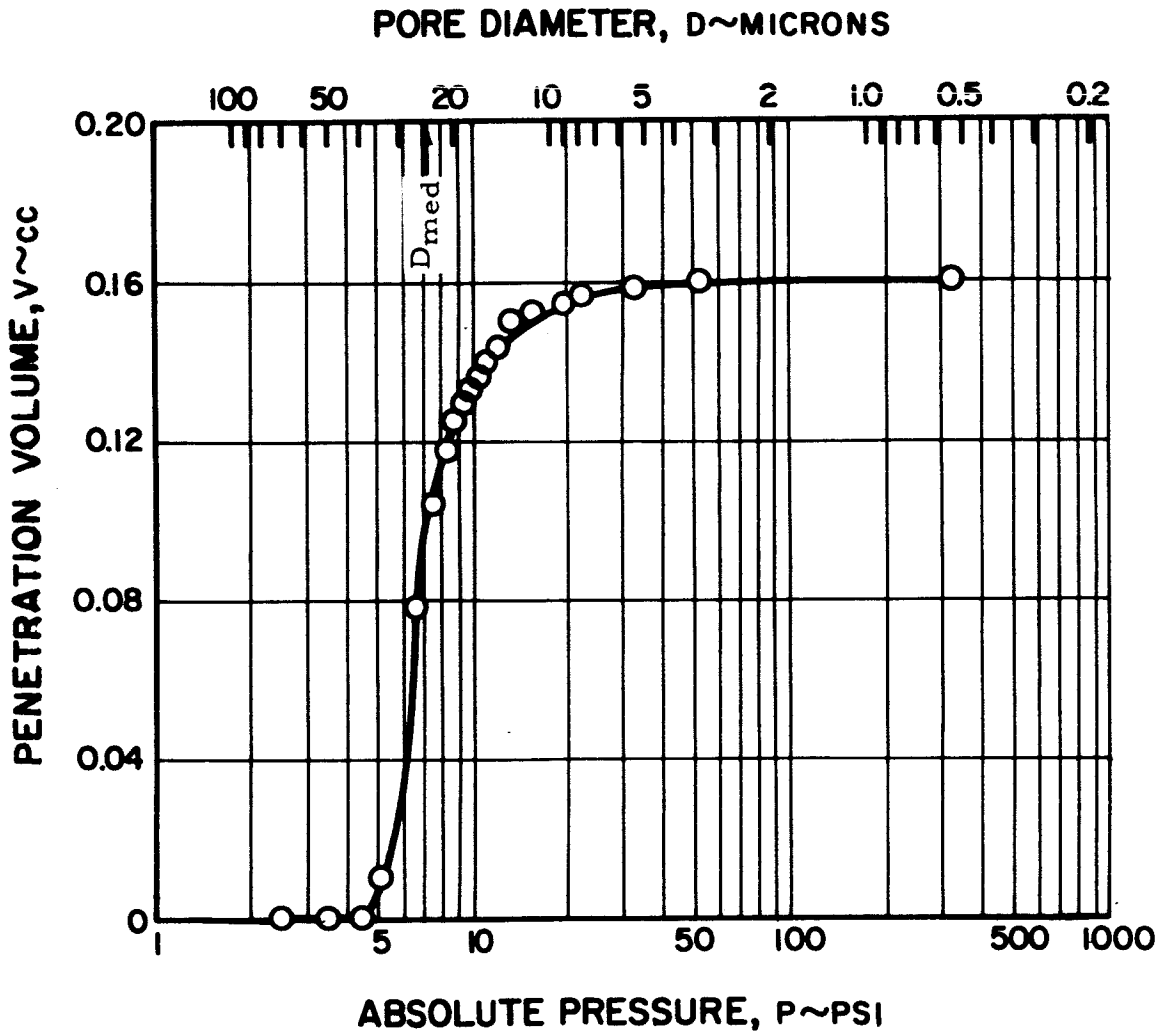


Figure 12 Mercury Intrusion Porosimeter Curve for Sample H3



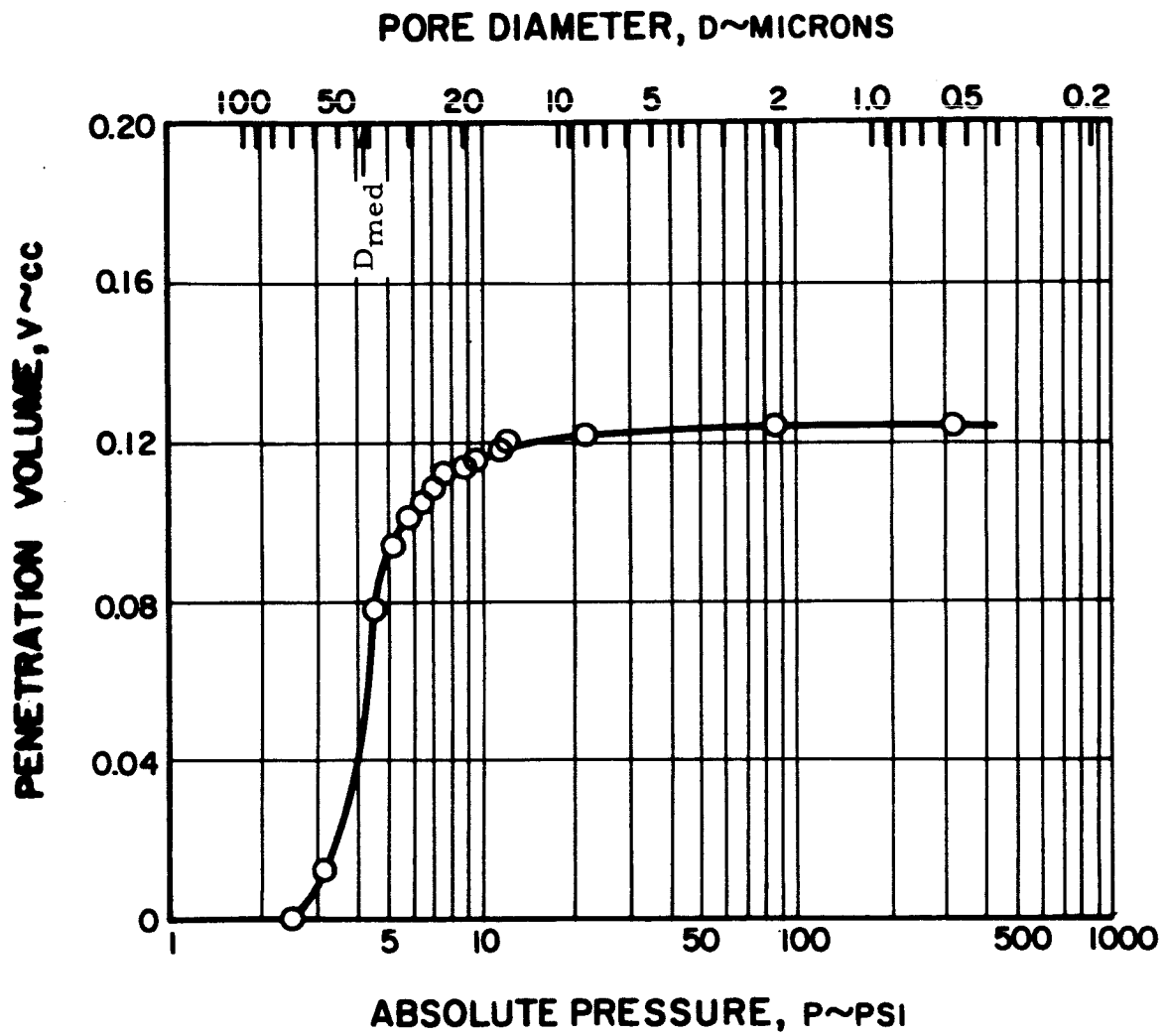


Figure 13 Mercury Intrusion Porosimeter Curve for Sample H6

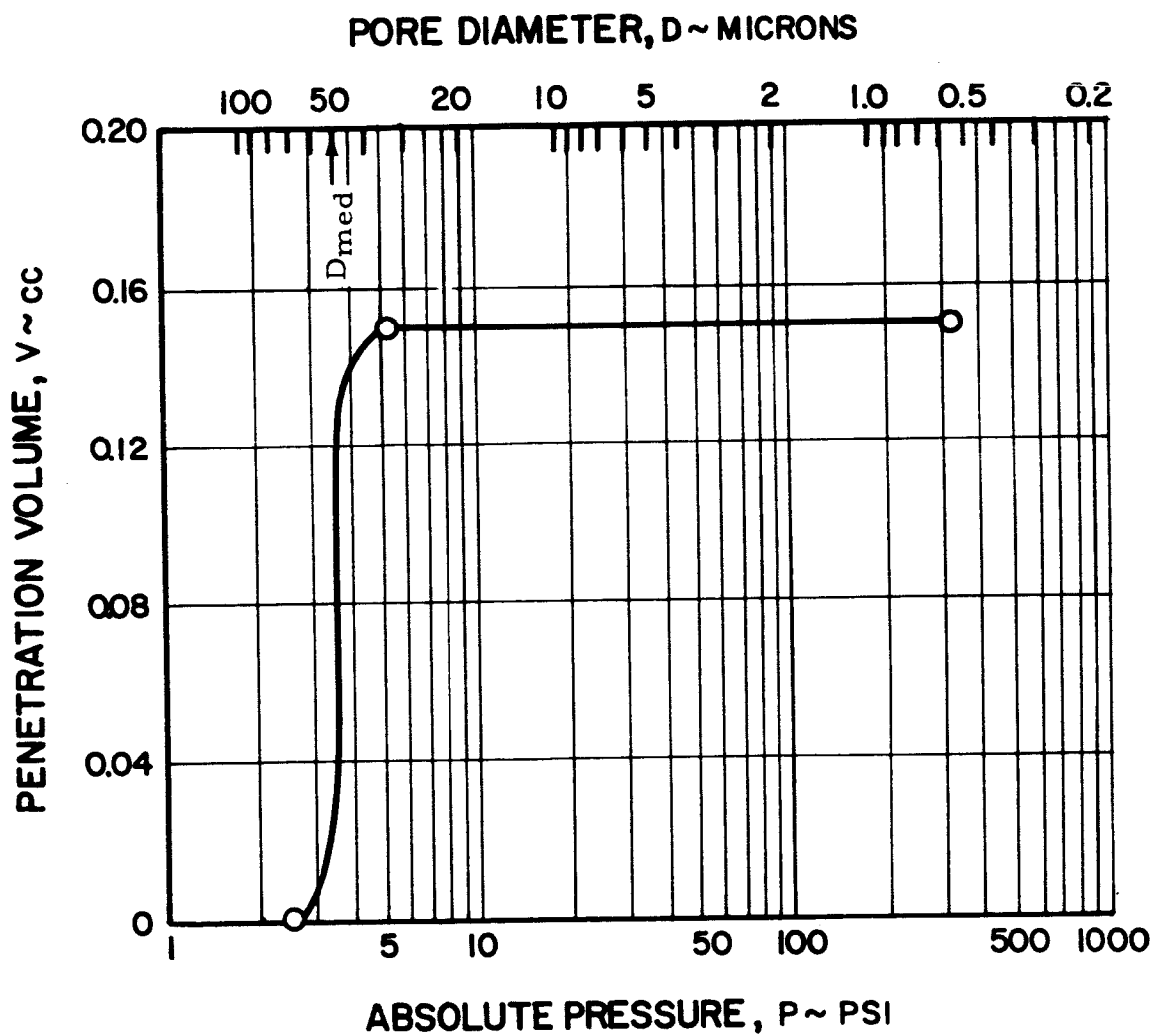


Figure 14 Mercury Intrusion Porosimeter Curve for Sample M10

than 70 microns, a complete pore spectrum could not be measured by this method.

Such was the case in the remainder of twelve selected materials, samples H11, H12, H13, M2, M4, M6 and M8. They constitute the most porous sintered fiber samples, two sintered powder samples and one sintered screen sample. The V-P curves for these samples are shown in Figures 15 to 21. In all of these cases the median pore diameter is greater than 70 microns. However, because of the shape of the V-P curves shown in Figures 15 to 21, the value of the lower bound estimate on median pore size can be increased. For example, sample M8 can be interpreted to have a median pore size greater than 100 microns.

TABLE 5

## Pore Space Distribution of Twelve Selected Porous Materials

<u>Sample No.</u>	<u>Measured Median Pore Diameter, microns</u>	<u>Pore Diameter Range of 90% of Pore Space, microns</u>
M2	> 70	-
M4	~ 80	-
M6	> 80	-
M8	>100	-
M10	50.0	43.4-57.8
H1	43.8	19.4-54.2
H2	35.0	13.3-48.9
H3	26.5	10.3-34.0
H6	40.7	15.5-59.3
H11	>80	-
H12	>70	-
H13	>80	-

The pore space distribution data presented by Figures 10 to 21 is summarized in Table 5. The median pore diameter is listed for each sample. Also tabulated for each of the twelve selected samples is the pore diameter range that represents 90 per cent of the pore volume in any given sample. In all cases the term pore diameter is defined as twice the radius defined by Equation (4).

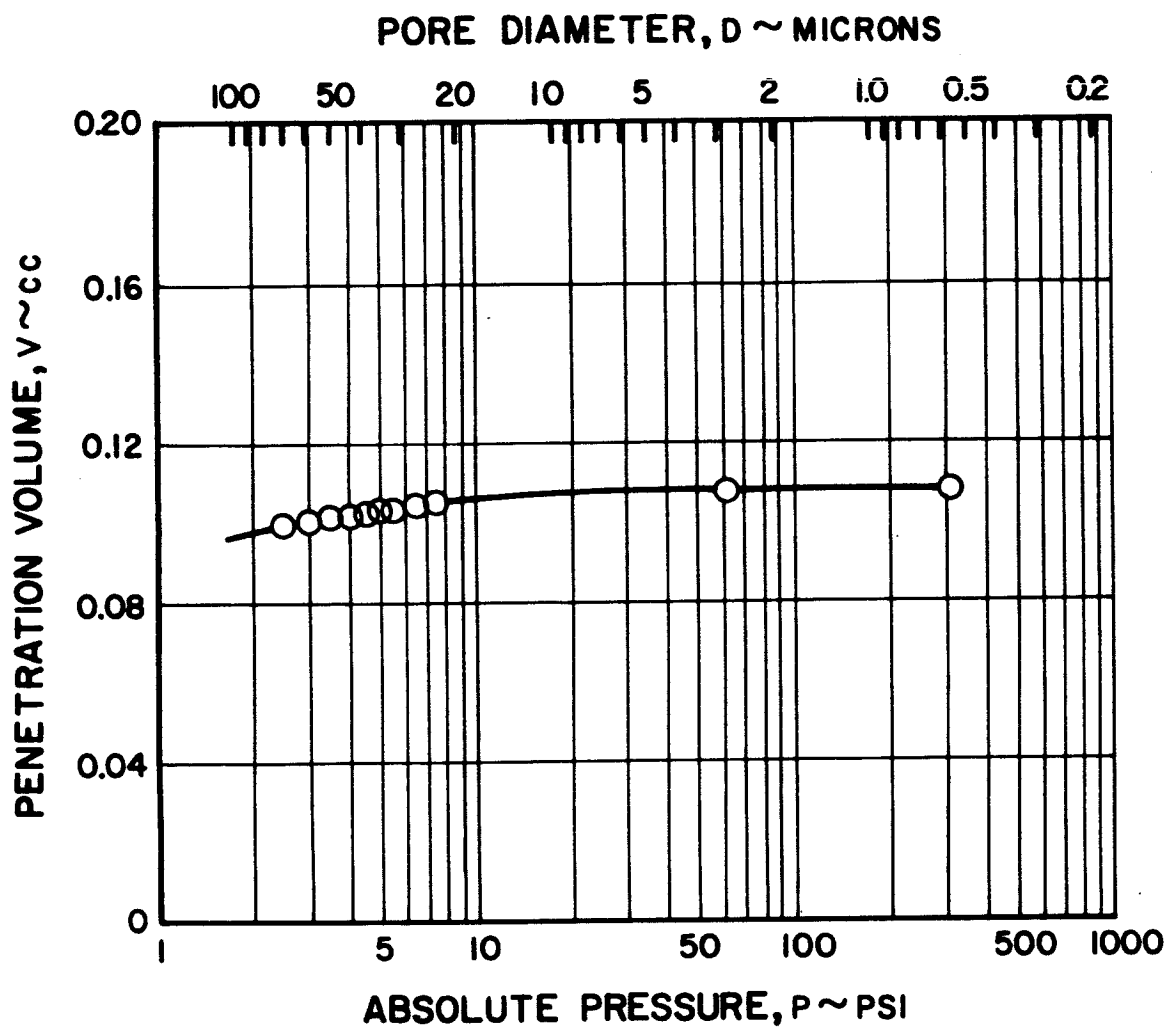


Figure 15 Mercury Intrusion Porosimeter Curve for Sample H11

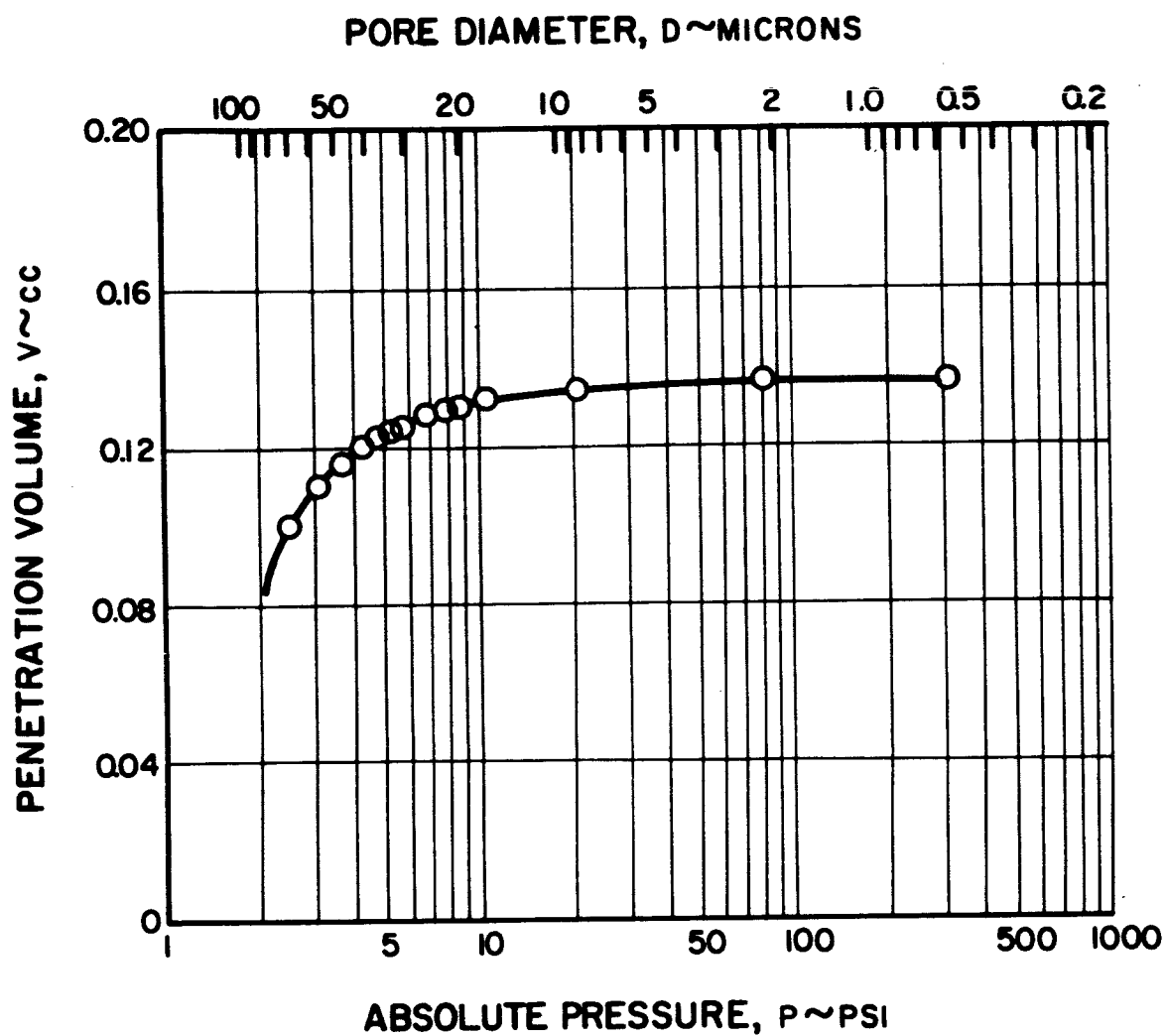


Figure 16 Mercury Intrusion Porosimeter Curve for Sample H12

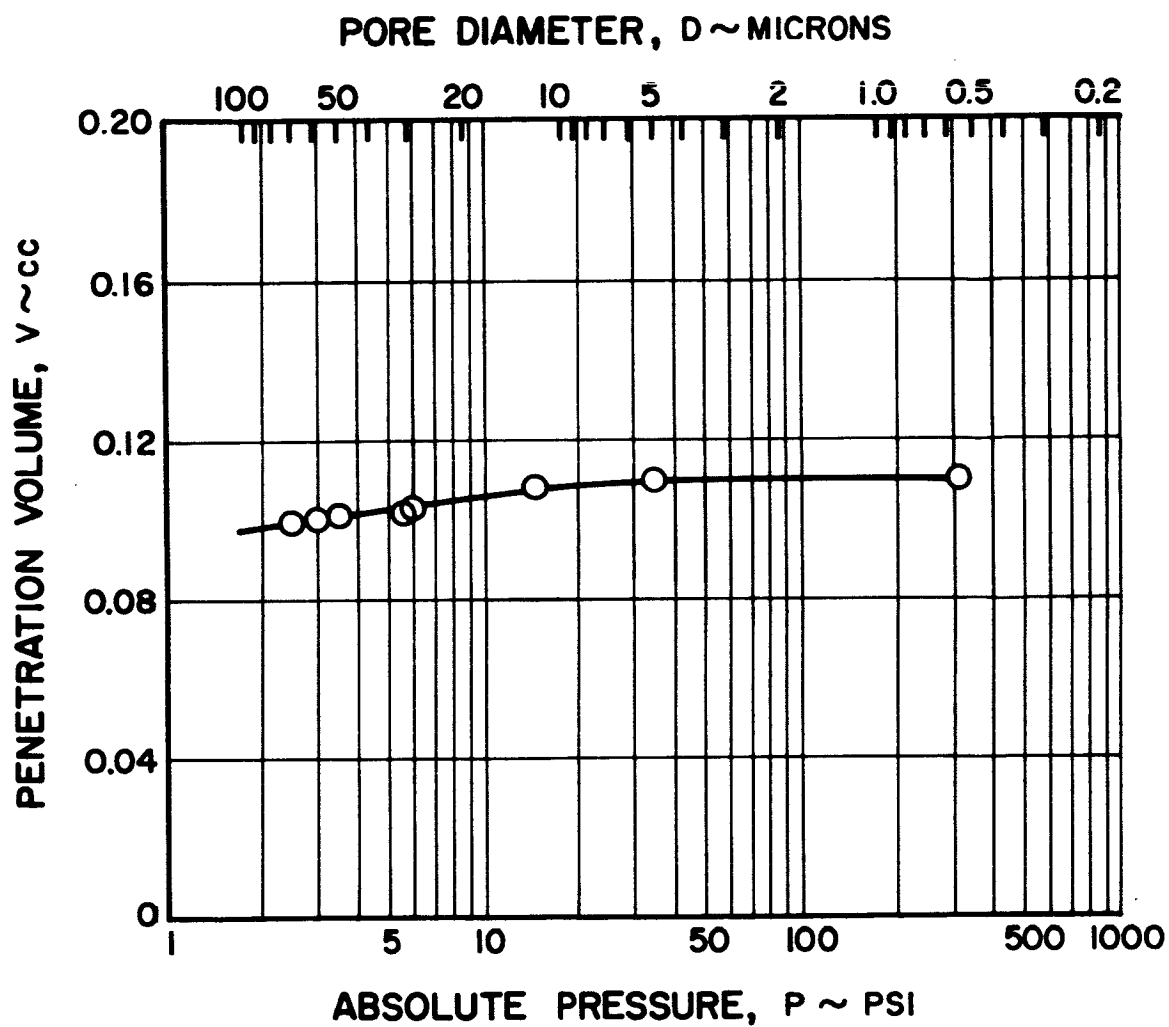


Figure 17 Mercury Intrusion Porosimeter Curve for Sample H13

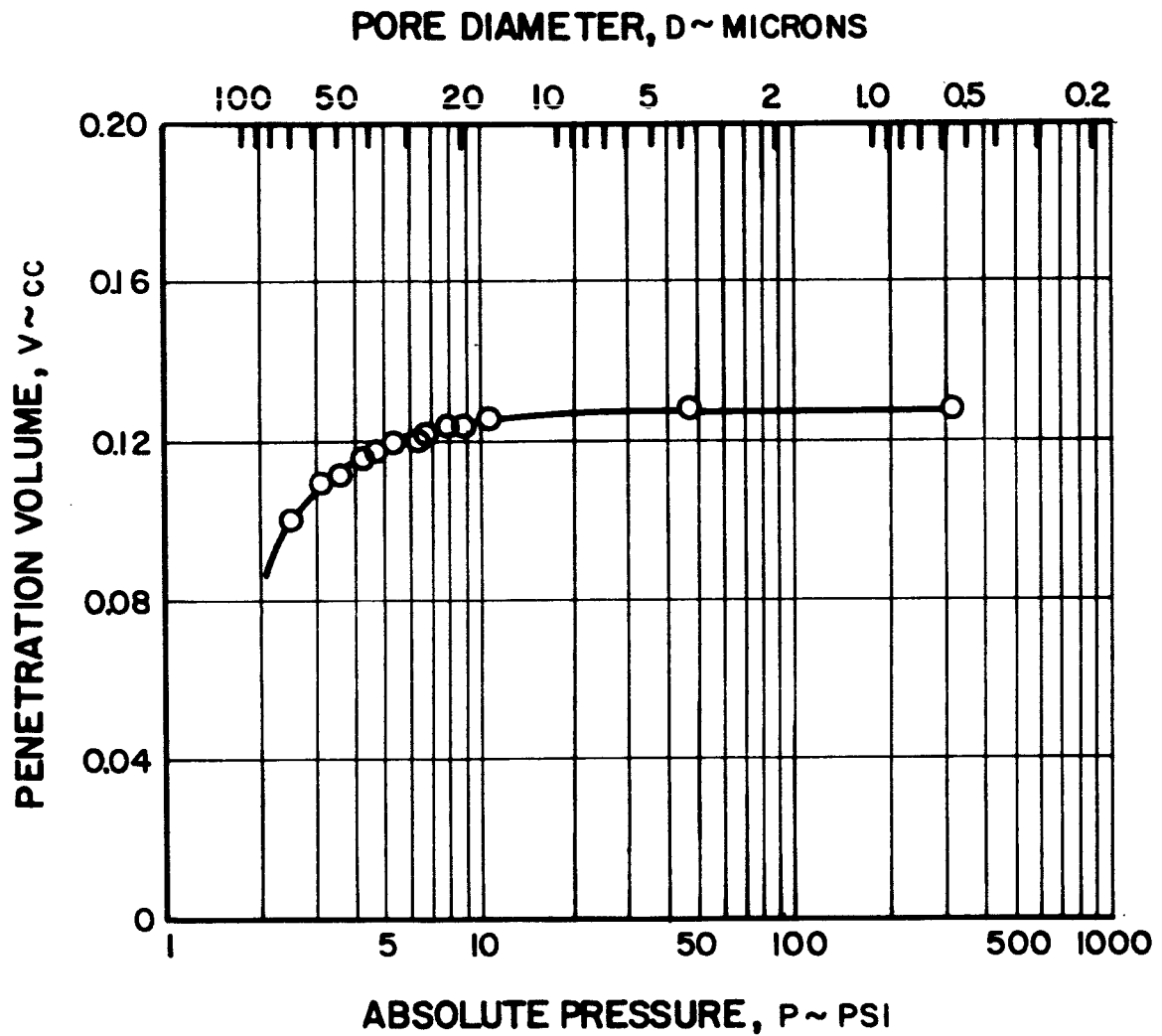


Figure 18 Mercury Intrusion Porosimeter Curve for Sample M2

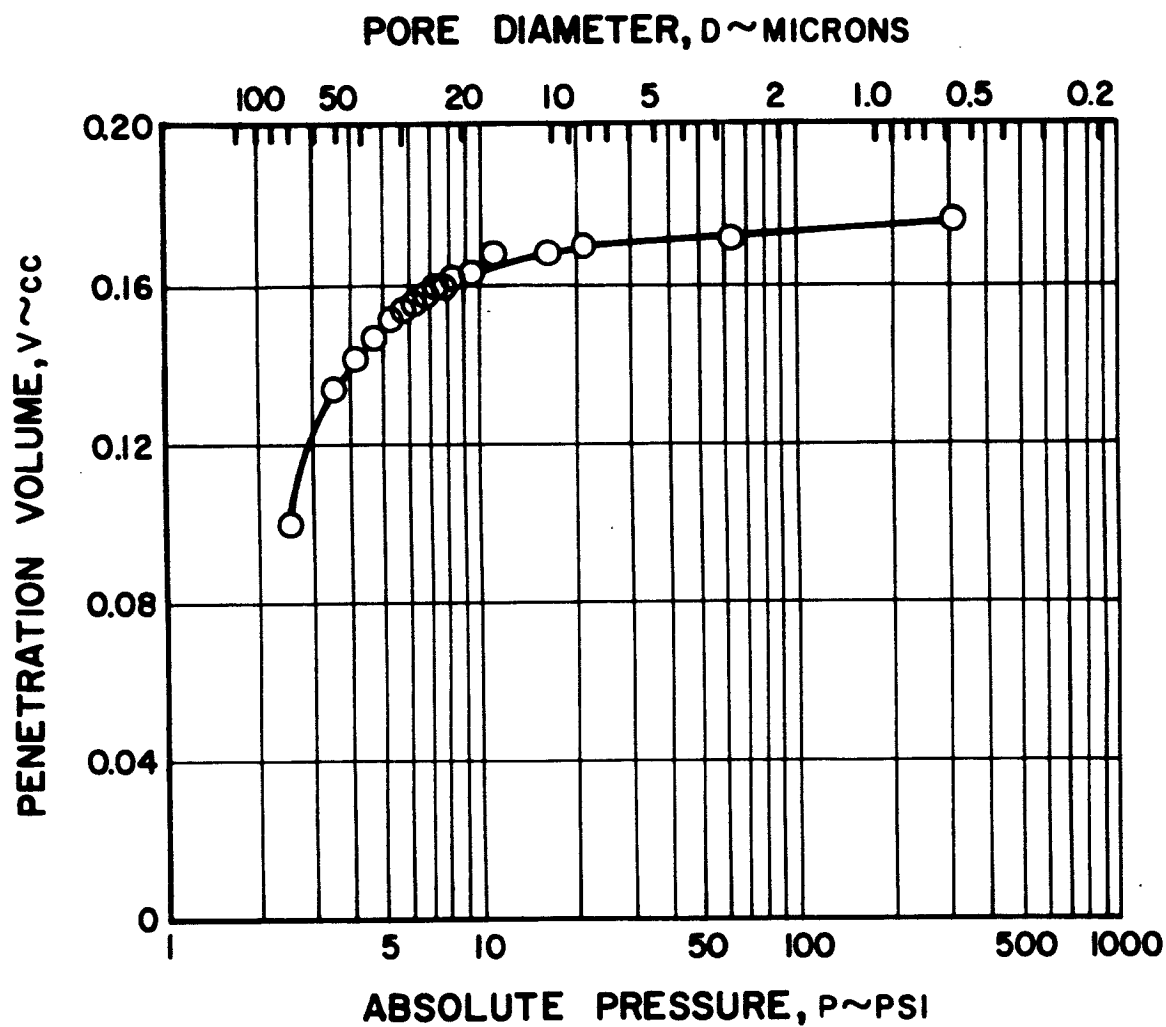


Figure 19 Mercury Intrusion Porosimeter Curve for Sample M4



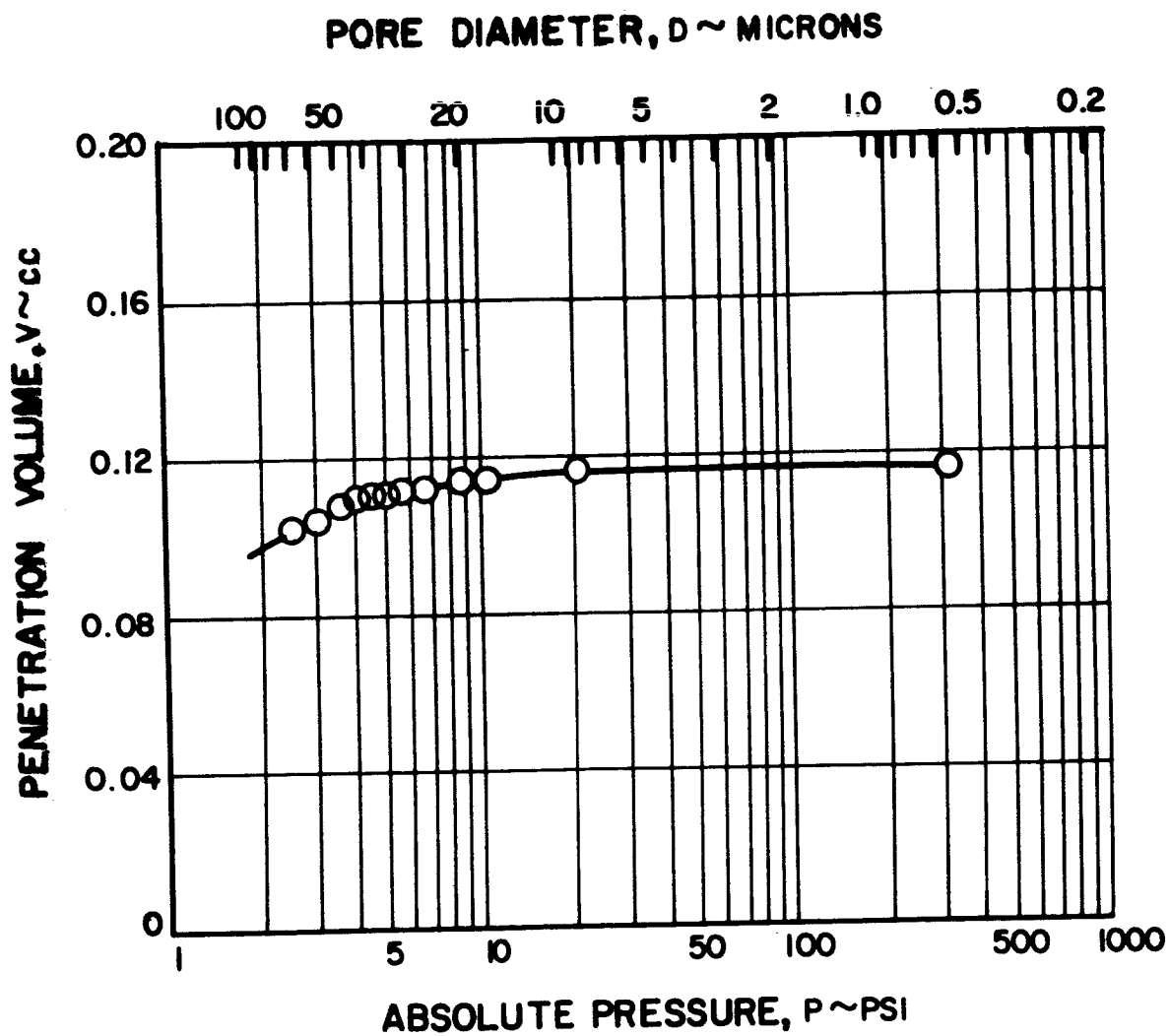


Figure 20 Mercury Intrusion Porosimeter Curve for Sample M6

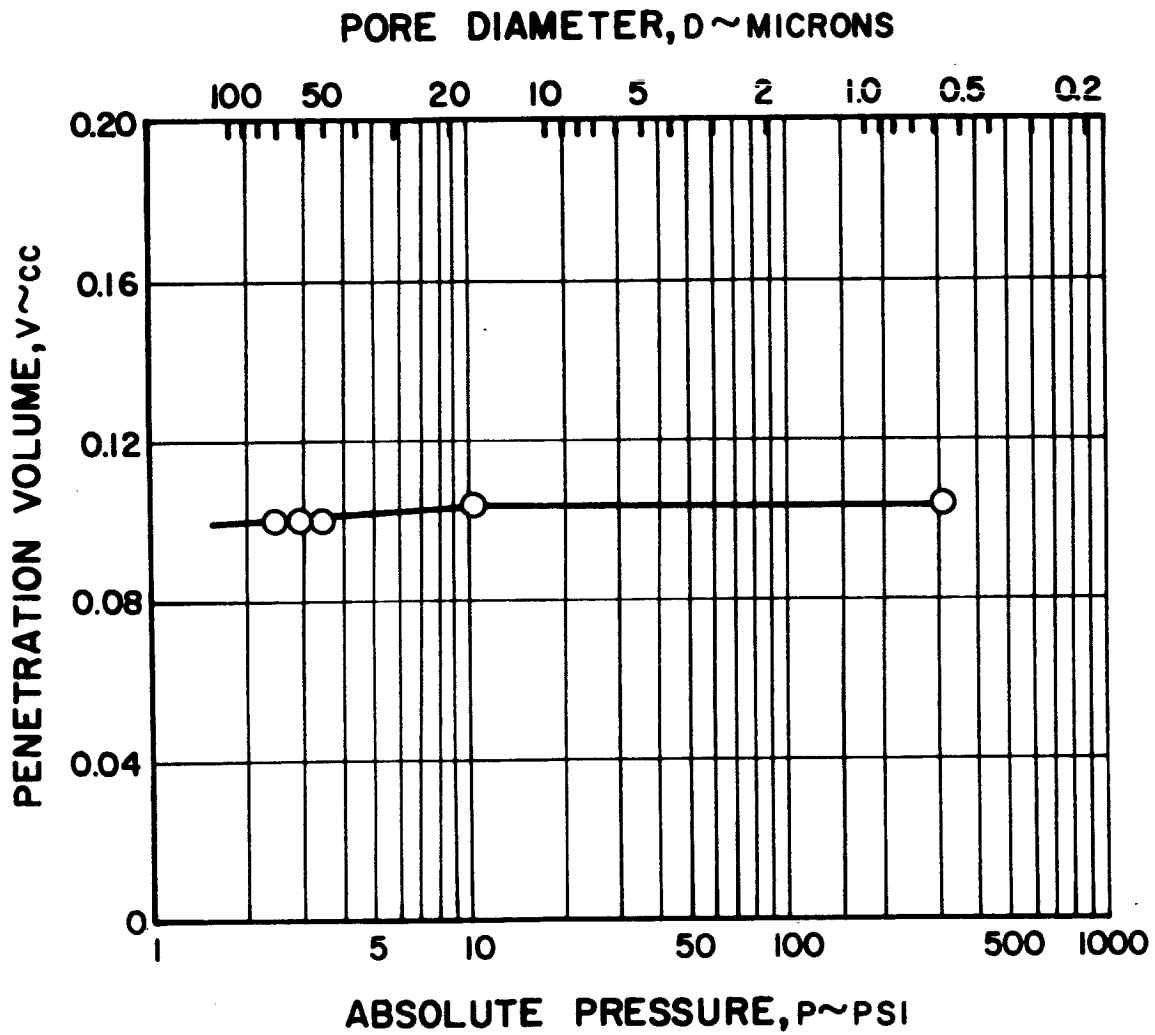


Figure 21 Mercury Intrusion Porosimeter Curve for Sample M8

### 3. Free-Flow Area Ratio

The free-flow area ratio is defined as the area available to flow of a fluid at any given cross-section of the porous material, divided by the total cross-sectional area. In accordance with this definition, the free-flow area ratio is a measure of the actual cross-sectional area available to the flow of a fluid in any given porous material. An expression for the free-flow area ratio was given in the first quarterly report as

$$F_{AR} = 1 - (1 - \epsilon)^{2/3} \quad (11)$$

where  $\epsilon$  is the porosity of the material. This expression was derived by considering a unit cube of the porous material and assuming that the mass of this porous cube could be compressed into a smaller solid cube. Equation (11) was then computed from a consideration of the frontal area of the porous cube and the solid cube. However, even though the porous material might be isotropic, the cube model used to derive Equation (11) was not. Thus Equation (11) is valid only when fluid flow is in a direction normal to the faces of the cube.

To overcome this obvious objection to Equation (11), an expression for  $F_{AR}$  that is based solely on considerations of isotropy can be derived as follows. In a given porous material, a body of any shape can be considered so that its smallest dimension is much greater than the largest pore size. The body will be considered to be  $x_1$  units long in some chosen x-direction and to have a cross-sectional area normal to the x-direction of  $A_T$ , where  $A_T$  is some known function of x.

By definition, the free-flow area ratio at a given x for the body of porous material is given by

$$F_{AR} \equiv \frac{A_F}{A_T} \quad (12)$$

or

$$A_F = F_{AR} A_T \quad (13)$$

where  $A_T$  is the total cross-sectional area at x,  $F_{AR}$  is the free-flow area ratio, and  $A_F$  is the total pore area contained in  $A_T$ .

The porosity of the body is given by

$$\epsilon \equiv \frac{V_P}{V_T} \quad (14)$$

where  $\epsilon$  is the porosity,  $V_T$  is the total volume of the body of porous material, and  $V_P$  is the total volume of the pore space in the body. The total volume can be calculated by integrating in the x-direction to get

$$V_T = \int_0^{x_1} A_T dx \quad (15)$$

Similarly, by using Equation (13) for  $A_F$ , the pore volume is given by the integral

$$V_P = \int_0^{x_1} F_{AR} A_T dx \quad (16)$$

Combining Equations (14), (15), and (16), it is seen that

$$\epsilon = \frac{\int_0^{x_1} F_{AR} A_T dx}{\int_0^{x_1} A_T dx} \quad (17)$$

As stated above,  $A_T$  is some known function of x. Now, if it is assumed that the porous material is truly isotropic and that the pore space is randomly distributed, the value of the free-flow area ratio as given by Equation (12) at any given x will be a constant, if the dimensions of  $A_T$  are large compared to the largest pore sizes. Thus, since  $F_{AR}$  is not a function of x, Equation (17) reduces to

$$F_{AR} = \epsilon \quad (18)$$

subject to the conditions of isotropy and a randomly distributed pore space. Hence, for an isotropic porous material with a randomly distributed pore space, the free-flow area ratio is equal to the porosity. This result agrees with a similar conclusion given by Carman<sup>1</sup>.

The photomicrographs of Figures 3 to 8 indicate that the assumptions of isotropy and a randomly distributed pore space apply reasonably well to sintered powder materials and sintered fiber materials. However, the structural regularity exhibited by the sintered screen sample shown in Figures 1 and 2 indicates that Equation (18) is at best an approximation to a mean value of  $F_{AR}$  for these porous materials. The interlocking of the screen layers discussed in Section III. A. will help both assumptions.

<sup>1</sup> Carman, P. C., Flow of Gases through Porous Media, Butterworth, 1956, p 8

Table 6 contains a list of values of free-flow area ratio computed from Equation (18) for all of the samples in this study. The porosity values were taken from those listed in Table 4. It should be mentioned that the accuracy of the values of  $F_{AR}$  listed for the sintered screen samples M7, M8, M9, and M10 is subject to the approximation that the samples are isotropic in structure and have a randomly distributed pore space.

TABLE 6

## Free-Flow Area Ratio of Porous Material Samples

	<u>Sample No.</u>	<u>Free-Flow Area Ratio, %</u>
Sintered Powder Samples	M1	59.7
	M2	65.8
	M3	47.7
	M4	54.0
	M5	69.1
	M6	69.6
Sintered Screen Samples	M7	62.5
	M8	67.9
	M9	67.8
	M10	67.6
Sintered Fiber Samples	H1	86.8
	H2	82.5
	H3	68.9
	H4	62.8
	H5	91.8
	H6	88.0
	H7	82.0
	H8	82.8
	H9	62.6
	H10	70.9
	H11	91.6
	H12	80.8
	H13	82.2

The values of the free-flow area ratio listed in Table 6 will be useful in computing actual fluid flow velocities, Reynolds numbers, and an equivalent flow pore diameter.

### C. Porous Material Machining

In the second quarterly report it was pointed out that one of the problems encountered when dealing with porous materials was that of cutting or machining a sample without disturbing the porous structure in the region adjacent to the cutting plane. A minimum of disruption is necessary to insure that there are no end effects at the edges of the samples used for the wick permeability and boiling studies.

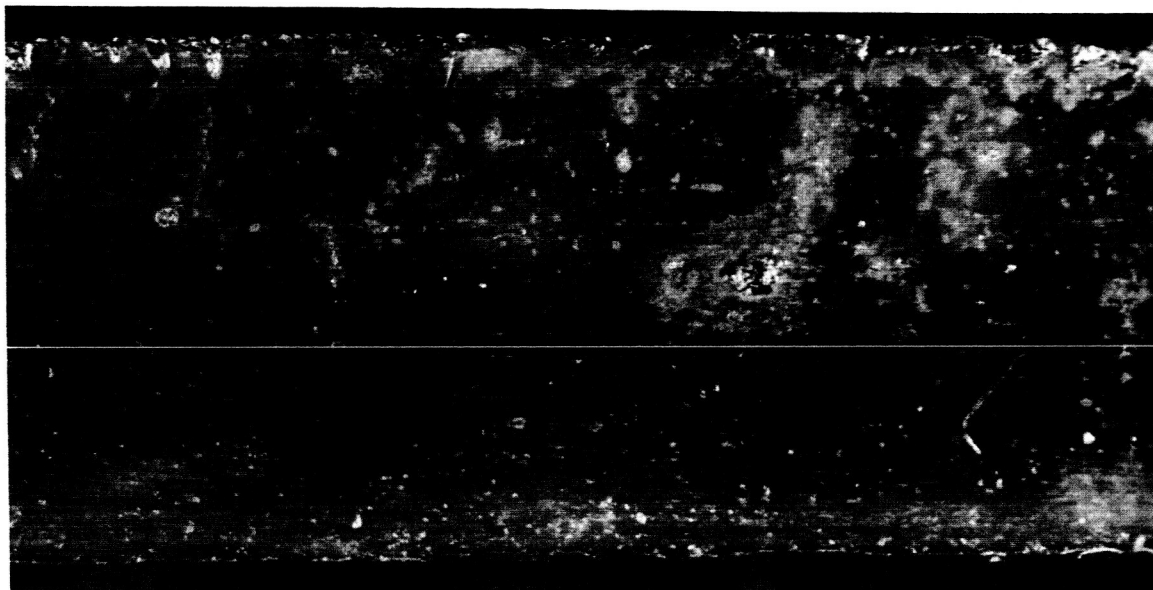
Normal cutting techniques such as band-sawing, shearing, grinding and cutting with a torch were found to both deform the porous material sample itself and smear the cut surface. Such a surface is shown in Figure 22, a photomicrograph of a cross-section of sample H4, a sintered nickel fiber material. The machined surface shown was produced by cutting the sample with a rotating rubber wheel charged with diamond dust. The nickel backup foil (0.0218 inch thick) is at the bottom of the cross-section, with porous structure (0.0982 inch thick) above it. It can be seen that almost the entire pore space has been smeared over and sealed off by the machining process. Such a surface would exhibit a relatively high resistance to flow during a permeability test.

The porous structure can be preserved during cutting by filling the sample with some supporting material such as a wax or a salt. The filler material can be removed after the machining operation by melting or leaching. However, it is difficult to determine whether the filler is completely removed or that it has not changed the wetting characteristics of the porous material.

Figure 23 shows a photomicrograph of the same sample H4 where the material was cut by electro-discharge machining (EDM). EDM is a process of metal removal brought about by an electrical spark jumping a gap between the workpiece and an electrode. A dielectric liquid flows between the electrode and the workpiece, both to cool the work and to remove the spark-eroded particles as they come off the workpiece.

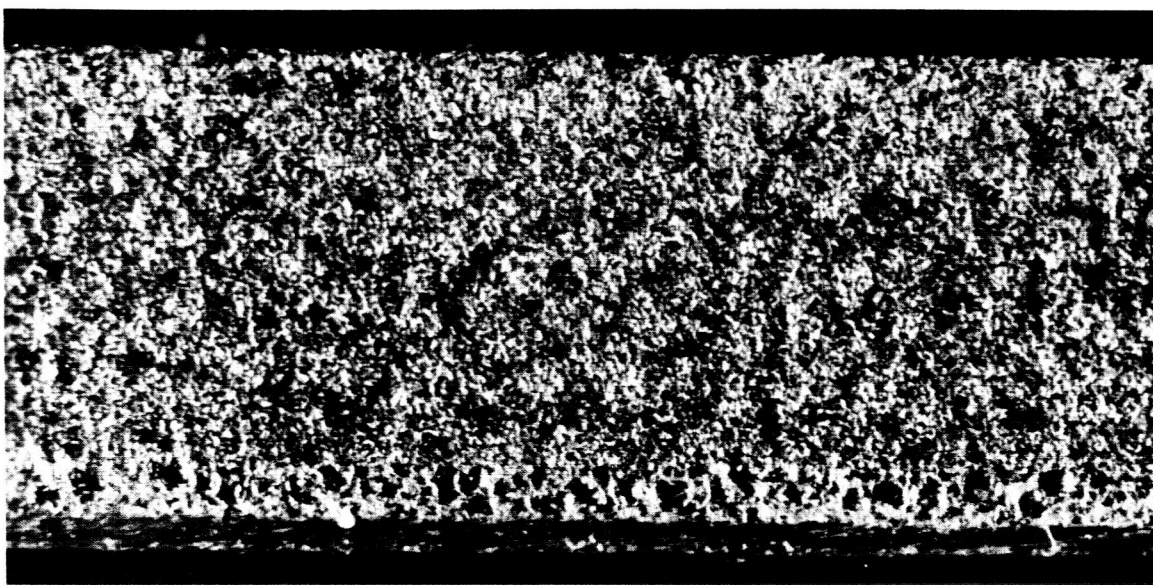
As seen by the cross-sectional view of Sample H4 in Figure 23, this machining method tends to produce a rough edge. The electrical discharges tend to erode the solid backup foil unevenly, producing a pockmarked surface. When examined under a microscope the porous material near the cut surface can be seen to be disrupted and opened up just the reverse of the situation shown in Figure 22.

The cutting process finally chosen was electrochemical machining (ECM). A cross-sectional view of Sample H4 cut in this manner is shown in Figure 24. Electrochemical machining is essentially metal removal by controlled electroplating in reverse. The workpiece and a shaped tool form a pair of electrodes.



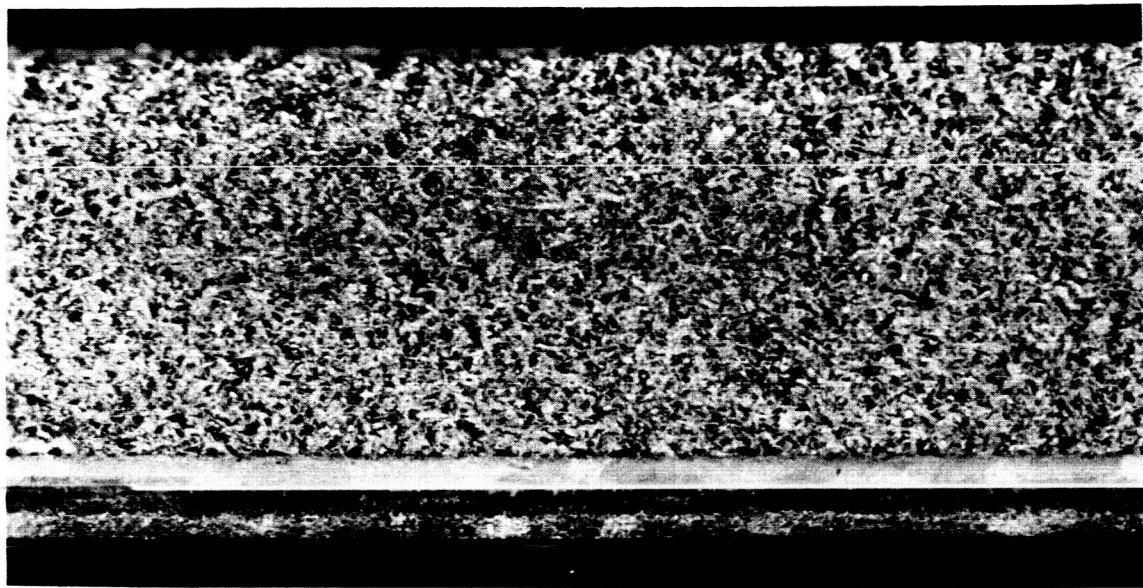
Mag: 21X

Figure 22 Cross-Sectional View of Sintered Nickel Fiber Sample H4  
Cut by Grinding Method



Mag: 21X

Figure 23 Cross-Sectional View of Sintered Nickel Fiber Sample H4  
Cut by Electrical Discharge Method



Mag: 21X  
Figure 24 Cross-Sectional View of Sintered Nickel Fiber Sample H4  
Cut by Electrochemical Machining Method



An electrolyte (usually an ordinary salt solution) is pumped between the work-piece and the tool, and a voltage is applied to them. The material of the work-piece is then removed by electrolysis, duplicating the shape of the tool. The electrolyte sweeps away the metal ions so that they cannot deposit out on the tool, which acts like an anode. This cutting process occurs at the temperature of the electrolyte so that there are no excessive temperatures at the cut surface. Also, because of the electrolysis process, all chemical reactions take place right at or near the cut surface rather than in the matrix of the porous material.

Figure 24 shows that both the porous material and the backup foil of Sample H4 were cut cleanly and with a minimum of disruption. As will be shown in Section V. E., samples cut by the ECM method show no observable end effects. The machined surfaces shown in Figures 1, 3, 5, and 7, were all produced by the electrochemical machining process.

During the last quarter the special tooling necessary for the ECM process was constructed and all of the boiling and permeability samples reported on in the sections to follow, were cut using the ECM method.

#### D. Summary

A total of 23 porous materials was selected, representing three classes of porous materials: sintered metal screens, sintered metal powders, and sintered metal fibers. Each sample was composed of either nickel or 430 stainless steel.

The porosity of all the samples was measured and was found to vary between 47.7 and 91.8 per cent.

A mercury intrusion porosimeter was used to measure the pore size distribution function of twelve of the twenty-three porous material samples. A complete pore spectrum was found for five of the twelve samples. The median pore diameter for these five ranged from 26.5 to 50.0 microns.

The free-flow area ratio, useful for computing Reynolds number and effective flow velocities in a given porous material, was found to be equal to the porosity. Thus the free-flow area ratio ranged from 47.7 to 91.8 per cent for the twenty-three samples.

A study of the machining of porous materials was made. It was found that the best method available was that of electrochemical machining.

#### IV. WICKING RISE TESTS - TASK 1

##### A. Objective

The wick rise tests were devised to determine the maximum height to which a liquid will rise in any given porous material. This information will yield a measure of the minimum liquid-vapor interfacial radius of curvature that the wick will support. As discussed in the first quarterly report, the value of this curvature is needed to evaluate the maximum pumping force produced by the wick. To study the effect of the liquid itself, two liquids are used, water and Freon 113.

##### B. Description of Wicking Rise Apparatus

The wicking rise apparatus was described in detail in the second quarterly report and will be discussed here only briefly. The test apparatus consists of glass tubes with a 60 mm inside diameter which are attached in a vertical position to a metal framework as shown in Figure 25. Each tube encloses a wicking sample and is open at the bottom with a rubber stopper on the top. The stopper has two openings in it to receive a valve assembly, used in venting the tube before the start of a test, and a fitting which allows the sample height to be adjusted. The sample is suspended in the glass tube by a stainless steel rod and clip that passes through the fitting. Also attached to each rod is a thermometer used in recording the temperature in the tubes. The glass tubes are suspended in a Plexiglas reservoir which has a Plexiglas top fitted with soft Neoprene seals that fit around the outside of each glass tube. The seals and the Plexiglas top prevent evaporation of the liquid contained in the reservoir. The Plexiglas reservoirs are large enough so that the level will remain nearly constant while tests are in progress. The reservoirs are filled with either water or Freon 113, the two liquids under investigation.

The bottom of each tube is submerged below the surface of the liquid in the reservoir, thereby sealing the tube and sample from the atmosphere, and wetting the lower end of the wick sample. The air in the tube becomes saturated, preventing any net evaporation from the wick during and after the time the liquid has risen to the equilibrium height.

As pointed out in the second quarterly report, a long time (on the order of days) can be required for the liquid front to reach an equilibrium height in a wicking sample. For this reason a second wicking rise apparatus essentially identical to the first was constructed to minimize testing time. Figure 25 shows the original wicking apparatus (Number 1) complete with wicking samples installed. The second wicking rise apparatus (Number 2) is shown in Figure 26.

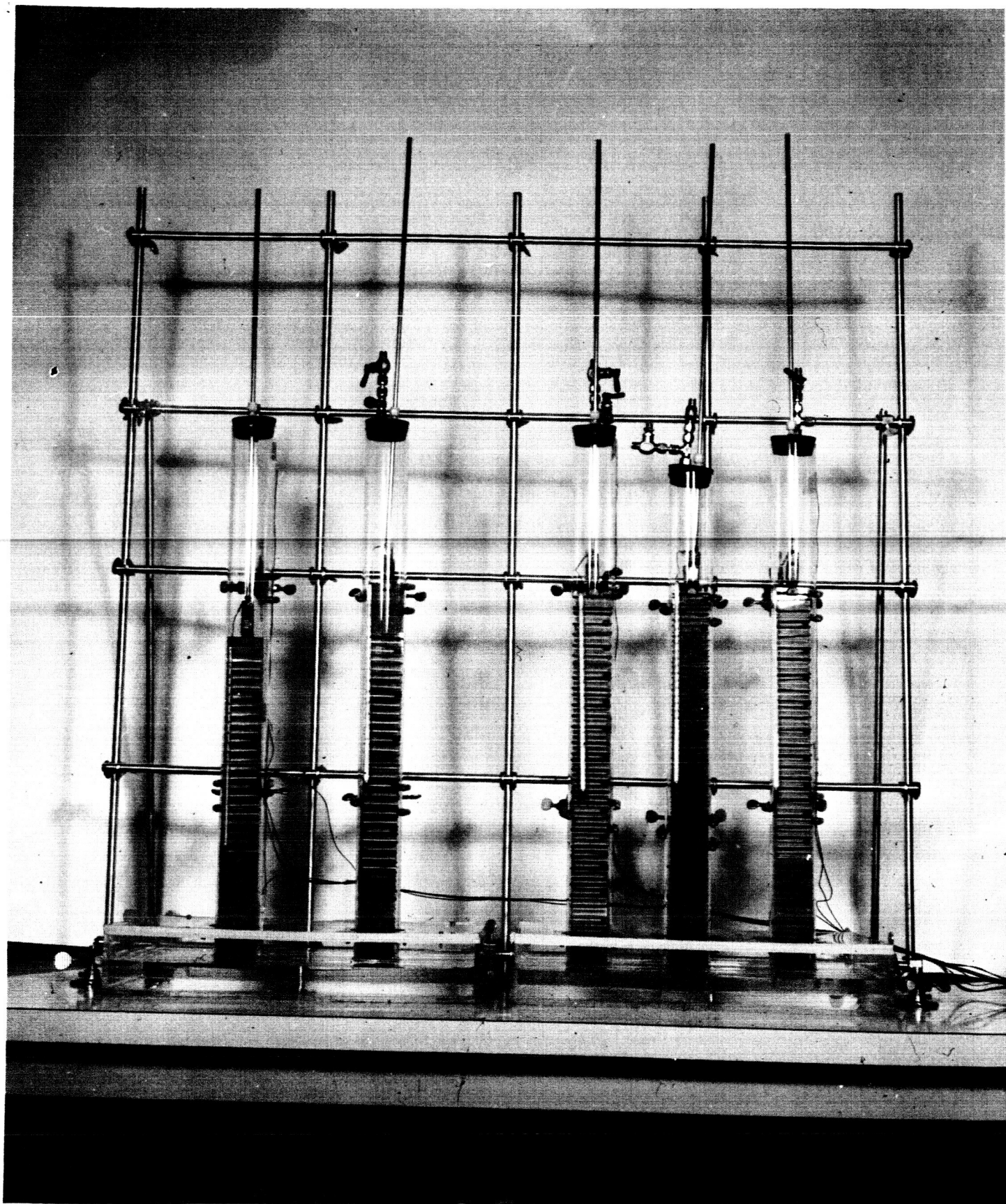


Figure 25 Wicking Apparatus with Samples Installed

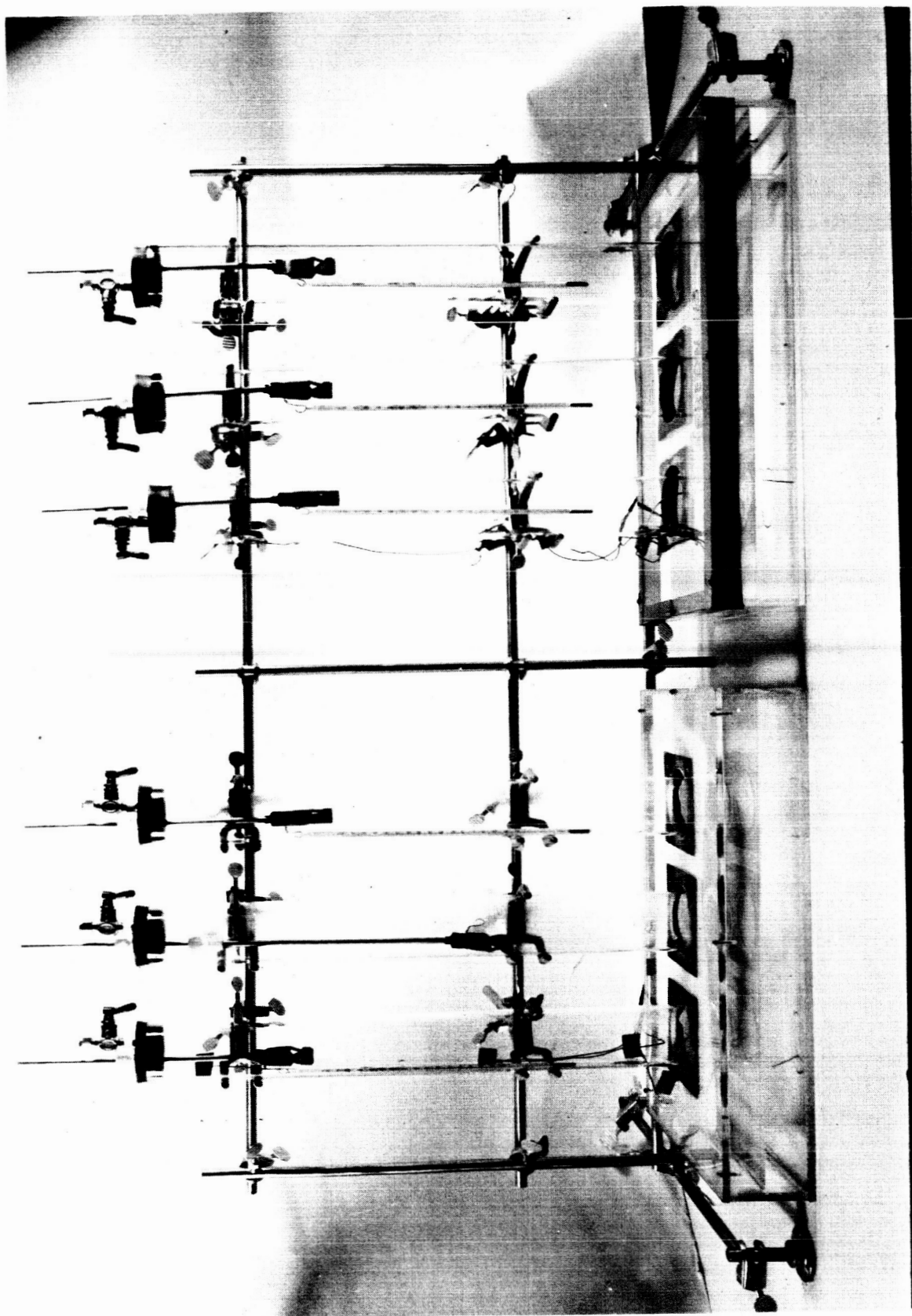


Figure 26 Wick Apparatus No. 2 without Samples

Thus a total of eleven wicking samples could be tested at any given time. During tests each apparatus was completely enclosed in a multiwalled cardboard enclosure to keep the entire apparatus at a near constant temperature and to minimize temperature gradients along the length of the wicking samples. Each enclosure had a Plexiglas front for viewing the samples during a test. Thermocouples were placed at various positions in each enclosure and each reservoir to ensure that temperature gradients were small.

### C. Wicking Rise Test Procedure

The procedure involved in observing the liquid front in a wicking sample was described in the second quarterly report. Basically, it consists of placing strips of pink litmus paper 0.30 inch apart along the vertical length of the sample. In the tests involving water the wicking liquid was actually an aqueous solution of 0.03 per cent potassium hydroxide, essentially having the same surface chemistry characteristics as pure water. The liquid front which is difficult to visually observe in the sample itself, was located by noting when each successive litmus paper started to turn blue.

The same technique was utilized during the wicking tests in which Freon 113 was used, except that blue litmus paper was substituted for the pink. Nothing was added to the Freon, for it was found that the blue litmus paper turned a very visible darker blue immediately upon coming in contact with Freon 113.

Before any wicking test was begun, each sample was subjected to the following cleaning procedure:

- 1) Washing the sample in a vapor degreaser and immediately rinsing the sample in distilled water before the condensed vapor re-evaporated,
- 2) Bathing in a reagent-grade acetone bath,
- 3) Submerging the sample immediately in distilled water, followed by several distilled water rinsings, and
- 4) Air-drying the sample in a clean oven at 500°F for at least 2 hours.

This procedure was followed for each sample to try to insure that the wetting characteristics of each sample would stay constant. After a sample was removed and cooled in the atmosphere, it was stored in a clean plastic bag until tested.

At the start of a wicking test, the sample with attached litmus paper was placed into one of the tubes shown in Figures 25 and 26, with the end of the sample above the reservoir level. The air in the tube was allowed to come into equilibrium with the liquid so that there was no net mass transfer during the actual wicking test. The lower end of the vertical wicking sample was lowered into the liquid by means of the fitting at the top of the tube, and a stopwatch started. The time, temperature, and level were recorded every time a litmus paper changed color, indicating passage of the liquid front. When the rate of rise slowed to less than 0.3 inch (one litmus paper) per hour, readings were taken every hour. When the rate of rise of the liquid front was less than 0.3 inch for every two hours, readings were taken at two-hour intervals to the end of a test. The wicking run on a sample was terminated when either, 1) the liquid front reached the sample top, or 2) the liquid front failed to rise 0.3 inch (one litmus paper) in 3 days. The height at which the latter occurs is defined as the equilibrium height,  $l_m$ .

#### D. Test Results

At least one wicking rise test was run on each of the samples described in Section III. A. In some cases as many as three wicking tests in water and one in Freon 113 were run on a sample.

The results of the wicking tests in water are shown in Figures 27 to 48 which present the variation of liquid height with time. The only sample listed in Section III. A. that is not represented in these figures is Sample H5. This sample was excluded after it was found that it had not been completely oven-dried after the cleaning process, which resulted in erroneous data for the only wicking test run on H5. In all cases the curves shown in these figures represent the particular wicking test that resulted in the largest value of the equilibrium height.

Representative wicking samples were chosen from those that had the largest value of  $l_m$  with water. These samples, M1, M4, M6, H1, H2, and H6, were then recleaned and prepared for wicking tests with Freon 113. The results of these tests are shown in Figures 49 to 55.

Because of the relatively long time required for the liquid front to reach equilibrium in a sample, all the plots shown in Figures 27 to 55 have logarithmic time scales. As shown in these figures this equilibrium time can exceed 10,000 minutes.

In a number of the tests the samples proved to be too short, as the liquid front rose to the top. This occurred with samples M3, H1, H2, H3, H4, H6, H7, H8, H9, and H10 in the tests involving water.

In tests where the liquid front did not progress to the top of the sample (samples

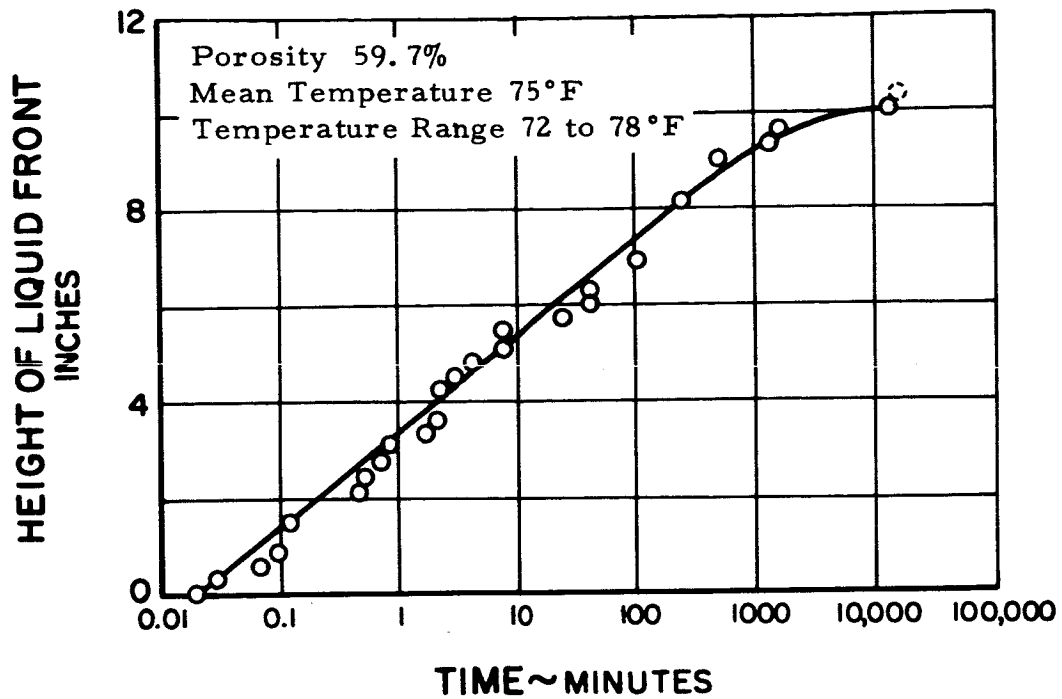


Figure 27 Water Wicking Curve for Sintered Nickel Powder Sample M1

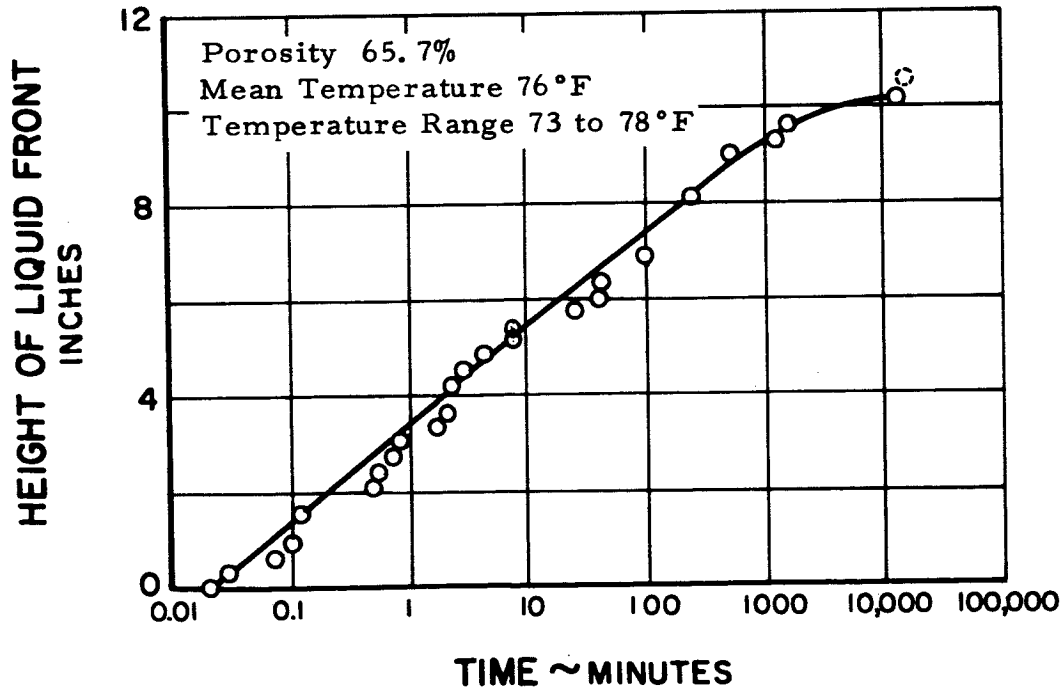


Figure 28 Water Wicking Curve for Sintered Nickel Powder Sample M2

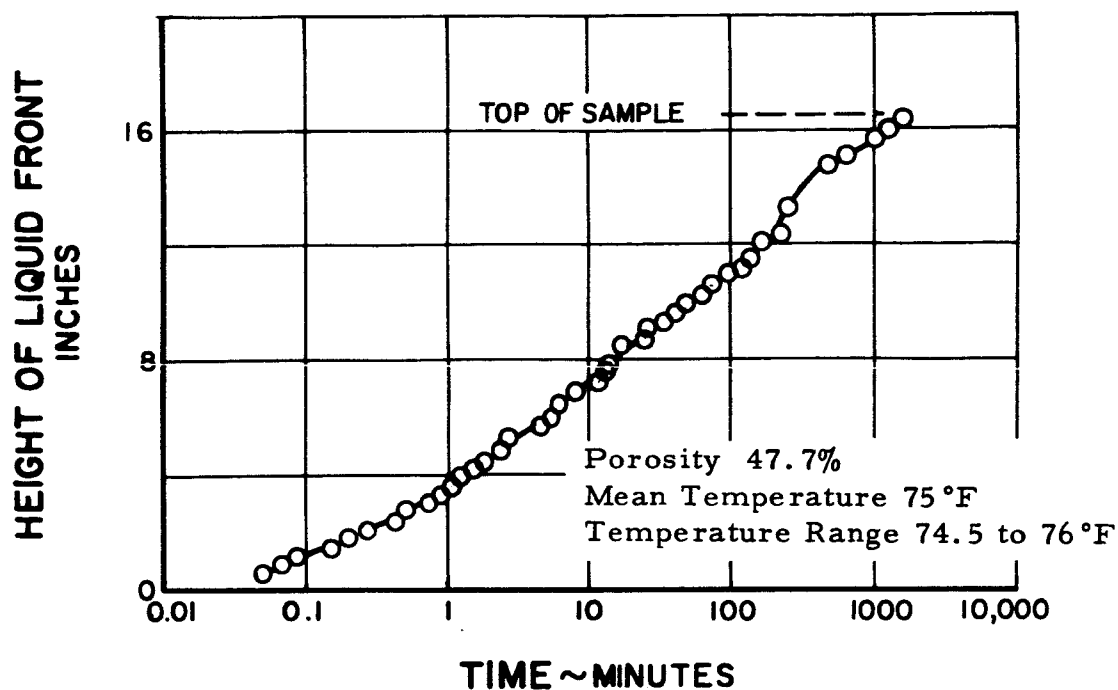


Figure 29 Water Wicking Curve for Sintered Nickel Powder  
Sample M3

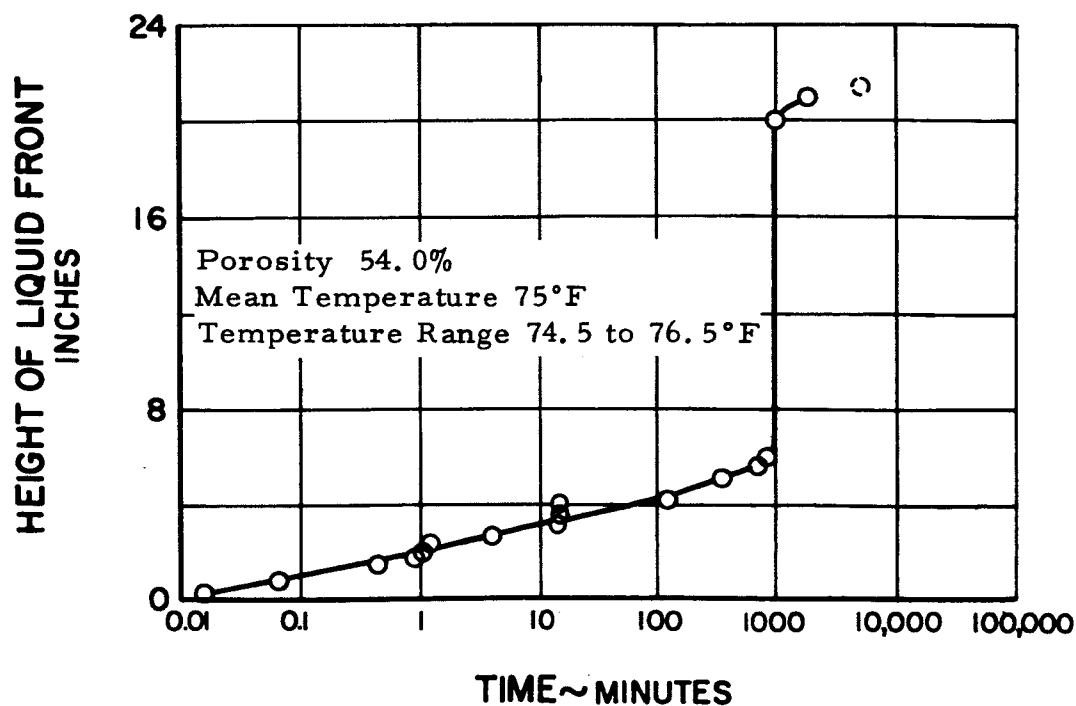


Figure 30 Water Wicking Curve for Sintered Nickel Powder  
Sample M4



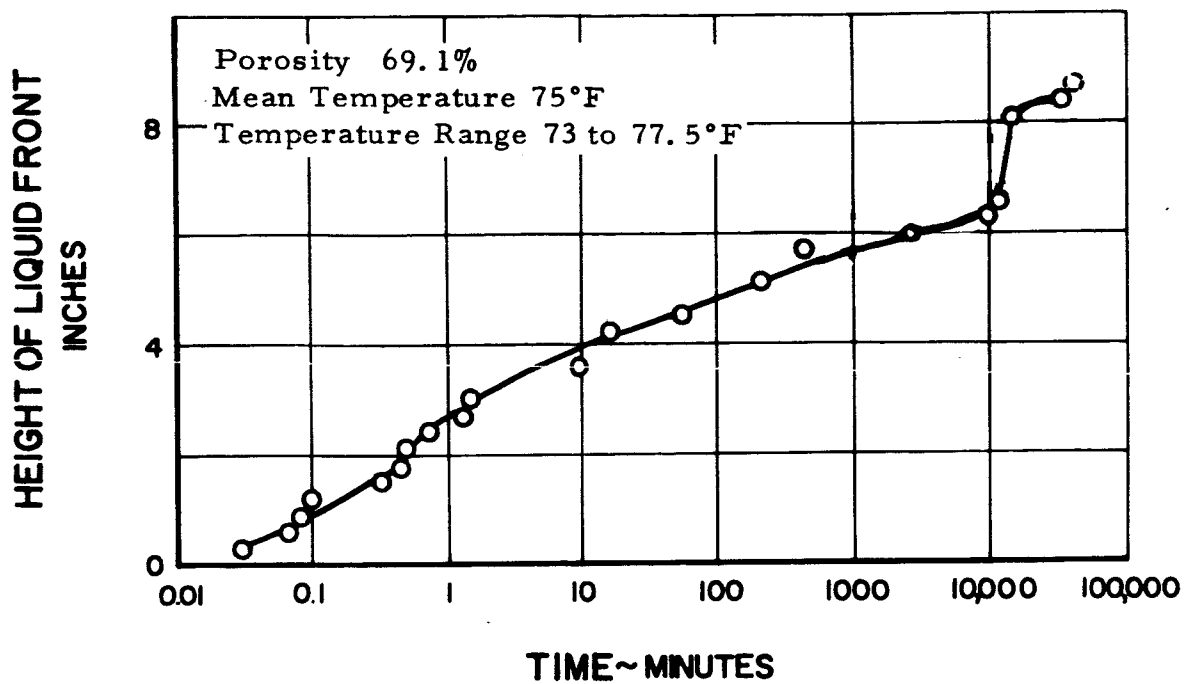


Figure 31 Water Wicking Curve for Sintered Nickel Powder Sample M5

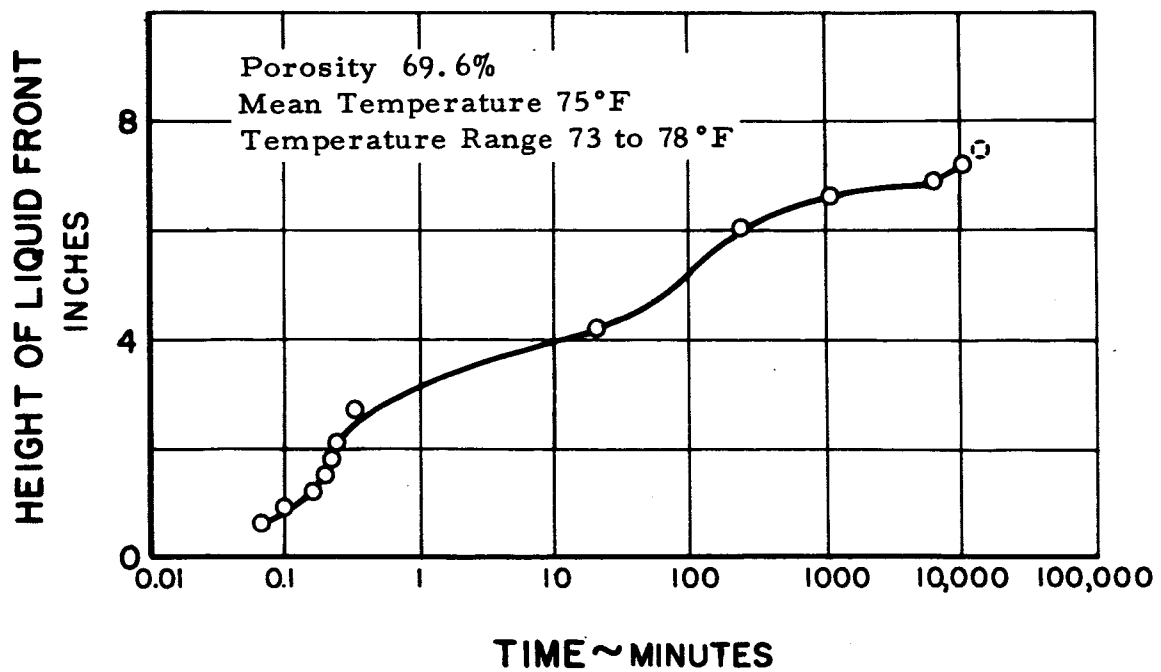


Figure 32 Water Wicking Curve for Sintered Nickel Powder Sample M6

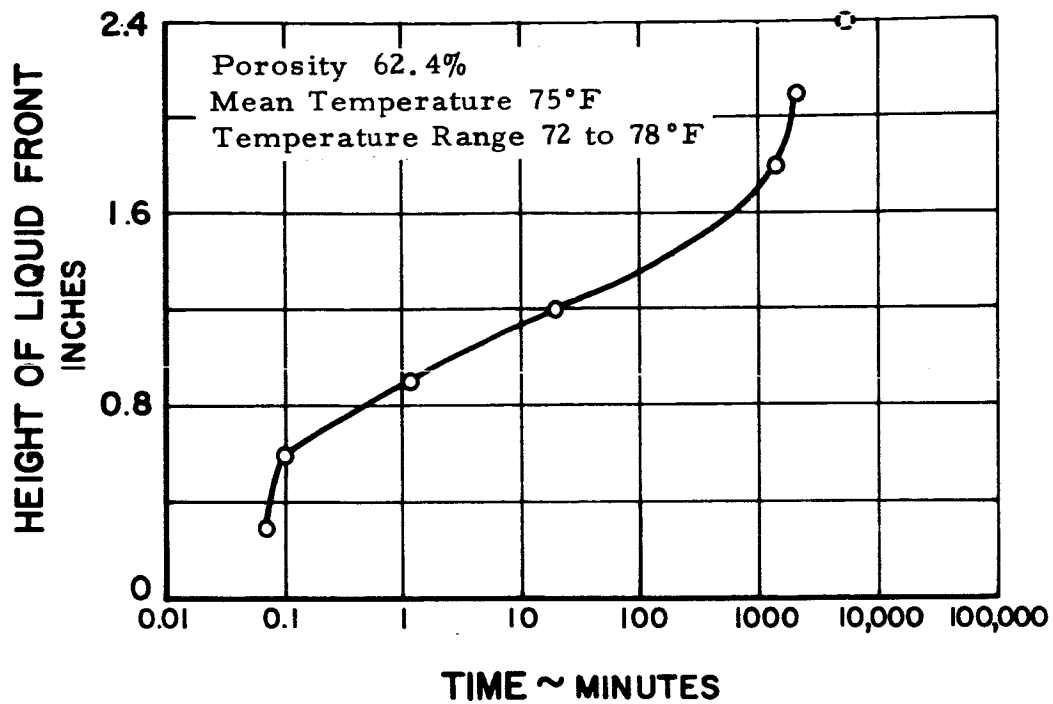


Figure 33 Water Wicking Curve for Sintered Nickel Screen Sample M7

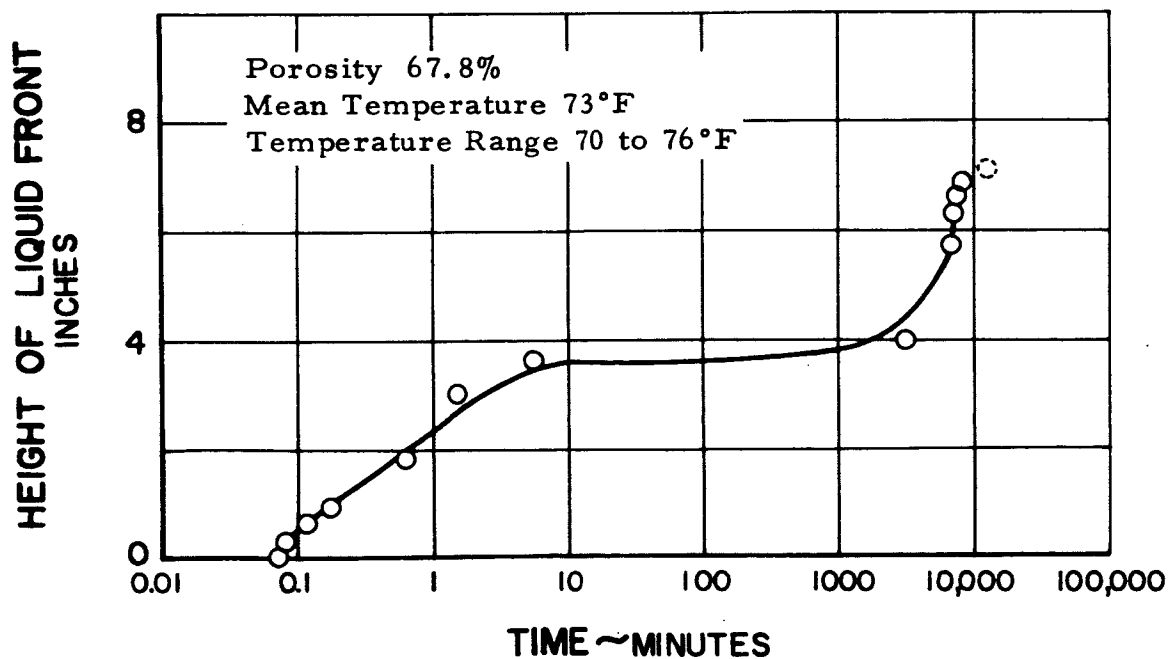


Figure 34 Water Wicking Curve for Sintered Nickel Screen Sample M8

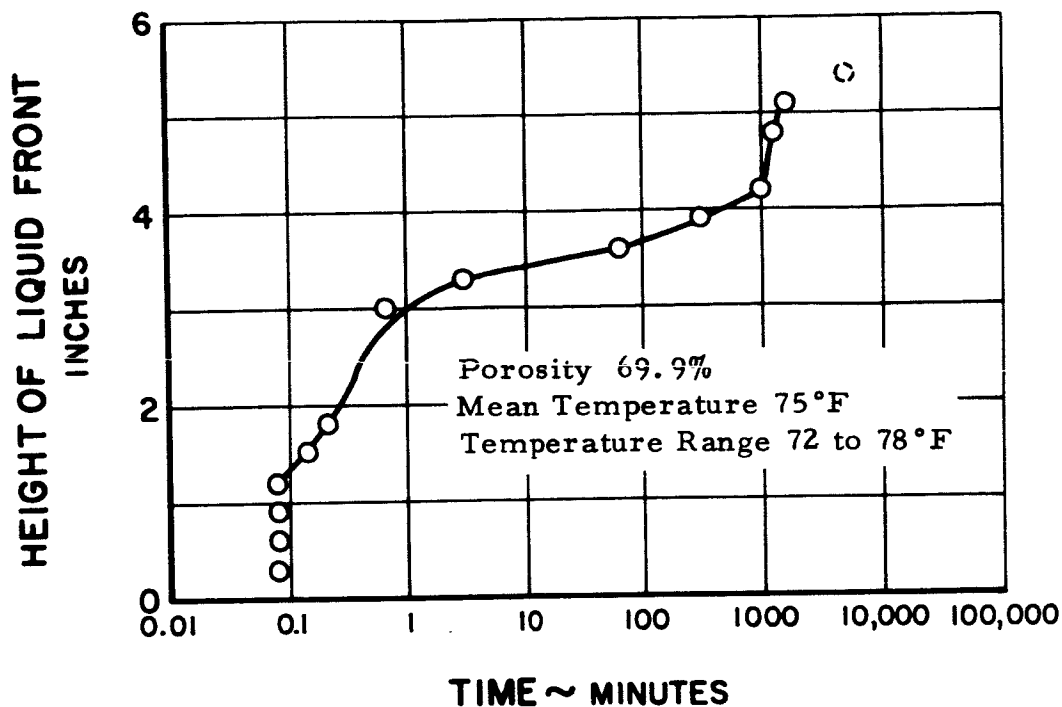


Figure 35 Water Wicking Curve for Sintered Nickel Screen Sample M9

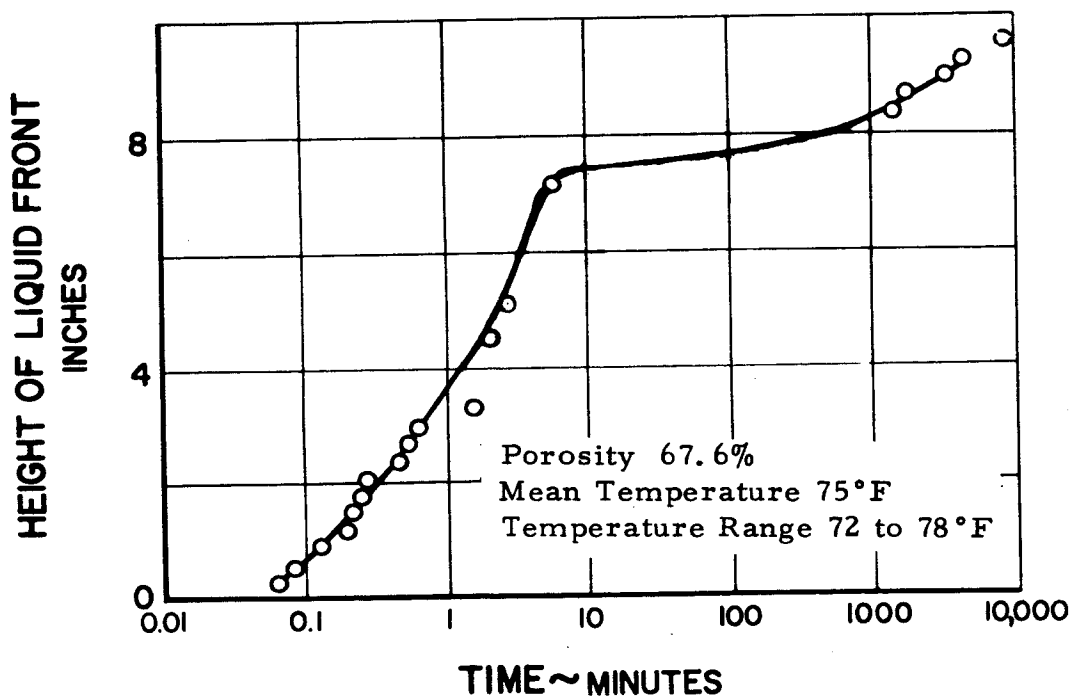


Figure 36 Water Wicking Curve for Sintered Nickel Screen Sample M10

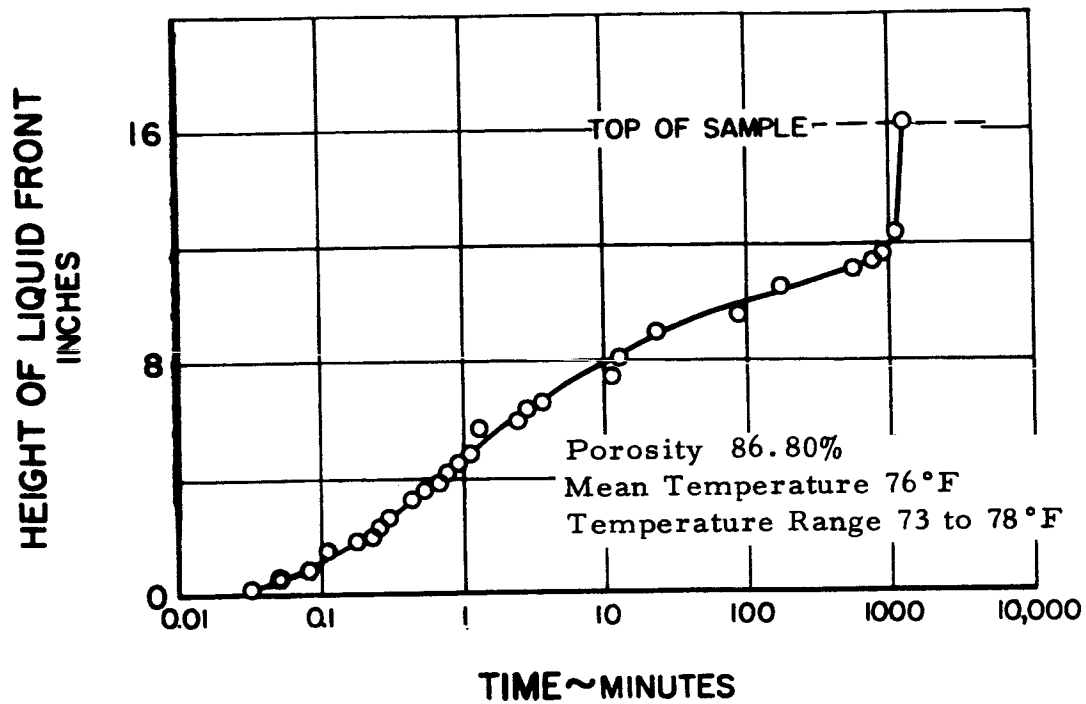


Figure 37 Water Wicking Curve for Sintered Nickel Fiber Sample H1

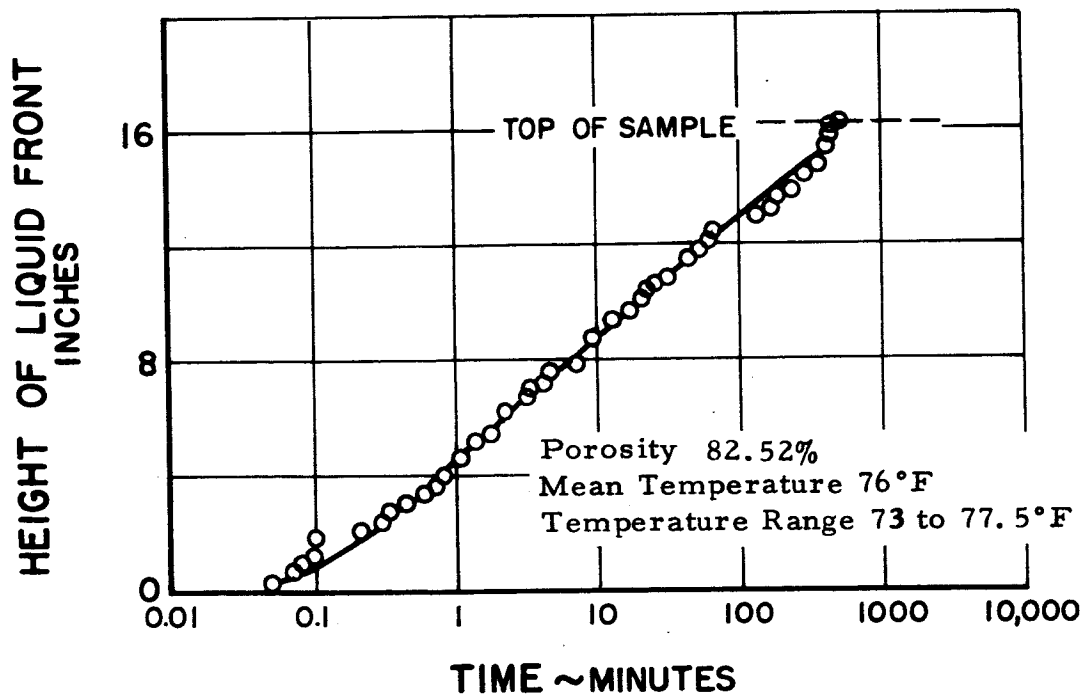


Figure 38 Water Wicking Curve for Sintered Nickel Fiber Sample H2

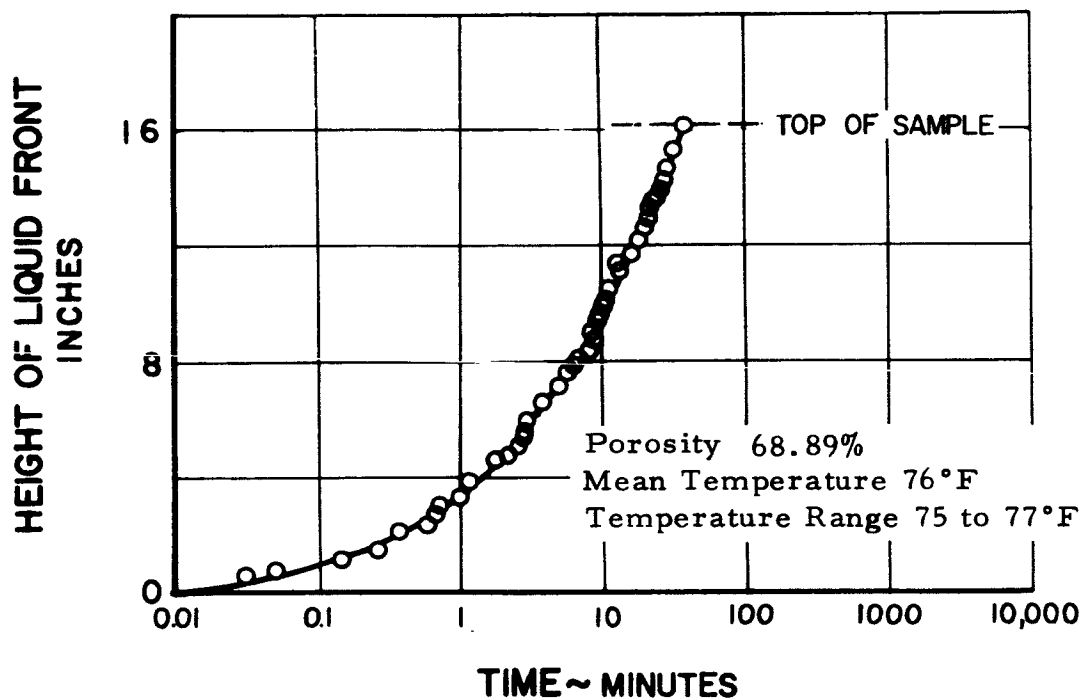


Figure 39 Water Wicking Curve for Sintered Nickel Fiber Sample H3

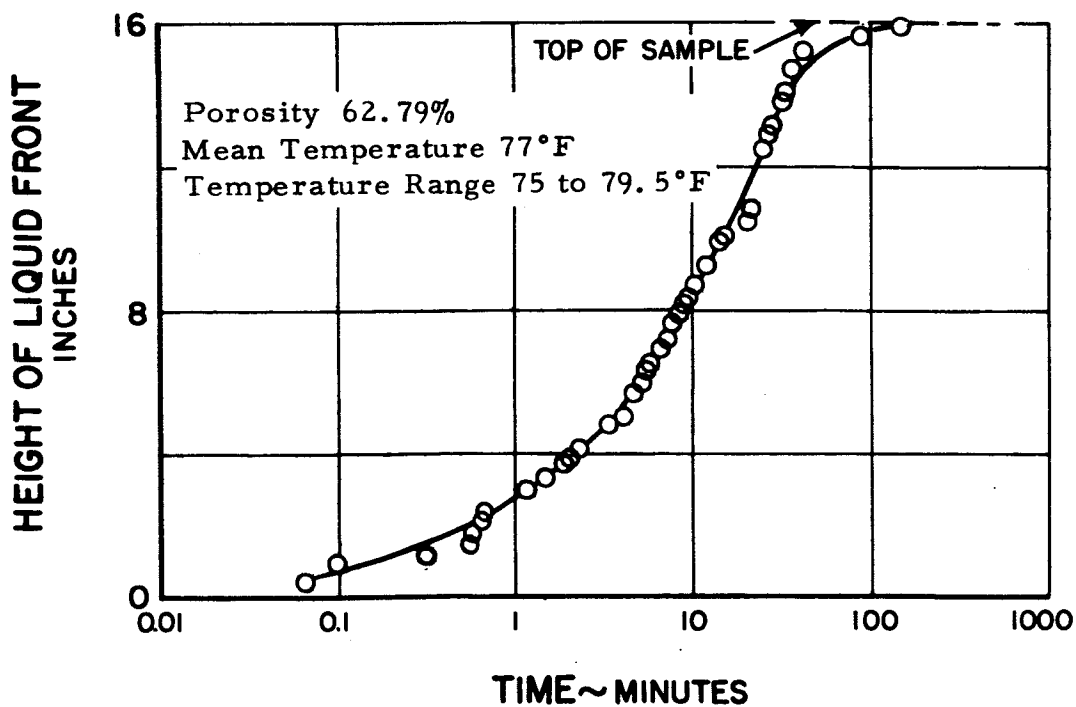


Figure 40 Water Wicking Curve for Sintered Nickel Fiber Sample H4

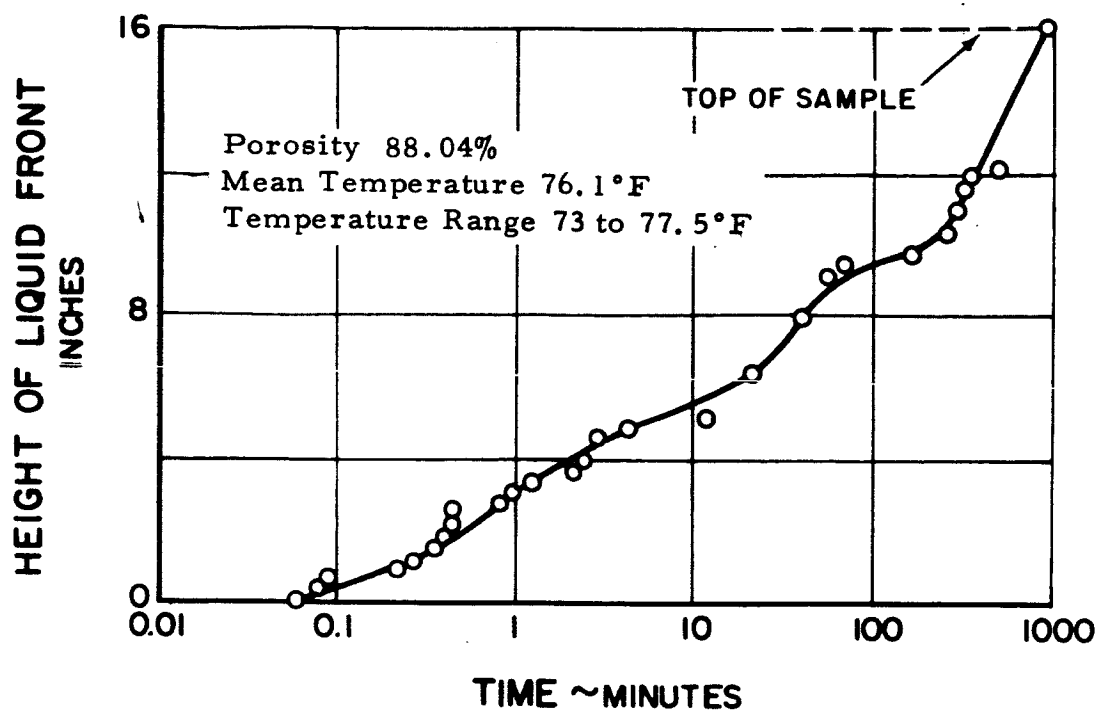


Figure 41 Water Wicking Curve for Sintered Nickel Fiber Sample H6

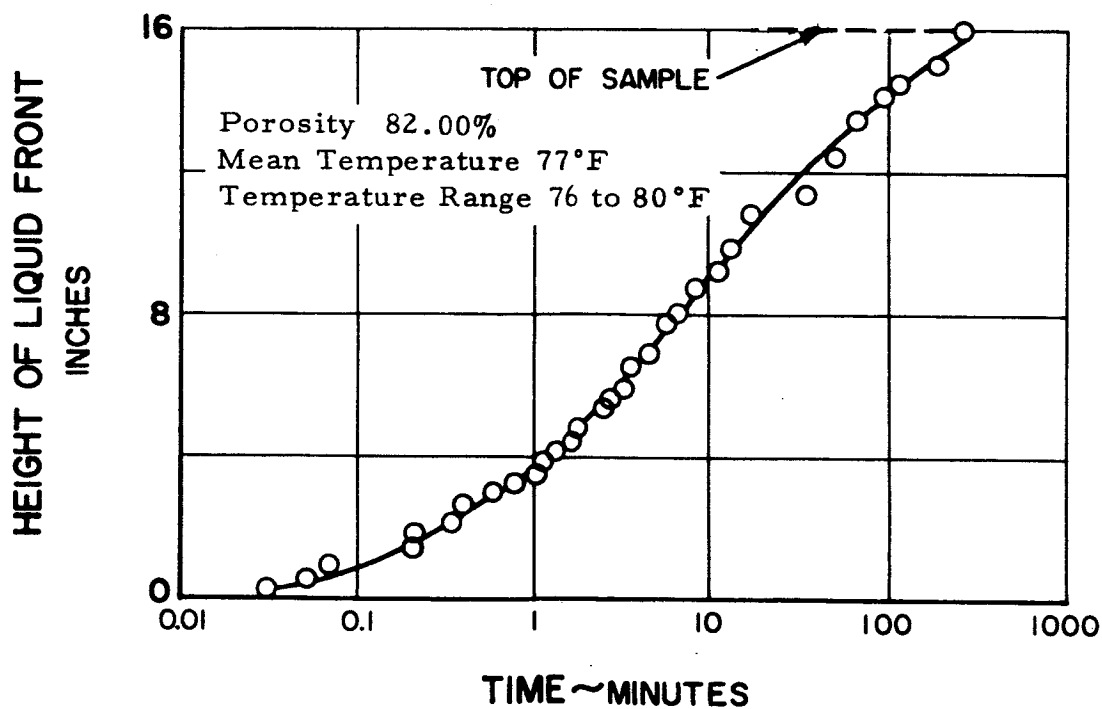


Figure 42 Water Wicking Curve for Sintered Nickel Fiber Sample H7

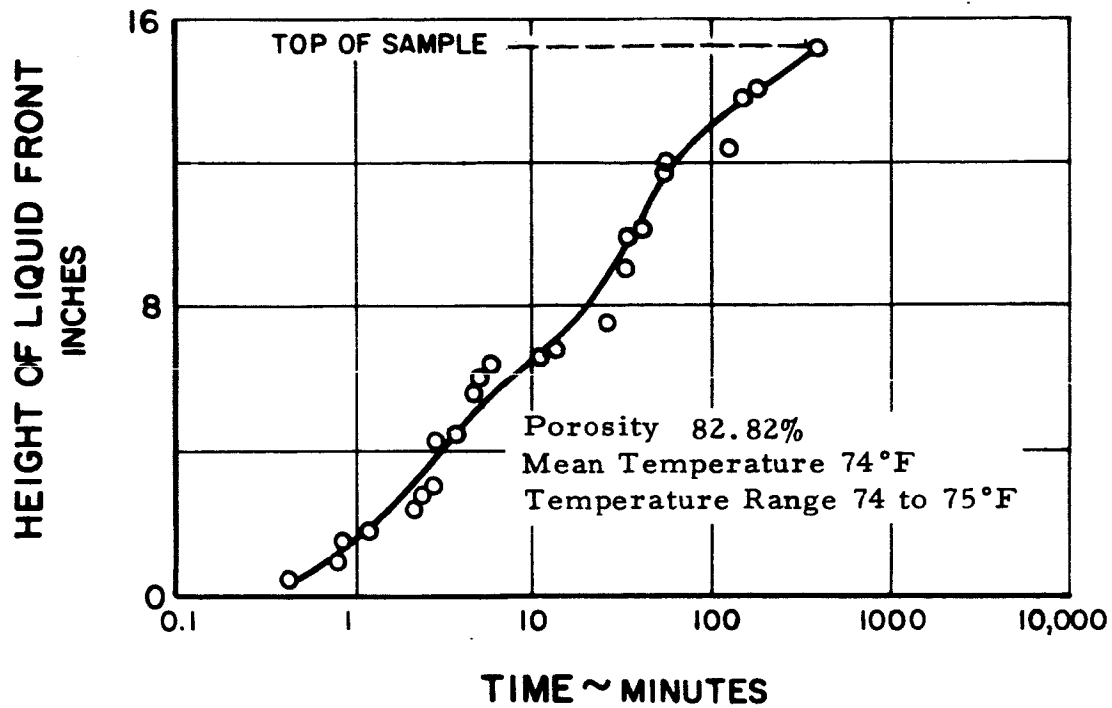


Figure 43 Water Wicking Curve for Sintered Nickel Fiber Sample H8

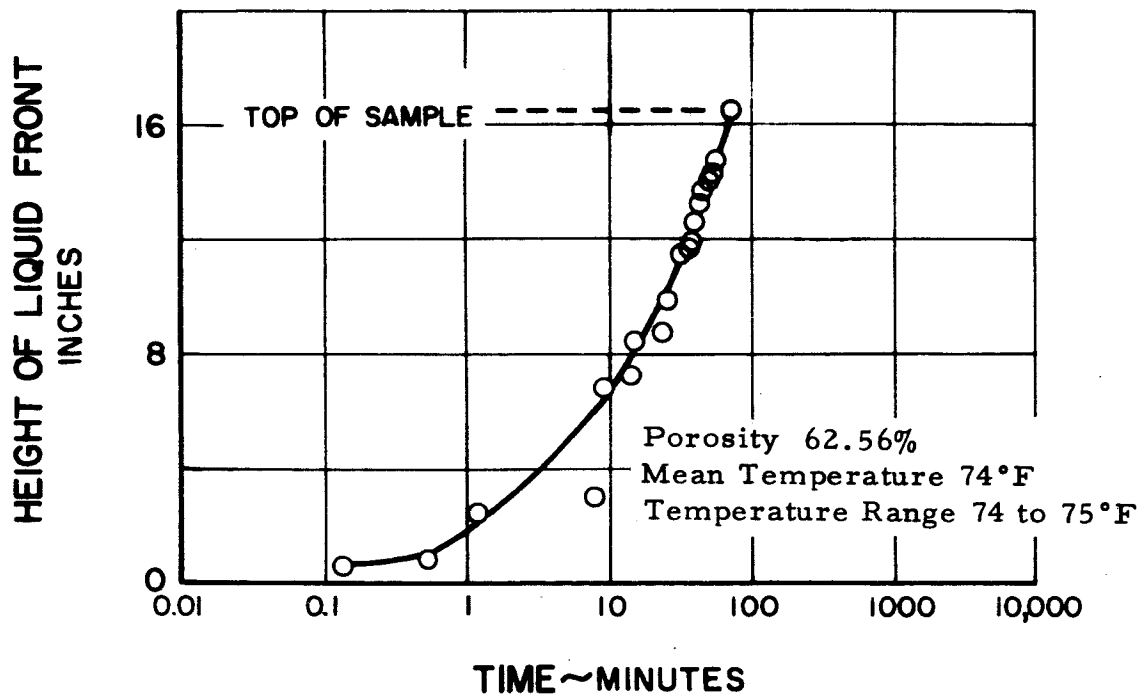


Figure 44 Water Wicking Curve for Sintered Nickel Fiber Sample H9

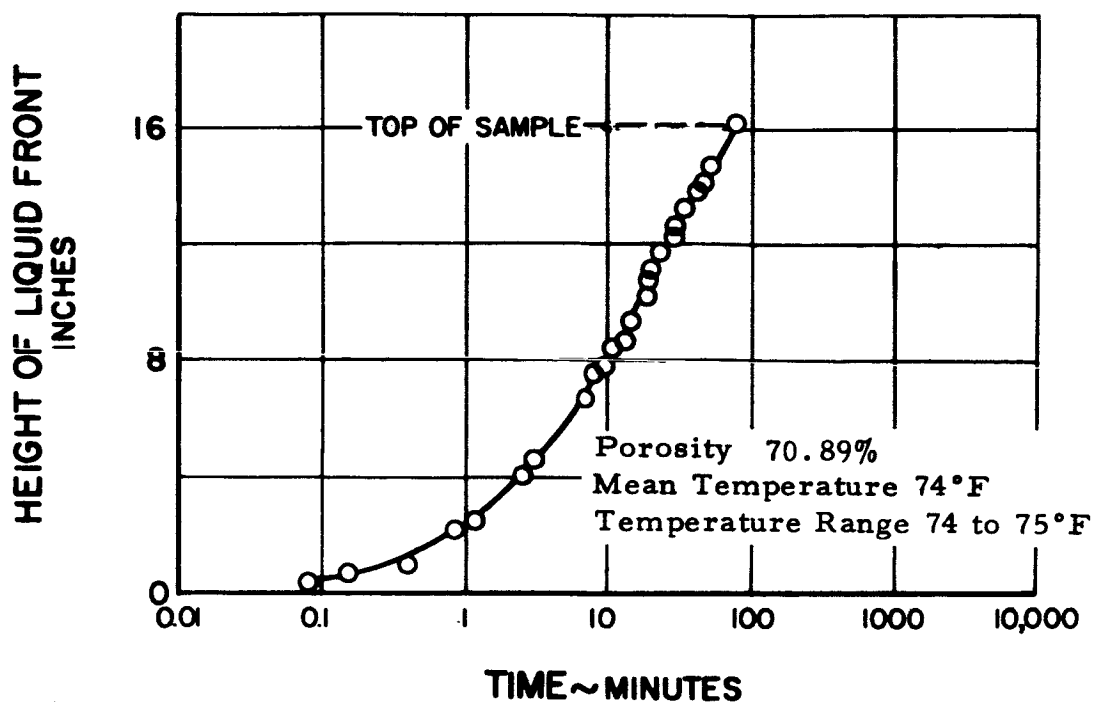


Figure 45 Water Wicking Curve for Sintered Nickel Fiber Sample H10

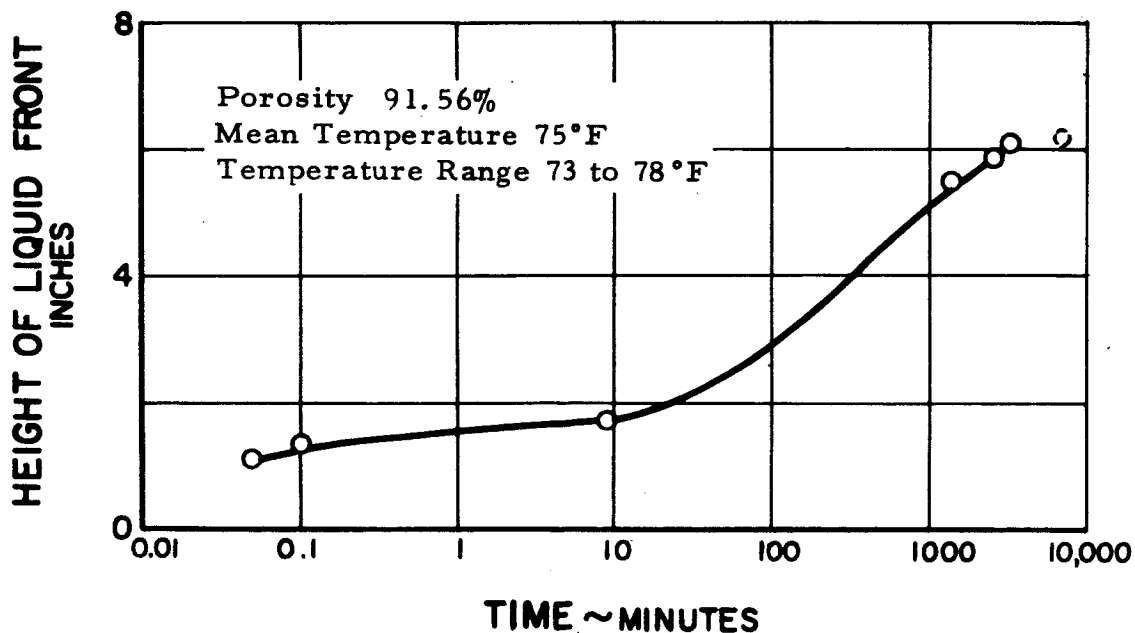


Figure 46 Water Wicking Curve for Sintered Stainless Steel Fiber Sample H11



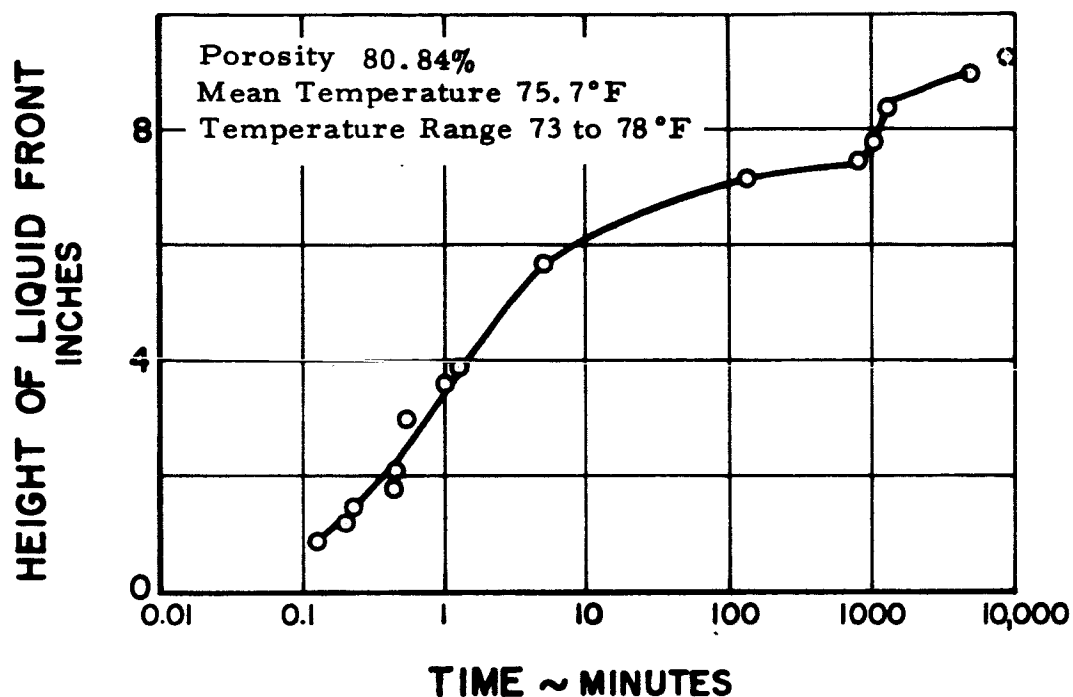


Figure 47 Water Wicking Curve for Sintered Stainless Steel Fiber Sample H12

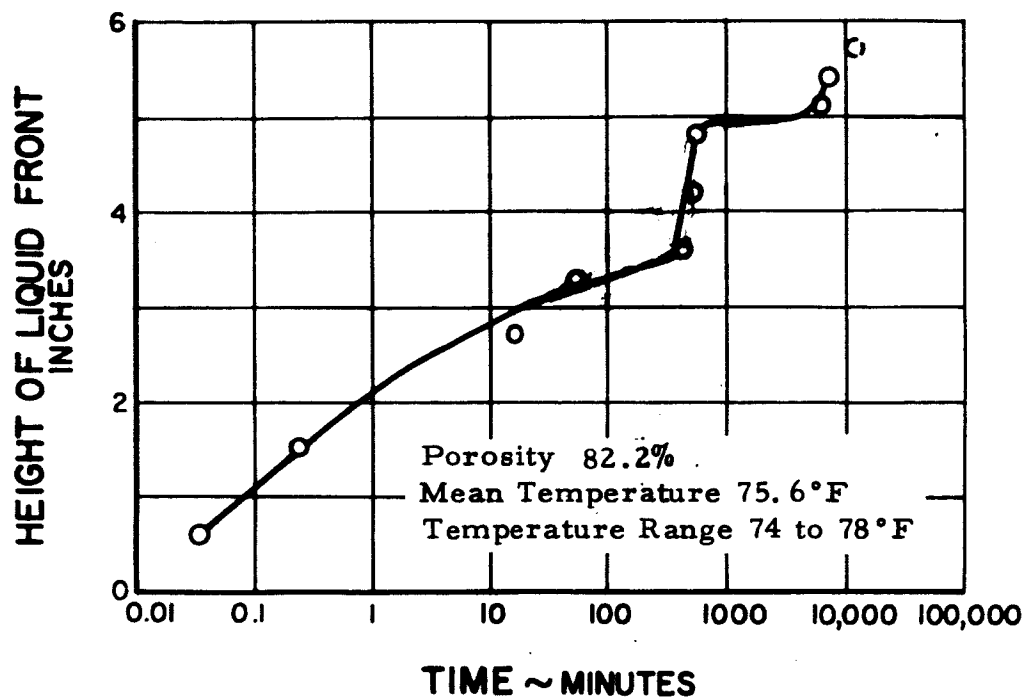


Figure 48 Water Wicking Curve for Sintered Stainless Steel Fiber Sample H13

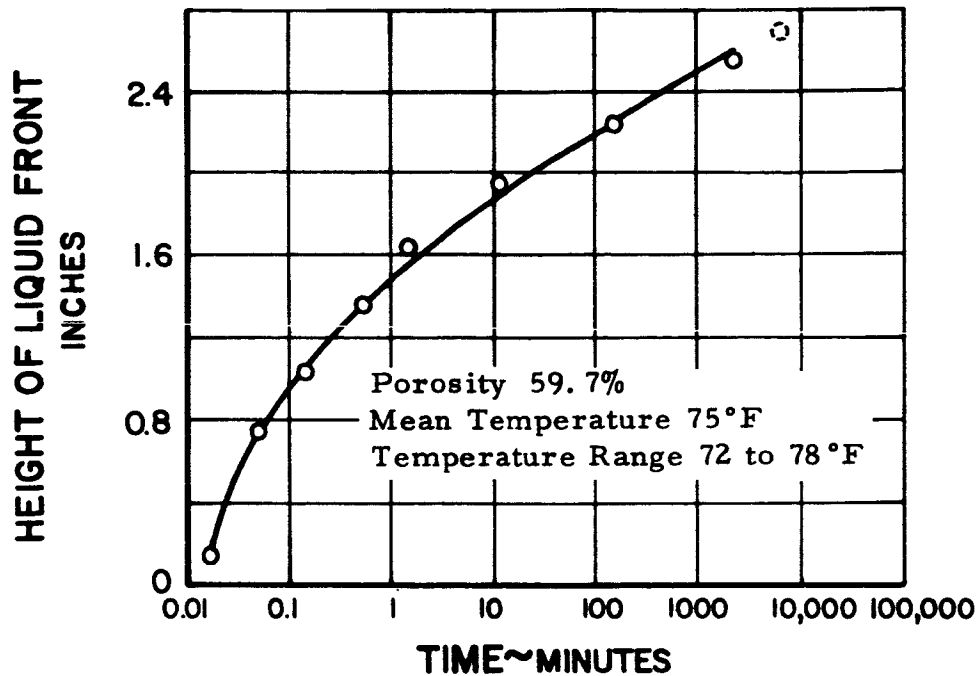


Figure 49 Freon 113 Wicking Curve for Sintered Nickel Powder Sample M1

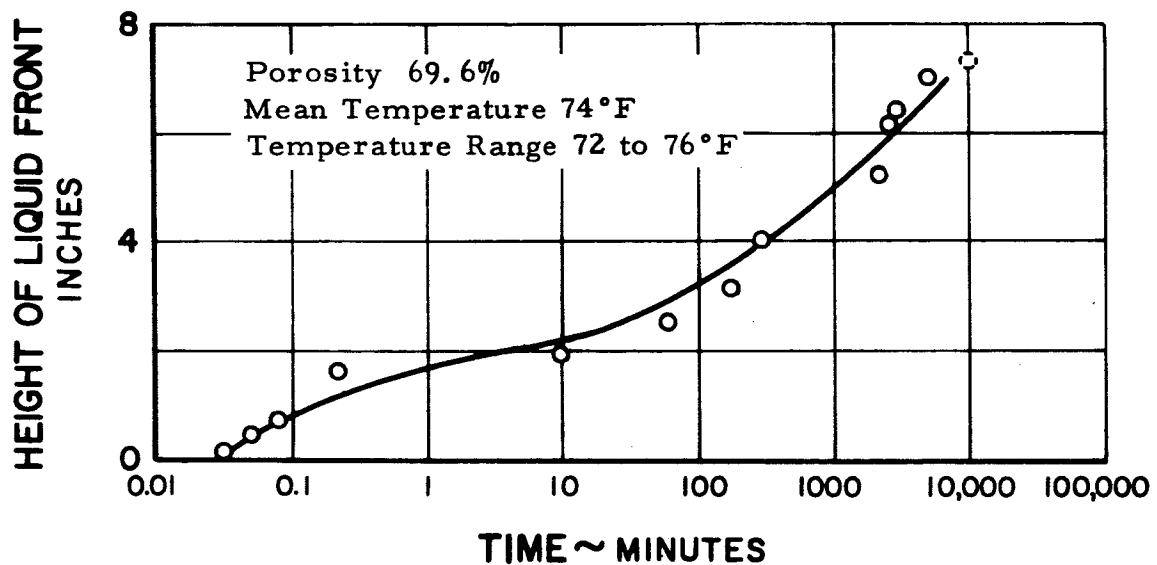


Figure 50 Freon 113 Wicking Curve for Sintered Nickel Powder Sample M4

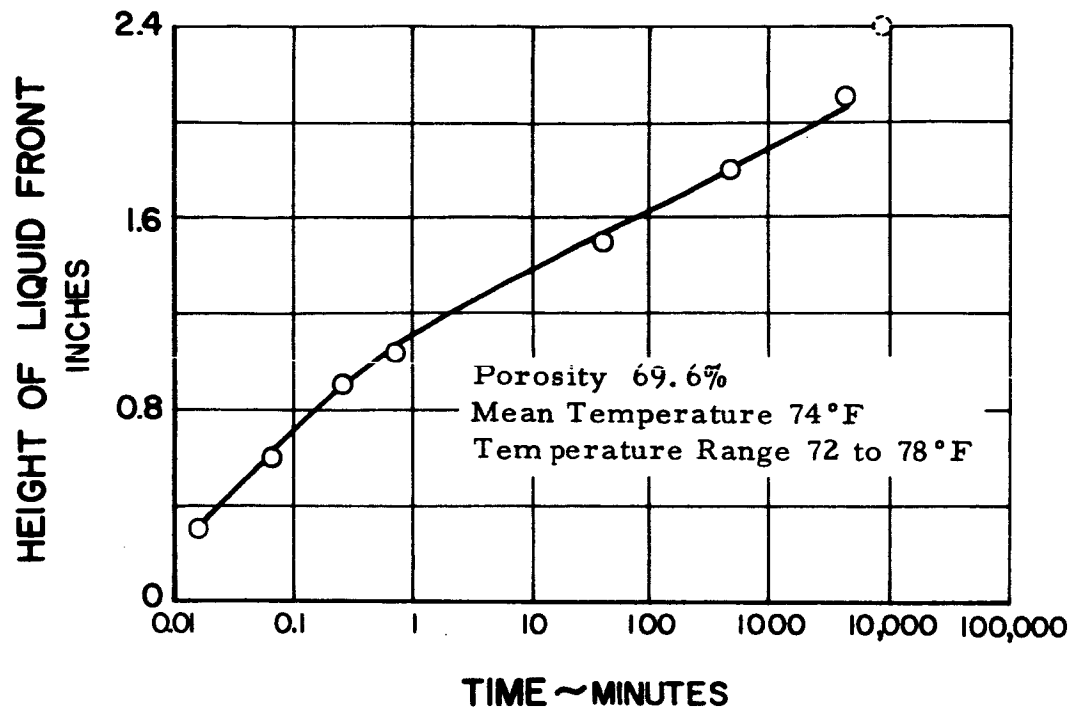


Figure 51 Freon 113 Wicking Curve for Sintered Nickel Powder Sample M6

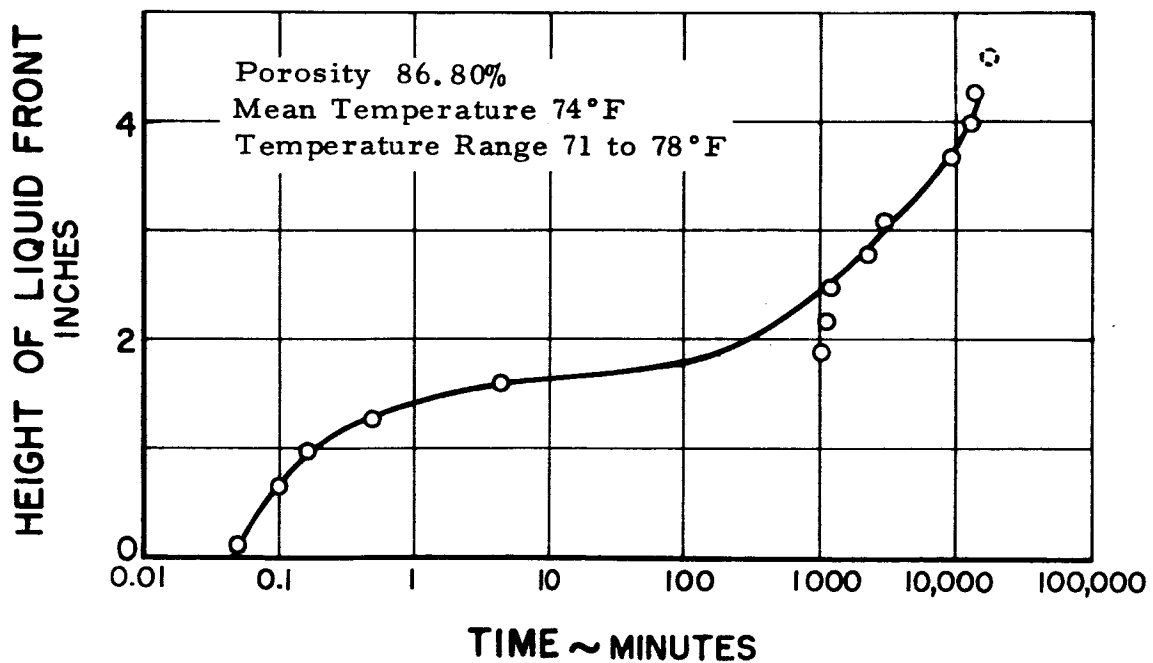


Figure 52 Freon 113 Wicking Curve for Sintered Nickel Fiber Sample H1

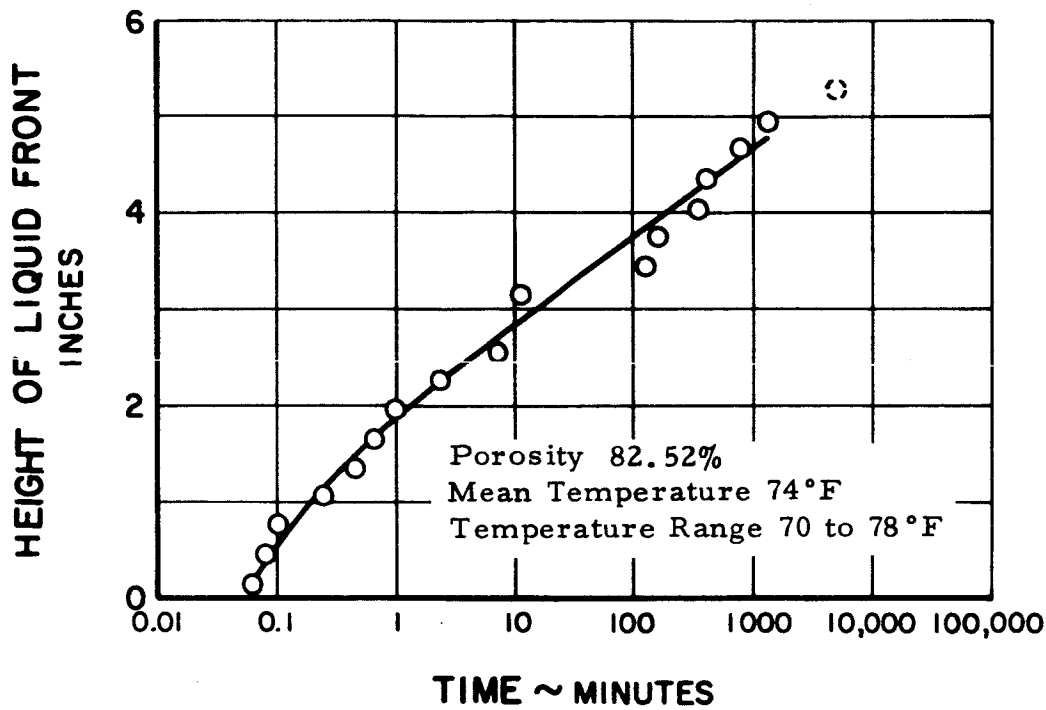


Figure 53 Freon 113 Wicking Curve for Sintered Nickel Fiber Sample H2

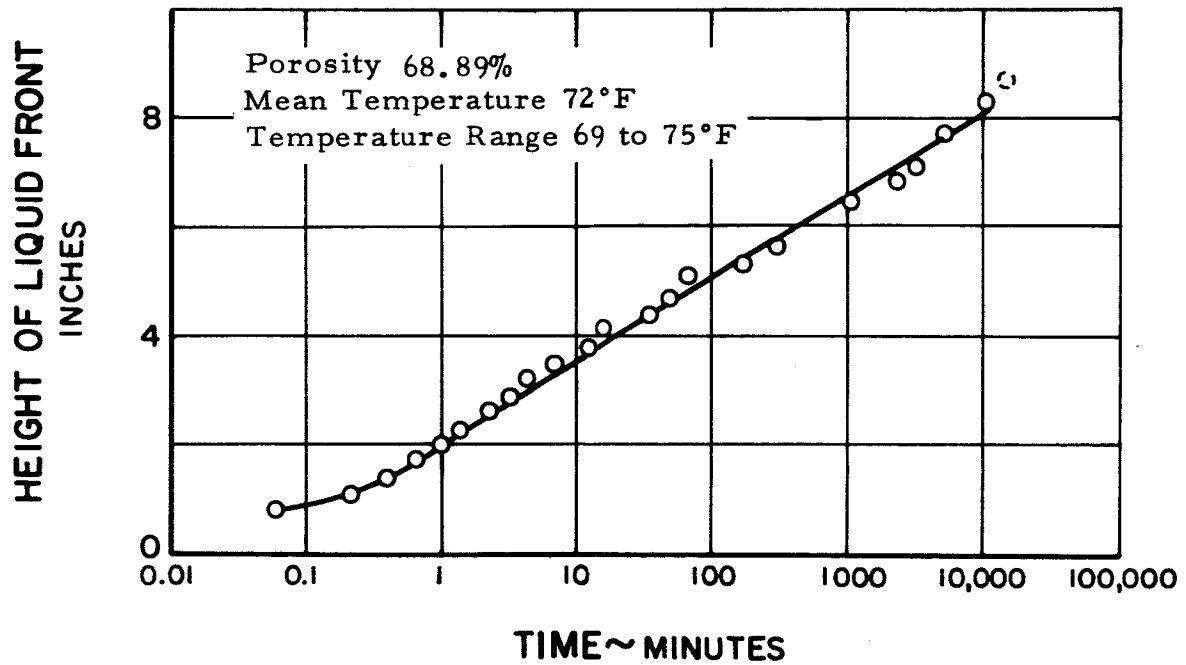


Figure 54 Freon 113 Wicking Curve for Sintered Nickel Fiber Sample H3

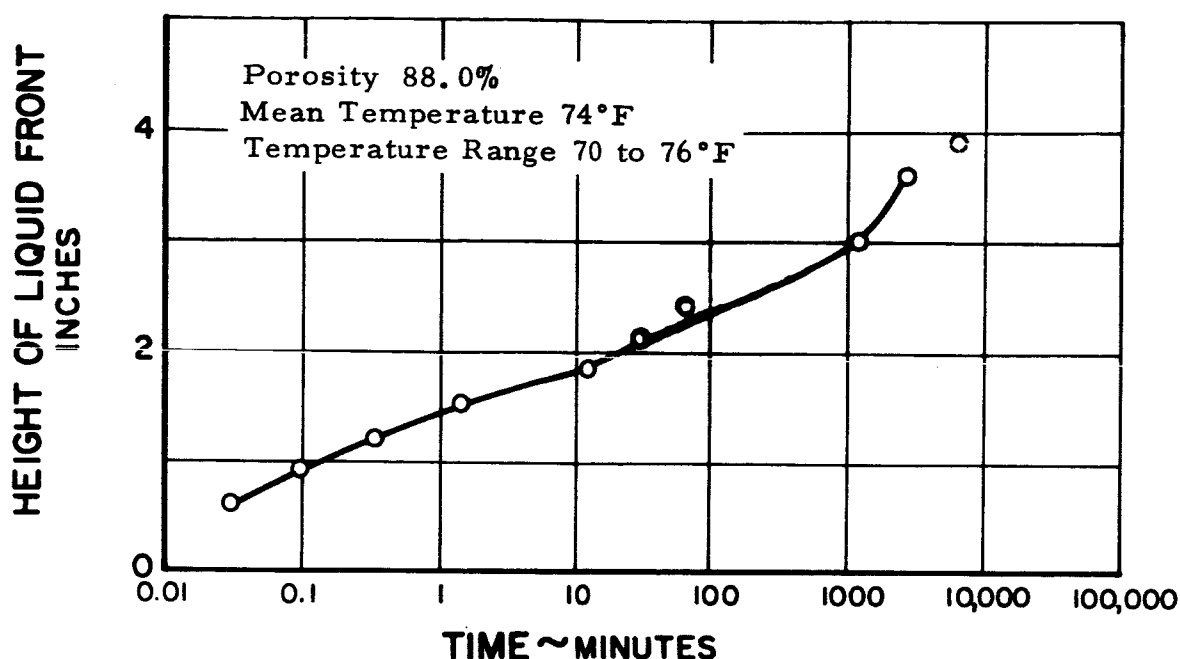


Figure 55 Freon 113 Wicking Curve for Sintered Nickel Fiber Sample H6

M1, M2, M4, M5, M6, M7, M8, M9, M10, H11, H12, H13 with water and all the tests involving Freon 113), the height of the first litmus paper above the liquid front and the time at which the test was terminated are indicated by a dotted circle.

No attempt was made to fit an analytical model to any of the rate of rise curves shown in Figures 27 to 55. This is because these curves do not present the true rate of rise of the liquid front in the sample, but are dependent on the speed with which the individual litmus paper strips respond to the presence of liquid front in the sample, especially at times near zero. Thus, the response time is the only reasonable explanation that can be offered for the large changes in slope shown in the wicking curves for Samples M4, M5, M8, M9, M10, H1, and H13 with water. However, this response time does not affect the final measured value of  $l_m$ .

The wicking characteristics of the porous materials under investigation are summarized in Table 7. The final equilibrium heights for the wicking tests utilizing water and Freon 113 are listed. The values listed show that the capillary forces in the sintered screen samples are relatively weak, while those associated with the sintered fiber samples are quite high, due presumably to the finer pore structure of the latter. The sintered powder samples are seen to be roughly intermediate between the other two classes of porous materials, although samples M3 and M4 because of their greater length had equilibrium heights greater than the sintered fiber samples.

TABLE 7

## Wicking Characteristics of Porous Materials

<u>Sample No.</u>	<u>(1<sub>m</sub>) water inches</u>	<u>(1<sub>m</sub>) Freon 113 inches</u>
M1	10.0	2.50
M2	10.19	--
M3	>16.20	--
M4	21.0	7.05
M5	8.40	--
M6	7.20	2.10
M7	2.10	--
M8	5.10	--
M9	6.90	--
M10	9.30	--
H1	>16.1	4.25
H2	>16.1	4.95
H3	>16.1	8.21
H4	>16.0	--
H6	>16.0	3.60
H7	>16.0	--
H8	>15.2	--
H9	>16.4	--
H10	>16.20	--
H11	6.15	--
H12	9.00	--
H13	5.40	--

The difference between equilibrium heights for the two liquids can be explained both in terms of the surface tension and the contact angle. As shown in the first quarterly report, the minimum radius of curvature that a wick can support is given by

$$R_{\min} = \frac{2g_c \sigma}{\rho_L g l_m} \quad (19)$$

where  $R_{\min}$  = minimum radius of curvature, and it is assumed that the meniscus is a segment of the surface of a sphere

$\sigma$  = surface tension  
 $\rho_L$  = density of the liquid  
 $g_c$  = proportionality constant in Newton's second law  
 $g$  = local acceleration of gravity

The radius of the pore in which the minimum radius occurs is

$$r_p = R_{\min} \cos \theta \quad (20)$$

where  $\theta$  is the contact angle between the liquid and the solid material of the wicking sample.

If it is assumed that the minimum radius of curvature occurs in the same size pores in both the water wicking tests and the Freon 113 wicking tests, then Equations (19) and (20) can be combined to arrive at an expression relating the equilibrium heights, given by

$$\frac{(l_m)_w}{(l_m)_F} = \left( \frac{\sigma_w}{\sigma_F} \right) \left( \frac{(\rho_L)_F}{(\rho_w)_w} \right) \left( \frac{(\cos \theta)_w}{(\cos \theta)_F} \right) \quad (21)$$

where the subscripts w and F refer to water and Freon 113 respectively.

If the contact angles associated with water and Freon 113 are assumed to be equal, and values of fluid properties are substituted, then Equation (21) becomes:

$$\frac{(l_m)_w}{(l_m)_F} = 5.46 \quad (22)$$

However, when the experimental values tabulated in Table 7 are used to calculate the equilibrium height ratio, the resulting values listed in Table 8 are less than those given by Equation (22). This would indicate that the contact angles in the water tests and the Freon 113 tests are not equal.

TABLE 8

## Comparison of Water and Freon 113 Wicking Tests

Sample No.	$\frac{(l_m)_w}{(l_m)_F}$	$\theta_w$ (Calculated), degrees	$(l_m)_w$ (Calculated), inches
M1	4.0	35	13.7
M4	2.98	53	38.5
M6	3.43	46	11.5
H1	> 3.79	< 39	> 23.2
H2	> 3.25	< 48	> 27.0
H3	> 1.96	< 66	> 44.8
H6	> 4.44	< 25	> 19.7

Freon 113 itself is an excellent solvent, which means that it has a contact angle of zero or near zero in a relatively clean wick. If it is assumed that  $\theta_F = 0^\circ$ , the contact angle of water in the wicking samples can be calculated using Equation (21) and the experimental values of the equilibrium height ratio. These calculated water contact angles which are listed in Table 8 show that the contact angle with water could have been as high as 53 degrees in some of the wicking materials.

Contact angle data given in Figure 3 of the second quarterly report shows that the contact angle formed between water and a clean pure nickel surface is about 42 degrees, while that formed between water and a clean nickel oxide surface is zero degrees. If the assumption used above that the minimum pore sizes are equal in both the water and Freon 113 tests is correct, then the non-zero value of  $\theta_w$  listed in Table 8 results from 1) a wick that was not truly clean, or 2) a wick in which the nickel was not completely oxidized. As outlined in Section IV.C., every effort was made to keep the samples clean. Also, each sample was air dried several times in an oven at 500°F for two hours, and appeared to be well oxidized (evidenced by a dark color and a dull finish) after each oven exposure. Thus no answer can be given as to which of the reasons, 1) or 2) above, was responsible for the apparent non-zero contact angles tabulated in Table 8.

Based on the Freon 113 data, the water equilibrium height that would have occurred had the contact angle been zero can be calculated from Equation (22). These values are listed in Table 8 and can be seen to be significantly higher than the experimental values given in Table 7. However, to evaluate each wicking material for use in a vapor-chamber fin experimental model, only the experimentally determined values of  $l_m$  listed in Table 7 will be used.



This is the most realistic approach to take because the wicking material that is used in the fin will be made and treated in the same way that the wicking samples were. Under these conditions, the experimentally determined value of  $l_m$  for a given fluid is the quantity that should be used in any fin design calculations.

#### E. Summary

To obtain data on the minimum liquid-vapor interfacial radius of curvature that a wick would support, tests were conducted to determine the final equilibrium height to which a liquid would rise in a wicking material. The wicking materials were chosen from the porous material samples listed in Section III. Two liquids, water and Freon 113, were used in the wicking rise tests.

In general it was found that the time necessary to reach an equilibrium height can be quite long, i. e., in the order of months. In some of the tests conducted, a true equilibrium height was not reached, and the test was terminated when the liquid front velocity fell below 0.1 inch per day.

In the tests involving water, it was found that capillary forces in the best wicking materials caused the water to rise rapidly to the top of the sample (16 inches). In poorer wicking samples the water front height was as low as 2.10 inches.

Wicking rise tests involving Freon 113 yielded equilibrium heights lower than those utilizing water, due primarily to the lower surface tension of Freon 113. Comparison of tests involving both liquids, showed that despite the oxidation and cleaning procedures followed, the contact angle in the water wicking tests could have been as high as 53 degrees.

## V. PERMEABILITY TESTS - TASK 1

A. Objective

The objective of the permeability tests is to evaluate the wick friction factor  $K_1$  and in particular the dependency of  $K_1$  on flow rate, temperature, and time for the porous materials described in Section III. The wick friction factor range of the metal wicks used in this study is compared to those of other porous materials in Table 9.

TABLE 9

## Flow Resistance of Various Porous Media

<u>Substance</u>	<u>Wick Friction Factor Range</u> <u><math>1/\text{ft}^2 \times 10^{-8}</math></u>
cork board	0.62 to 2.8 <sup>1</sup>
hair felt	0.77 to 1.1 <sup>1</sup>
cigarette	0.84 <sup>1</sup>
metal wicks (P&WA data)	0.75 to 61
sand (loose beds)	5.2 to 47 <sup>1</sup>
Fiberglas	18 to 39 <sup>1</sup>
soils	66 to 3,200 <sup>1</sup>
bituminous concrete	40 to 9,300 <sup>1</sup>
sandstone (oil sand)	310 to 1,900,000 <sup>1</sup>
agar-agar	2,100 to 47,000 <sup>1</sup>
leather	7,700 to 9,800 <sup>1</sup>
black slate powders	7,700 to 19,000 <sup>1</sup>
brick	4,200 to 190,000 <sup>1</sup>
silica powder	18,000 to 72,000 <sup>1</sup>
limestone, Dolomite	21,000 to 470,000 <sup>1</sup>

<sup>1</sup>Scheidegger, A. E., The Physics of Flow through Porous Media, Macmillan, 1960, p 87

## B. Description of Permeability Apparatus

### 1. Wick Samples

Thirteen different samples of the porous materials described in Section III. A. were selected on the basis of wicking rise data and tested in the permeability apparatus. Each sample was cut to the dimensions shown in Figure 56. The flow through the wicks was parallel to the three-inch dimension. The flow entrance and exit sections were cut by the electrochemical machining process described in Section III. C. The samples were oxidized before the permeability tests.

### 2. Test Assembly

Figure 57 is a schematic diagram of the permeability apparatus. The primary components include a mechanical pump which forces liquid to flow around a closed looped system, flowmeters to measure the flow through a sample, and U-tube manometers to measure the pressure drop across the sample. The wick sample is held in a wick holder and is enclosed by gaskets except at the inlet and outlet of the sample.

The only change in the system from the description given in the second quarterly report is the replacement of the slant-tube manometer with a U-tube manometer. The slant-tube manometer was found to react slowly with acetylene tetrabromide (specific gravity 2.9) and water as the fluids. By using a U-tube with diphosgene (specific gravity 1.65) and water as fluids the range of measurement and accuracy (Section V. E.) equivalent to the slant-tube manometer could be obtained.

## C. Test Results

The wick friction factor  $K_1$  was defined in the first quarterly report to be

$$K_1 = \left( \frac{A_c}{\Delta x} \right) \left( \frac{\rho_L}{\mu_L} \right) \left( \frac{\Delta P}{w_L} \right) \quad (23)$$

where  $A_c$  is the total flow cross-sectional area of the sample (i. e.,  $A_T$  in Equation (12) and not  $A_F$ )  
 $\Delta x$  is the length of the sample  
 $\rho_L$  and  $\mu_L$  are the liquid density and viscosity  
 $\Delta P$  is the pressure drop across the sample  
 $w_L$  is the liquid flow rate through the sample

The units of  $K_1$  are  $(1/\text{length})^2$ . The permeability is defined as the reciprocal of  $K_1$ .

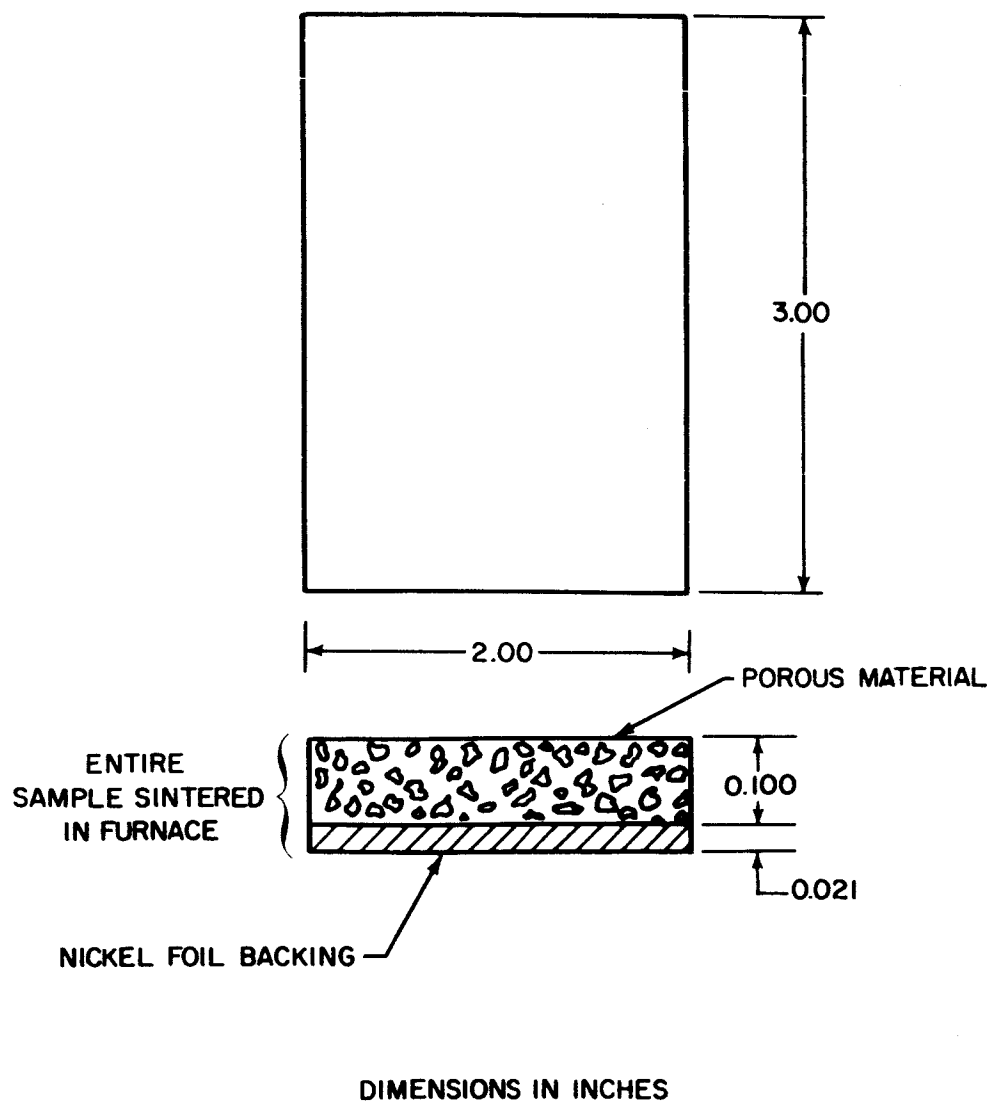


Figure 56 Dimensions of Permeability Samples

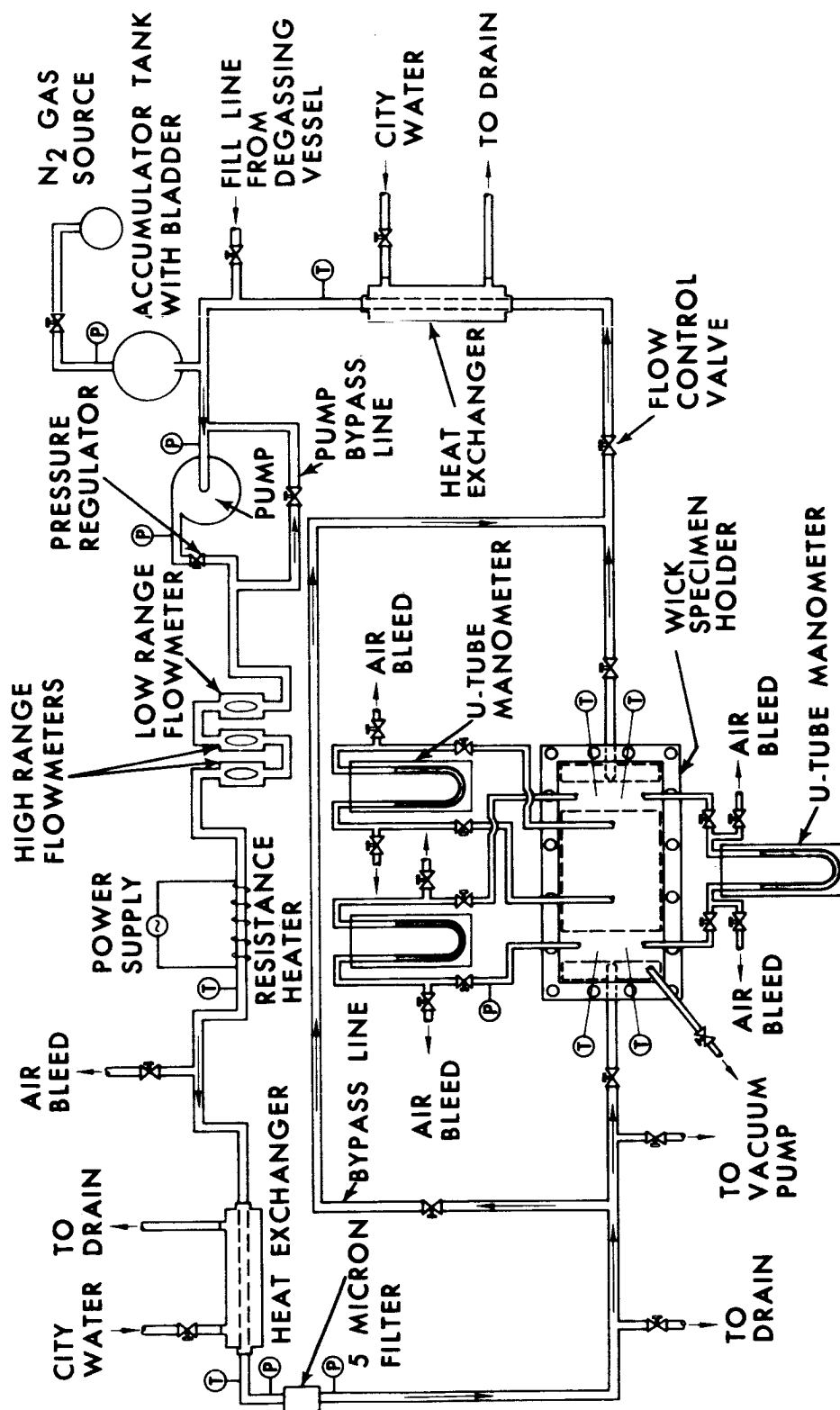


Figure 57 Schematic Diagram of Permeability Apparatus

The permeability results obtained with water on thirteen samples selected from those listed in Section III. A. are presented in Table 10 and Figures 58 to 62, in terms of the wick friction factor  $K_1$ .

The porosity listed in Table 10 with the samples tested may be slightly smaller than the porosity given in Section III for the respective samples. This is the result of a slight crushing of the softer samples when being installed between the gaskets of the wick holder. A slight deflection of the gaskets on the top and bottom of the sample is necessary to prevent any leaks, and on the softer porous materials the pressure associated with the gasket deflection caused some crushing. The effect of crushing has been accounted for in the porosity and permeability results presented in this section, by using the sample dimensions measured after the test.

TABLE 10

## Wick Friction Factor for Porous Material Samples

<u>Sample No.</u>	<u>Porosity, %</u>	<u>Wick Friction Factor <math>K_1 \times 10^{-8}, 1/\text{ft}^2</math></u>
H1	83.6	21.9
H2	81.4	27.6
H3	68.9	61.3
H6	86.9	30.2
H11	88.7	1.60
H12	80.7	4.75
H13	81.8	0.80
M2	64.5	3.5
M4	54.0	11.5
M6	69.6	3.1
M7	62.5	1.4
M8	58.5	6.1
M10	65.1	12.0

In the range of flow rates that are encountered in the vapor-chamber fin, Darcy's law<sup>1</sup> for flow through porous media will apply, meaning that  $K_1$  as given by Equation (23) should be independent of flow rate. Figures 58 to 61 show  $K_1$  vs flow rate per unit area (i. e., the flow rate  $w_L$  divided by the cross-sectional area  $A_c$ ) for different sintered screen samples, sintered powder samples, and sintered fiber samples. These figures demonstrate that for a certain range of flow rate per unit area,  $K_1$  is independent of flow rate.

<sup>1</sup>Scheidegger, A. E., The Physics of Flow through Porous Media, Macmillan, 1960, pp 68-90

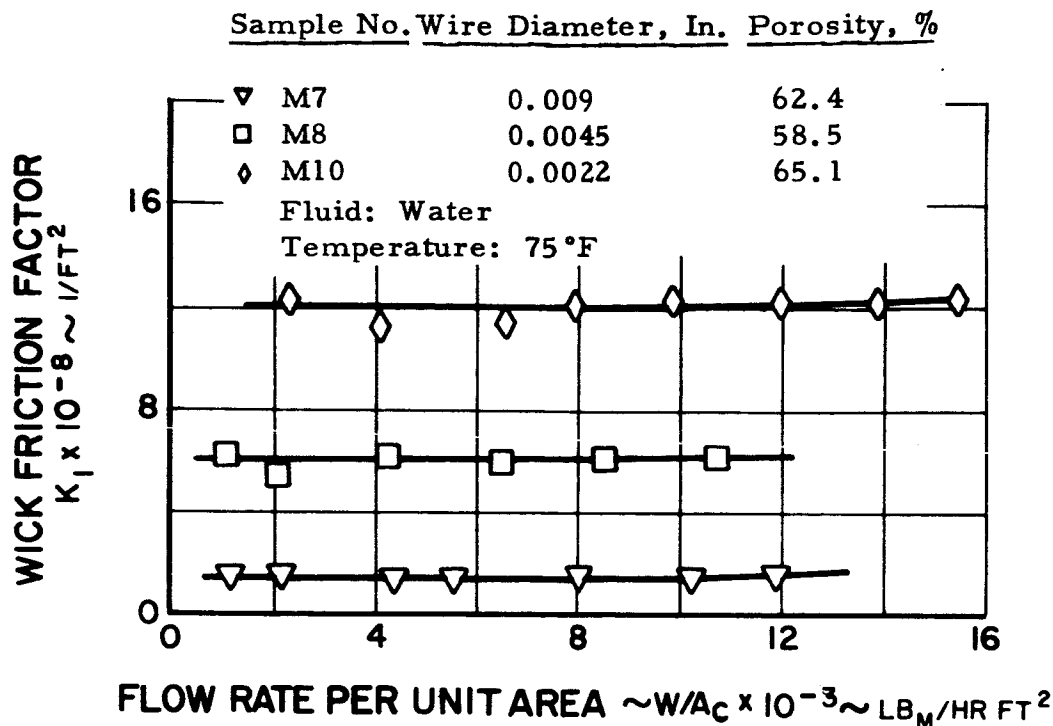


Figure 58 Wick Friction Factor vs Flow Rate per Unit Area for Sintered Nickel Screen Samples

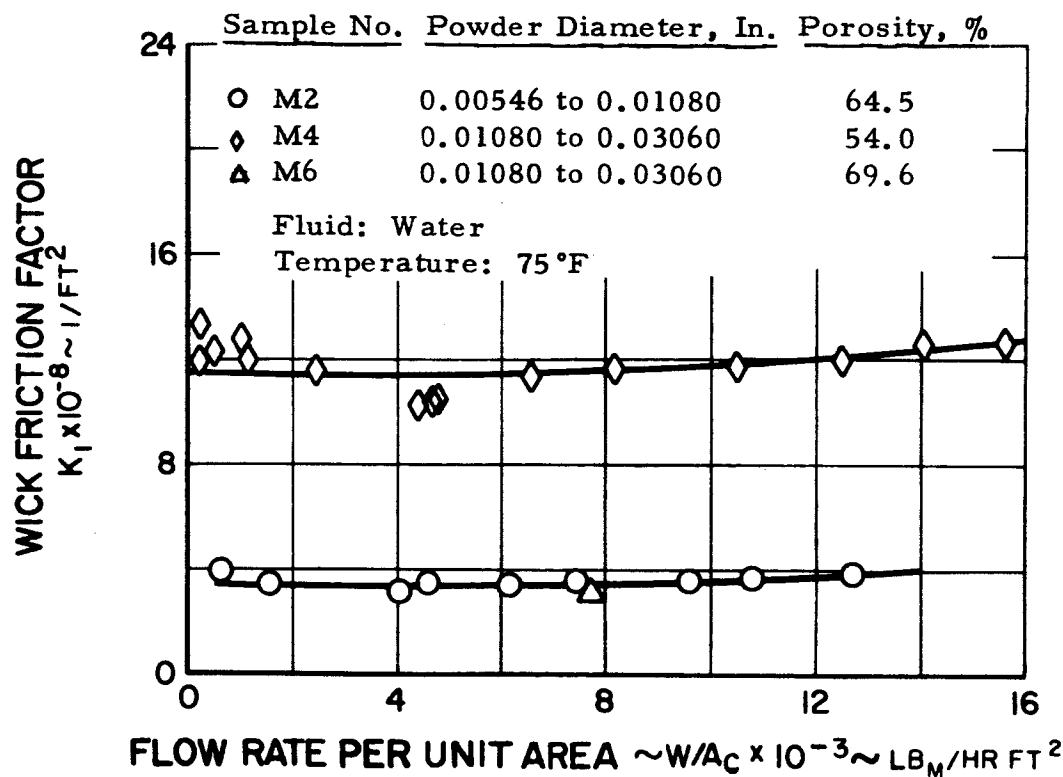


Figure 59 Wick Friction Factor vs Flow Rate per Unit Area for Sintered Nickel Powder Samples

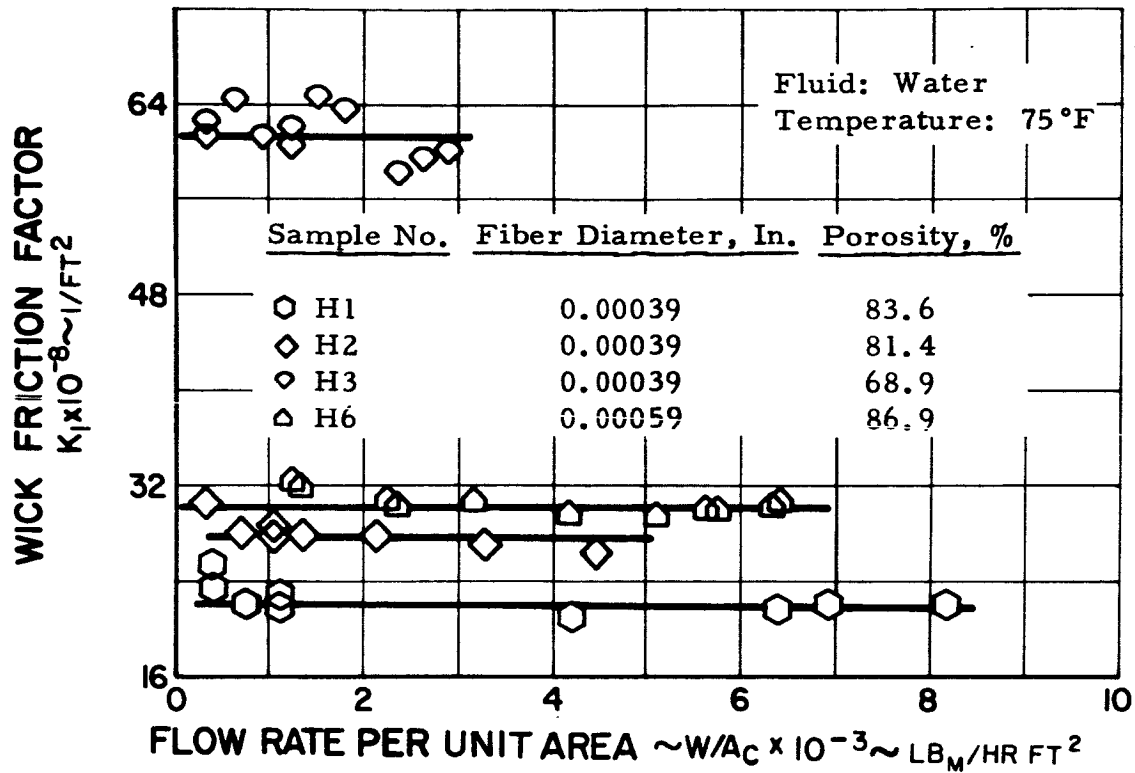


Figure 60 Wick Friction Factor vs Flow Rate per Unit Area for Sintered Nickel Fiber Samples

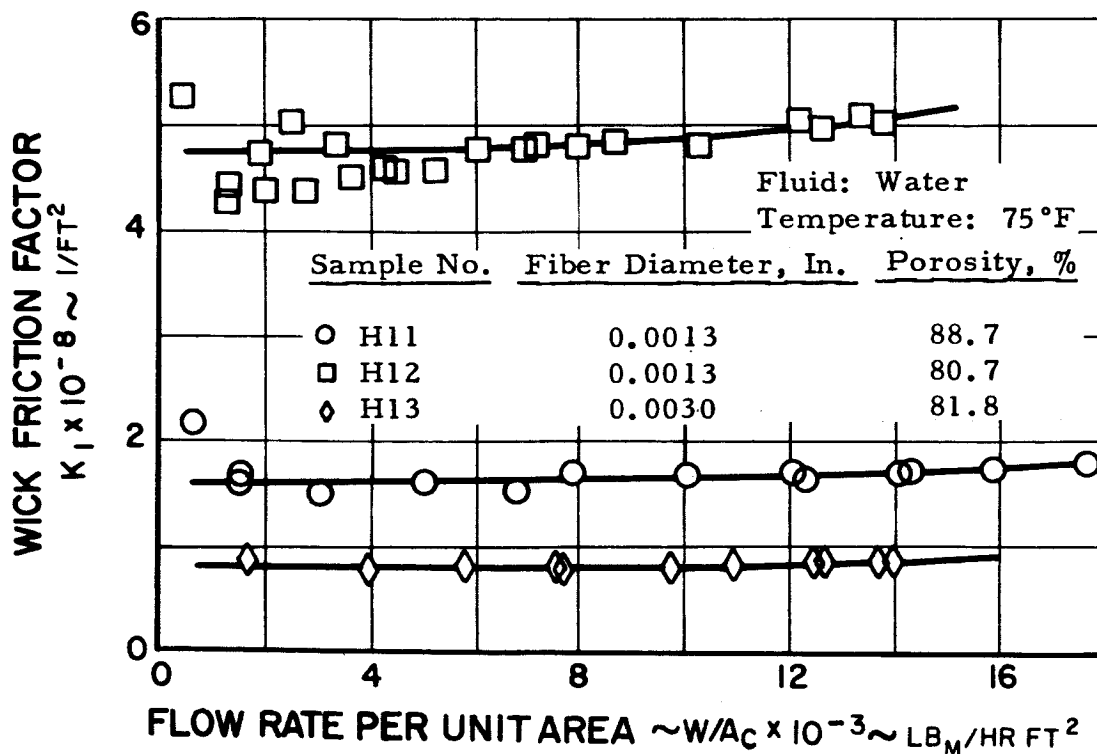


Figure 61 Wick Friction Factor vs Flow Rate per Unit Area for Sintered 430 Stainless Steel Fiber Samples



In interpreting these figures it should be noted that the points given at very low rates of flow per unit area become inaccurate for two reasons. First, the instrument for measuring flow rate for flow rates per unit area less than  $1 \times 10^3 \text{ lb}_m/\text{hr ft}^2$  becomes increasingly inaccurate as flow rate decreases. Second, the inaccuracy in measuring the pressure drop for samples with relatively low values of  $K_1$  becomes greater at low flows because of the small pressure drops. These two reasons account for the small scatter of points at the lower flow rates per unit area. Figures 58 to 61 clearly show that for these samples, flow rates per unit area up to  $9 \times 10^3 \text{ lb}_m/\text{hr ft}^2$  are definitely within the Darcy flow regime, where  $K_1$  is independent of flow rate.

For a few of the samples (M4, H11, H12, and H13),  $K_1$  increases slightly at flow rates per unit area above  $9 \times 10^3 \text{ lb}_m/\text{hr ft}^2$ . This increasing  $K_1$  indicates that the Darcy flow regime has been exceeded. Inside the Darcy flow regime friction causes the only pressure drop, and outside this regime (i. e., at higher flows) inertia effects resulting in drag forces start to enter as a pressure drop component, causing  $K_1$  to increase.

A Reynolds number for this purpose may be defined as

$$\text{Re} = \frac{\rho_L u_L D_{\text{med}}}{\mu_L} \quad (24)$$

Where,  $\rho_L$  and  $\mu_L$  - are the liquid density and viscosity

$u_L$  - is the flow velocity in the sample based on the area  $A_c$

$D_{\text{med}}$  - is the median pore diameter listed in Section III. B.

The Reynolds number corresponding to the upper flow limit of  $9 \times 10^3 \text{ lb}_m/\text{hr ft}^2$  is between 0.2 and 3.0, depending on the porous sample.

Figure 62 is a plot of wick friction factor vs fluid temperature of several different samples for tests with water. For the temperature range of 75 to 160°F the friction factor remained constant while the liquid viscosity changed by a factor greater than two. This shows that in the range tested,  $K_1$  as given in Equation (23) is independent of temperature. Permeability tests will be run during the next quarter using Freon 113 to verify that  $K_1$  is independent of fluid properties.

In the second quarterly report  $K_1$  was shown to be independent of test time. Summarizing the above, it has now been shown that  $K_1$  is also independent of flow rate within the Darcy flow regime and independent of temperature. The data presented in Figures 58 to 61 also provide information on the upper limit of the Darcy flow regime. One test, that of using another test liquid, remains to show that the wick friction factor as defined and measured is a property of the porous material only.

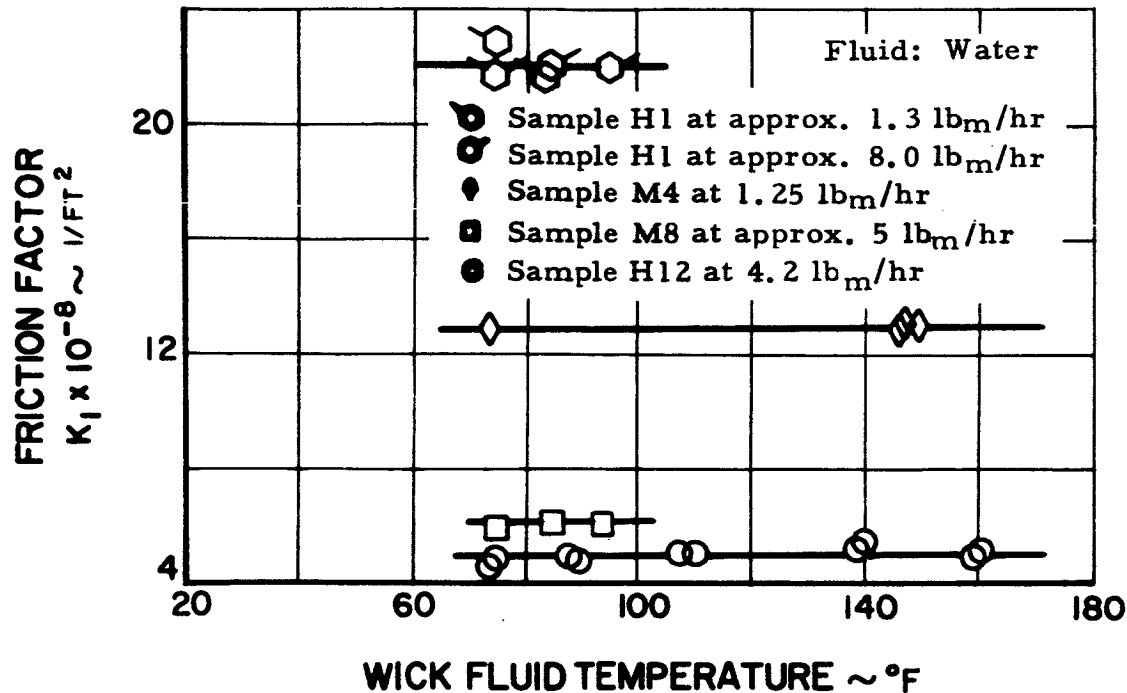


Figure 62 Wick Friction Factor vs Temperature for Sintered Metal Wicks

#### D. Accuracy of Permeability Results

To determine  $K_1$  as defined in Equation (23), pressure drop data was taken for two lengths of the sample: the entire sample length of about three inches, and an internal length of about two inches. The nominal three-inch dimension of the sample was measured within  $\pm 1$  per cent. However, the cut entrance and exit sections of the wicks were not always perpendicular to the nominal three-inch dimension, and for some samples a taper of 10 degrees from the perpendicular exists, caused by the cutting process. Because this taper may cause a slight flow maldistribution at the sample entrance and exit, data from both lengths are compared in Figure 63, demonstrating the usual variation of less than  $\pm 3$  per cent. The nominal two-inch dimension is fixed by the construction of the pressure

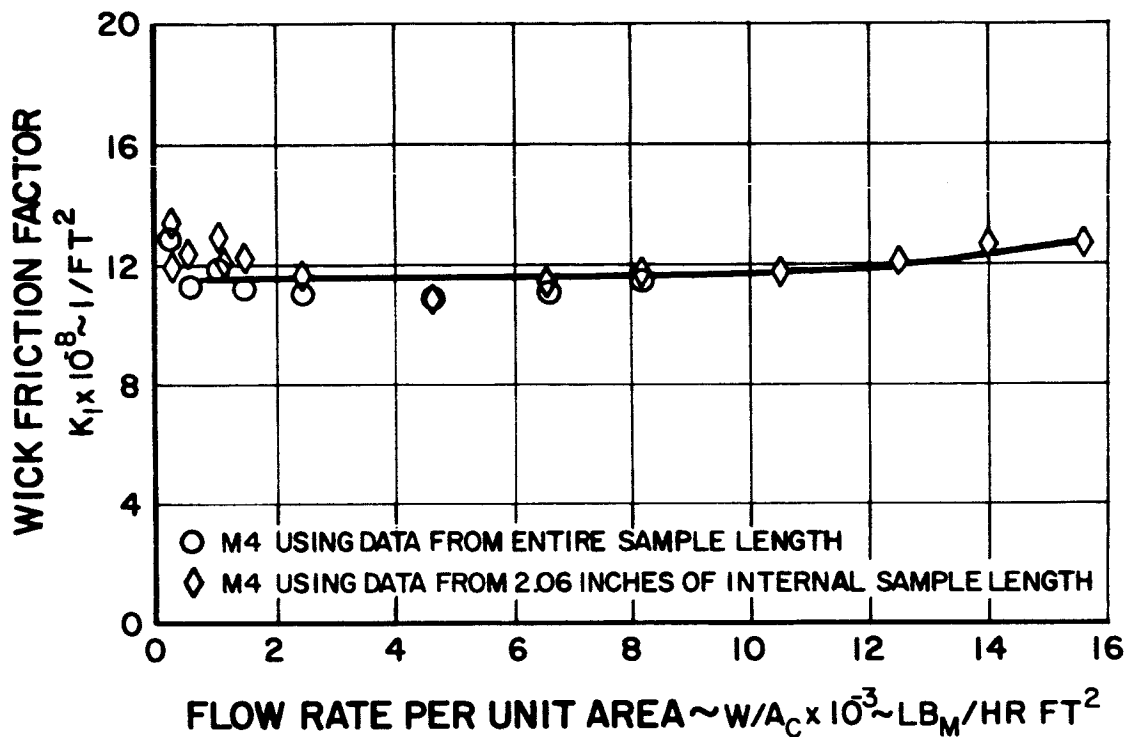


Figure 63 Wick Friction Factor for Sample M4 vs Flow Rate Using an Internal and External Sample Length

taps in the sample wick holder, as shown in Figure 64. The actual measurement was 2.06 inches.

The accuracy of  $K_1$  determined with the permeability apparatus is summarized in Table 11. The table includes the accuracy of all parameters used in calculating  $K_1$  from Equation (23). All of the results of  $K_1$  presented in the previous sections were calculated from two-inch data instead of the three-inch data because it was possible to include a higher flow range with the smaller pressure drops across the two-inch dimension. For the samples with  $K_1 > 4.0 \times 10^8 \text{ 1/ft}^2$  the results of  $K_1$  are accurate within 9.8 per cent for flow rates per unit area above  $4.4 \times 10^3 \text{ lb}_m/\text{hr ft}^2$  and within 5.3 per cent for flow rates per unit area above  $7.3 \times 10^3 \text{ lb}_m/\text{hr ft}^2$ . For the samples with  $K_1 < 4.0 \times 10^8 \text{ 1/ft}^2$  the accuracy of  $K_1$  is 9.8 per cent for flow rates per unit area above  $1.4 \times 10^3 \text{ lb}_m/\text{hr ft}^2$  and 5.3 per cent for flow rates per unit area above  $2.3 \times 10^3 \text{ lb}_m/\text{hr ft}^2$ .

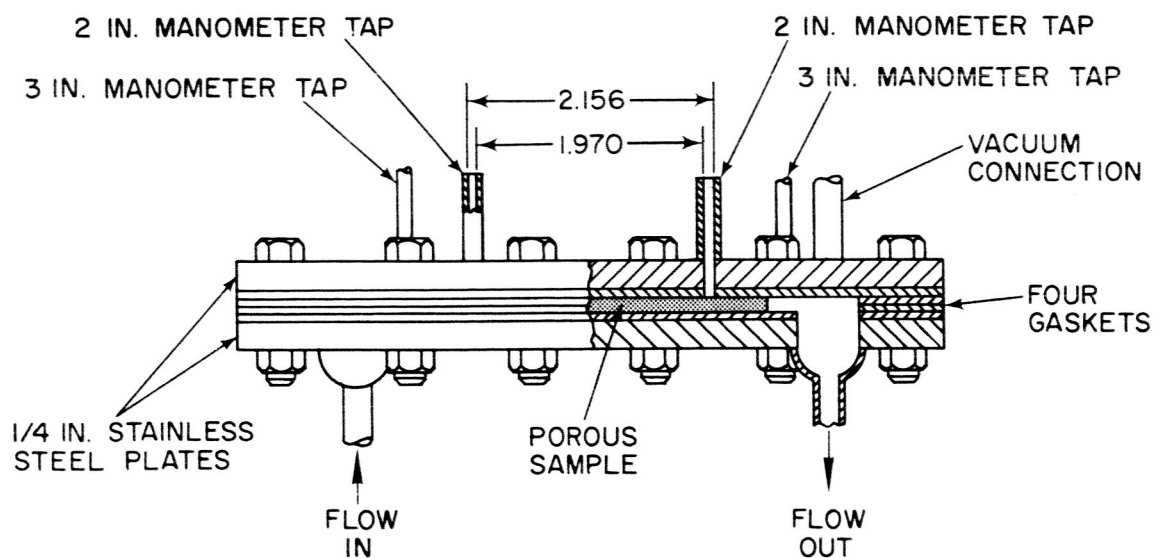
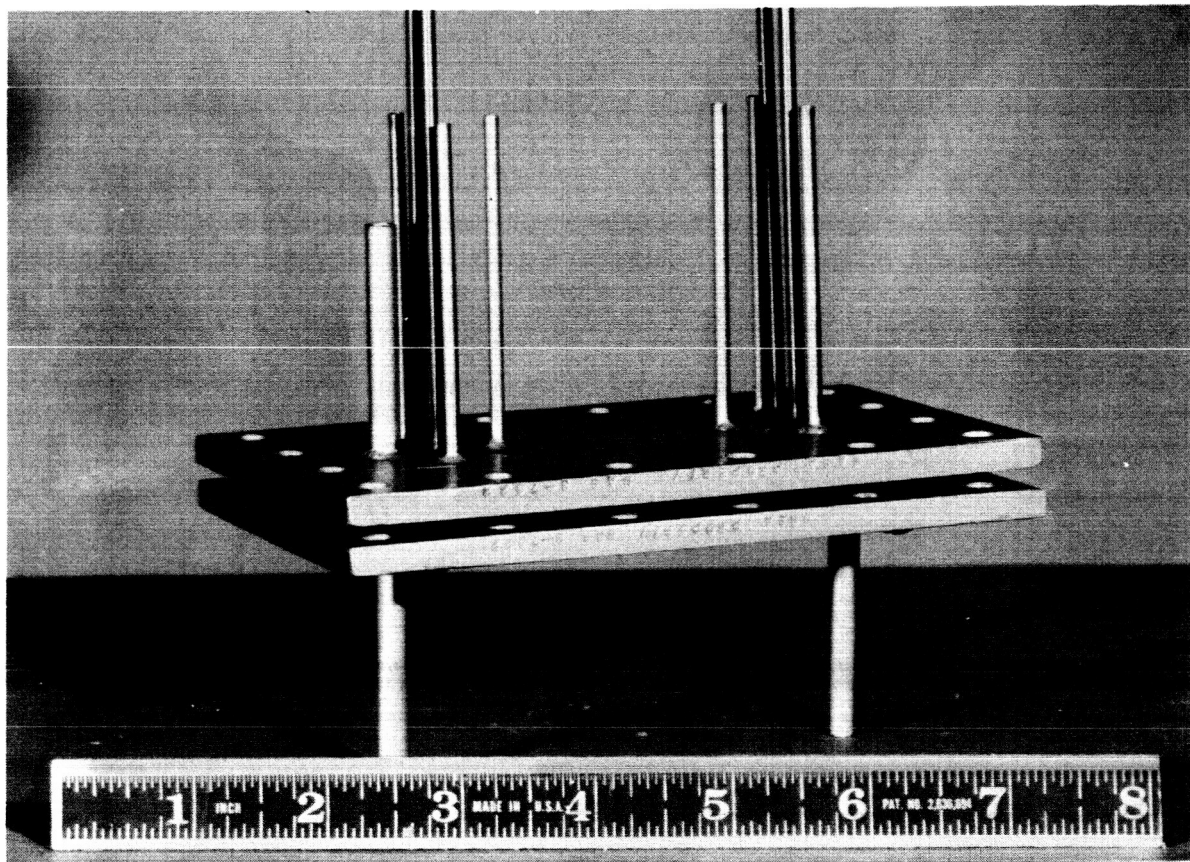


Figure 64 Photograph and Sketch of Wick Permeability Sample Holder Showing Pressure Taps

TABLE II  
Accuracy of Wick Friction Factor,  $K_1$

Parameter or Dimension	Accuracy of 3-Inch Results		Accuracy of 2-Inch Results	
	Magnitude	Uncertainty	Magnitude	Uncertainty
density (H <sub>2</sub> O at 75°F) lbm/ft <sup>3</sup>	62.2	<±0.1	62.2	<±0.1
viscosity (H <sub>2</sub> O at 75°F) lbm/ft sec	0.616	±0.01	0.616	±0.01
length, Δx inches	3.00 <sup>1</sup>	±0.020	2.060	<±0.01
cross-section area, A <sub>c</sub> (inches) <sup>2</sup>	0.20 <sup>1</sup>	±0.002	0.20 <sup>1</sup>	±0.002
flow rate	Flowmeter Reading			
flowmeter No. 1				
0.41 lb <sub>m</sub> /hr	10.5	±0.1		
1.24 lb <sub>m</sub> /hr	18.8	±0.1		
flowmeter No. 2				
1.24 lb <sub>m</sub> /hr	5.0	±0.25		
3.84 lb <sub>m</sub> /hr	9.5	±0.25		
12.2 lb <sub>m</sub> /hr	22.0	±0.1		
pressure drop	U-Tube Reading		U-Tube Reading	
0.056 psi	2.50"	±0.05"	0.79"	±0.05"
0.111 psi	5.00"	±0.05"	1.57"	±0.05"
0.666 psi	30.0"	±0.05		

TABLE 11 (Cont'd)

Parameter or Dimension	Accuracy of 3-Inch Results		Accuracy of 2-Inch Results	
	Magnitude	Uncertainty	Magnitude	Uncertainty
pressure drop	U-Tube	Per cent		Per cent
	Reading	Uncertainty		Uncertainty
0.666 psi	9.4"	±0.05	9.4"	±0.05"
2.12 psi	30.0"	±0.05	30.0"	±0.05"
wick friction factor, K <sub>1</sub>				
for all flows from 0.41 lb <sub>m</sub> /hr to 12.2 lb <sub>m</sub> /hr and for ΔP of 0.056 psi to 2.12 psi		±0.53% < ±0.50%		±0.53% < ±0.50%
for flows > 3.84 lb <sub>m</sub> /hr and ΔP > 0.111 psi		≤ ±7.75% <sup>3</sup>		≤ ±9.75% <sup>3</sup>
		≤ ±4.26% <sup>3</sup>		≤ ±5.27% <sup>3</sup>

1 The exact magnitude varied slightly in different samples  
2 These uncertainties take into account the instrument accuracy and the calibration error  
3 These uncertainties are obtained from the square root of the sum of the uncertainties squared for the parameters in Equation (23)

### E. Summary

The wick friction factor  $K_1$  of each of thirteen of the samples listed in Section III was measured and was found to range from  $0.80 \times 10^8 \text{ 1/ft}^2$  for a high-porosity sintered fiber sample to  $61.3 \times 10^8 \text{ 1/ft}^2$  for a low-porosity sintered powder sample.

The wick friction factor values were determined in a range of flow rates where  $K_1$  was independent of the flow rate, i. e., the Darcy flow regime. The wick friction factor was also found to be independent of liquid temperature. None of the samples tested showed any observable end effects on the measured value of  $K_1$ .

## VI. WICK BOILING TESTS - TASK 2

### A. Objective

The objective of the boiling tests is to measure the following quantities while boiling from a wick-covered surface:

- 1) the variation of heat flux  $q$  with  $\Delta T_{\text{sat}}$ , the temperature at the liquid-wick-solid interface minus saturation temperature,
- 2) the maximum heat flux that can be sustained before film boiling occurs, and
- 3) the variation of limiting heat flux and  $\Delta T_{\text{sat}}$  vs  $q$  curves with wick material, boiling fluid (water or Freon 113), wick orientation with respect to gravity, and degree of wick saturation.

The results will be interpreted to determine limitations on fin operation imposed by the boiling region of the fin. The heat transfer coefficient  $q/\Delta T_{\text{sat}}$  will be obtained over a range of heat fluxes. The following sections contain a description of the apparatus used to accomplish these objectives and the results obtained to date.

### B. Description of Boiling Apparatus

#### 1. Overall Design

A sketch of the boiling primary tank is shown in Figure 65, and a photograph of the overall rig in Figure 66. The flat test sample to be evaluated is bonded with an electrical insulator to a resistance heater which is mounted on copper busbars. The bottom of this heater is firmly pressed against insulating blocks by means of busbar adjusting screws. The insulating blocks, two of which have a Nichrome guard heater sandwiched between, rest on a Textolite platform which is mounted in the stainless steel primary tank. The Plexiglas cover and Neoprene gasket are used to prevent spillage during the tests in which the primary tank is tilted. The large surface area of the secondary tank which feeds the primary tank, limits the change in liquid height with time to a negligible value.

#### 2. Sample-Heater Assembly

The wick boiling samples consist of a piece of porous nickel or stainless steel 2.875 by 0.625 by 0.100 inch thick bonded to a backup plate of the



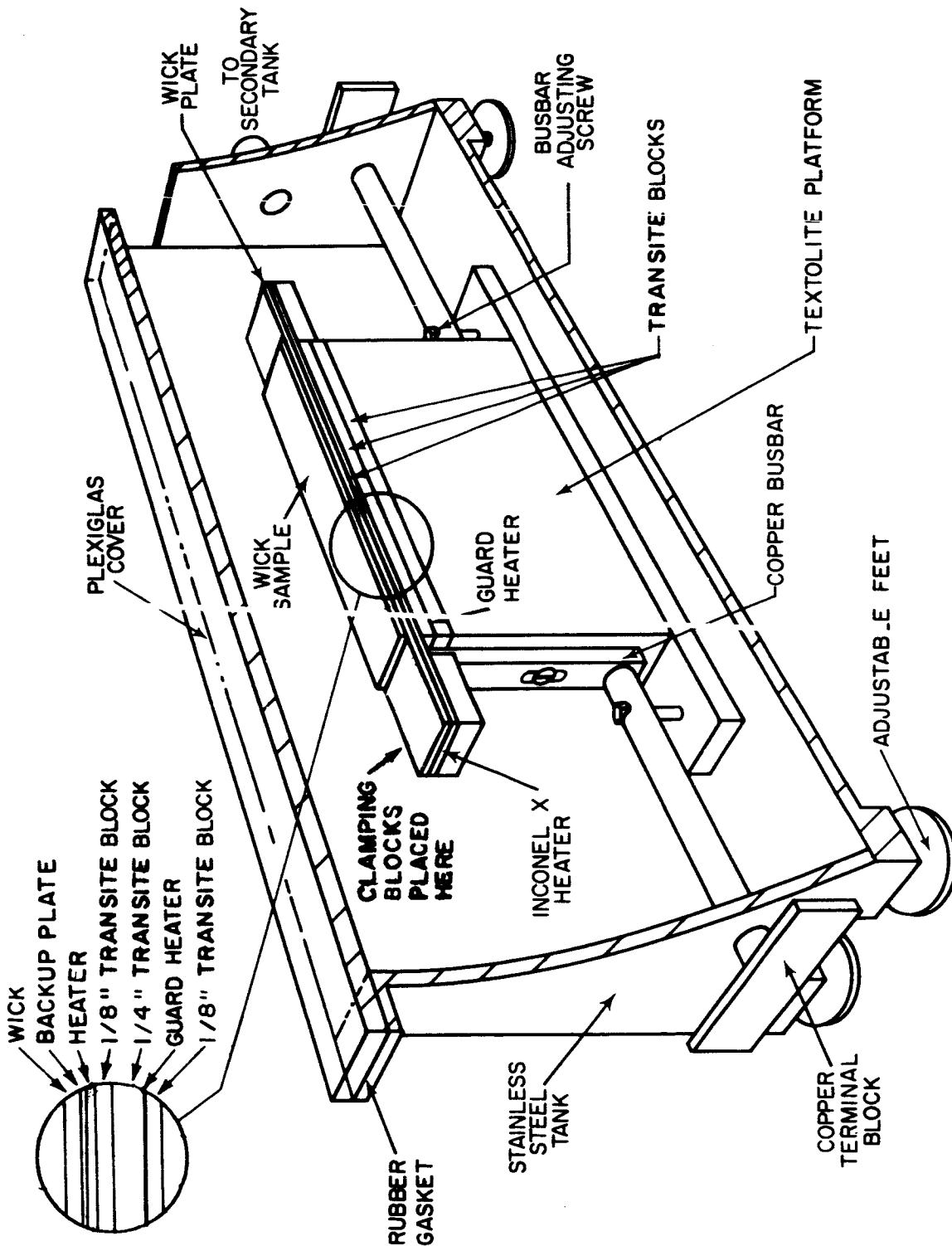


Figure 65 Cutaway View of Boiling Test Apparatus

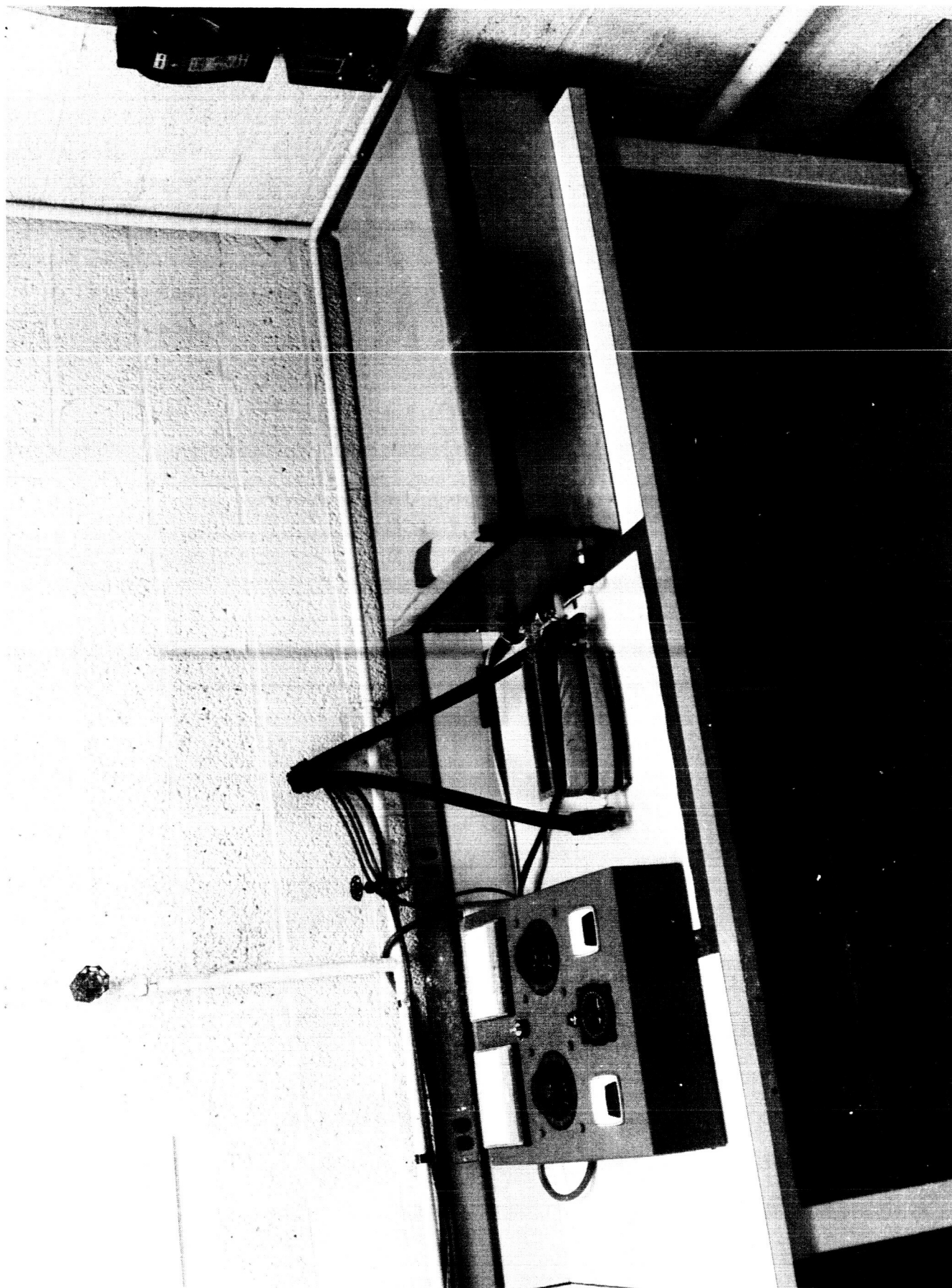


Figure 66 Wick Boiling Experimental Test Setup Showing Control Panel, Primary Tank, and Secondary Tank

same material. The samples are cut from the wicks such as those shown in Figures 1 to 8 by electrochemical machining. Since a wick boiling sample is small in size, there should be little resistance to fluid flow in the wick. Hence, for tests in which the sample is horizontal with respect to the surface of the water, failure should be due to the onset of film boiling rather than the wicking ability of the sample.

The heater is made of either Inconel X for the nickel samples, or stainless steel for the stainless samples. This material selection reduces differential expansion between the heater and sample which could break the sample-heater bond. The top side of the heater is plasma arc-sprayed with a 0.002-inch coating of aluminum oxide. A thin layer of epoxy bonds the coated surface to the sample backup plate. A 1/2-inch Transite block is placed under the heater and is held in place by two 1/8-inch wide layers of epoxy along the side edges. Figure 67, which is a photograph of a completed sample, shows these edges of epoxy, and Figure 65 shows a schematic of sample-heater construction. The advantages of this type of sample-heater construction are the following:

- a. The aluminum oxide coating provides the electrical resistance necessary to prevent current leakage across the sample, while the thermal conductivity ( $10 \text{ Btu/hr ft}^2$ ) remains quite high for an electrical insulator. Hence, the temperature drop across the aluminum oxide is negligible for the heat fluxes of interest ( $10,000 \text{ Btu/hr ft}^2$  to  $100,000 \text{ Btu/hr ft}^2$ ).
- b. The epoxy bond between the heater and sample maintains good thermal contact.
- c. The epoxy edge prevents boiling heat transfer losses from the edges of the sample and heater. Edge boiling could also inhibit the flow of liquid to the wick surface.
- d. The Transite prevents boiling from the bottom of the heater. The Transite is held in place by the epoxy on the edges of the assembly rather than by epoxy on the underside of the heater, since the bottom surface of the heater is at the highest temperature of any surface in the boiling apparatus. Hence, the epoxy could possibly decompose if used on this surface.

### 3. Changes Since Last Report

The following additions to the rig have occurred since the last report:

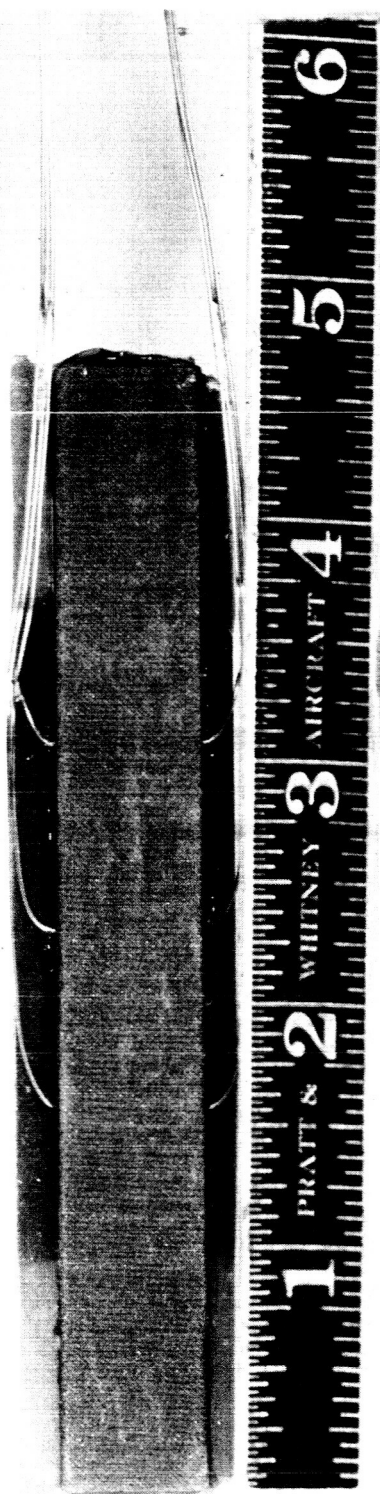


Figure 67 Boiling Test Sample M9. 150-Mesh Sintered Nickel Screen

- a. A fixture was built for tilting the primary tank to test the effect of wick orientation with respect to gravity on heat transfer coefficients. The fixture consists of two steel plates, hinged together at one end, and connected by supporting rods on the other end. The tank, which is bolted to one of the plates, can then be tilted up to 90 degrees by varying the length of the rods. Figure 68 shows the tank operating at a 45-degree angle.
- b. A heater was installed between the secondary and primary tanks in order to heat the incoming water to the primary tank.

#### 4. Instrumentation

The data obtained from the boiling tests is used to plot  $q$ , the heat flux through the wicking sample, as a function of  $\Delta T_{\text{sat}}$ , the temperature difference between the liquid-wick-solid interface and saturated vapor. In order to accomplish this, six chromel-alumel thermocouples are located in the underside of the sample backup plate, two are installed in the vapor above the sample to measure the temperature of the saturated vapor, and two are immersed in the liquid. Also, two sets of thermocouples are located at different planes in the Transite block on top of the guard heater to enable the control of this heater. For each test point, the guard heater is adjusted until the two sets of thermocouples read the same, thus minimizing heat losses from the underside of the heater through the Textolite platform. The heat flux is computed from the measured voltage drop and current across the sample, and the known area of the sample.

Figure 67 shows six thermocouples installed in a 150-mesh sintered screen sample. The thermocouple wires are enclosed in sheaths of 0.020 inch inside diameter and are welded in 0.020-inch grooves on the underside of the sample backup plate. The actual thermocouple wires (0.001 inch in diameter) are then welded to the bottom of the grooves, and the grooves are filled with epoxy. Hence, the temperature being measured is at a location of 0.001 or 0.005 inch from the liquid-wick-solid interface, since the sample backup plates are either 0.021 or 0.025 inch thick. The liquid-wick-solid interface temperature can be calculated using the equation

$$T_{\text{lws}} = T_m - \frac{Q\Delta x}{A k_B} \quad (25)$$

where  $T_m$  = measured temperature of backup plate

$Q$  = heat input to sample

$A$  = heater area normal to heat flow

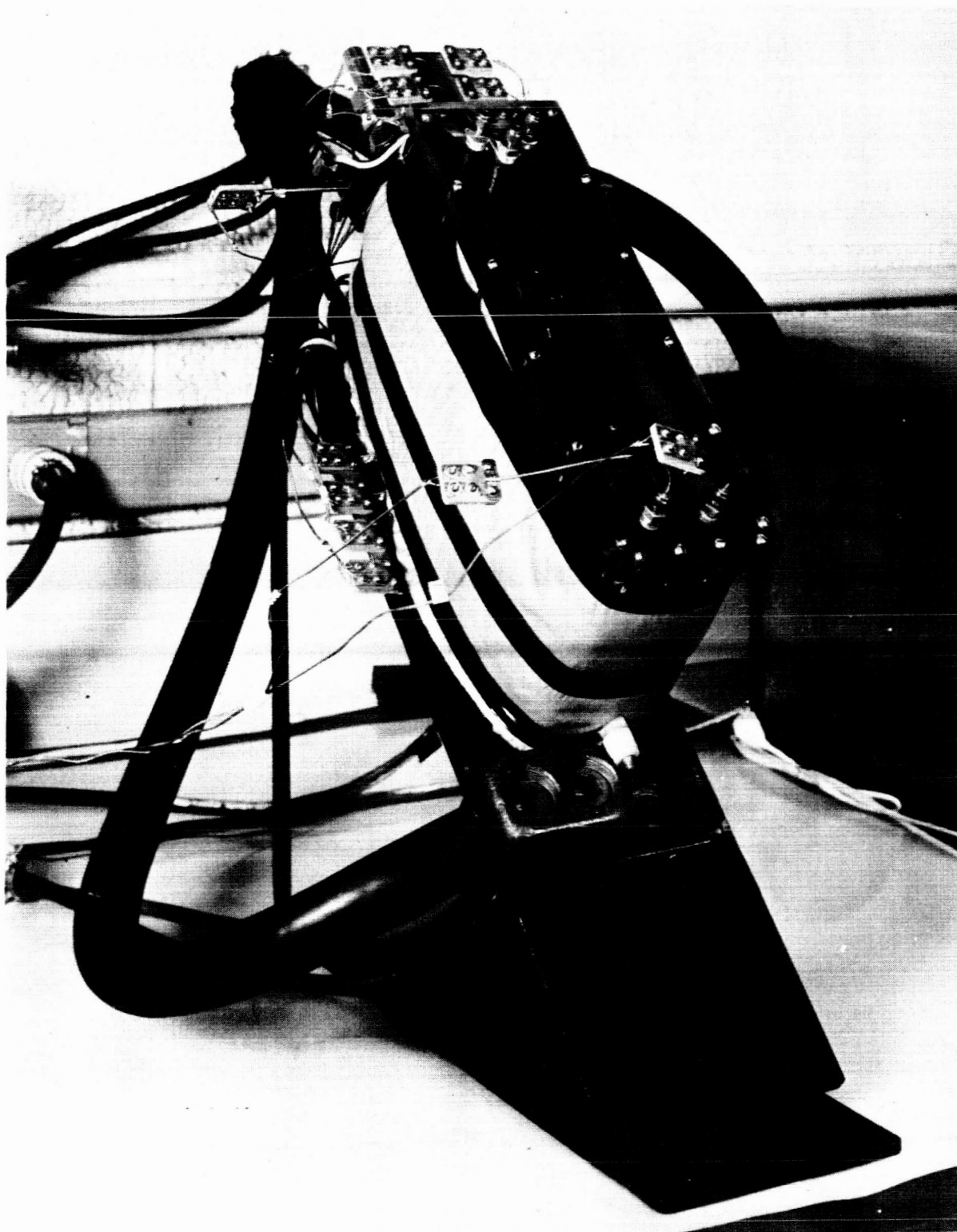


Figure 68 Boiling Apparatus during 45-Degree Angle Test

$\Delta x$  = backup plate thickness from measured temperatures to the liquid-wick solid interface (0.001 or 0.005 inch depending upon the sample)

$k_B$  = thermal conductivity of the backup plate

The thermocouple outside sheath dimension and groove size were changed from those stated in the last report period for the following reasons:

- a. The change in groove size from 0.015 to 0.020 inch means that the second term in Equation (25) becomes less significant, and hence  $T_m$  is closer to  $T_{lws}$ . This results in a lower error in the calculation of  $T_{lws}$ .
- b. The 0.010-inch outside sheath in the previous design required a bracing sheath around it for support. This required much time for installation, and resulted in a stiff, brittle structure. The more pliable 0.020-inch sheath has adequate strength and is less prone to accidents which result in the loss of a thermocouple.

Appendix A includes a summary of the instrumentation used and its location.

#### 5. Power Supplies

Power for the boiling rig is supplied by a 12 KVA rectifier with a three-phase 480-volt input and a controllable DC output of up to 750 amperes at 12 volts, or 1500 amperes at 6 volts. The guard heater power is controlled by a 115-volt input powerstat.

#### 6. Test Procedure

Appendix A contains the boiling test procedure that was presented in the second quarterly report, with additional information on the instrumentation used.

### C. Test Results

To enable the results obtained in the present program to be more easily interpreted, a brief review of general pool-boiling phenomena is included in the following paragraphs.

#### 1. Boiling Phenomena

The relationship between heat flux and the difference between the surface and fluid temperatures for water boiling at atmospheric pressure on a submerged electrically heated Chromel C wire is shown in Figure 69. The

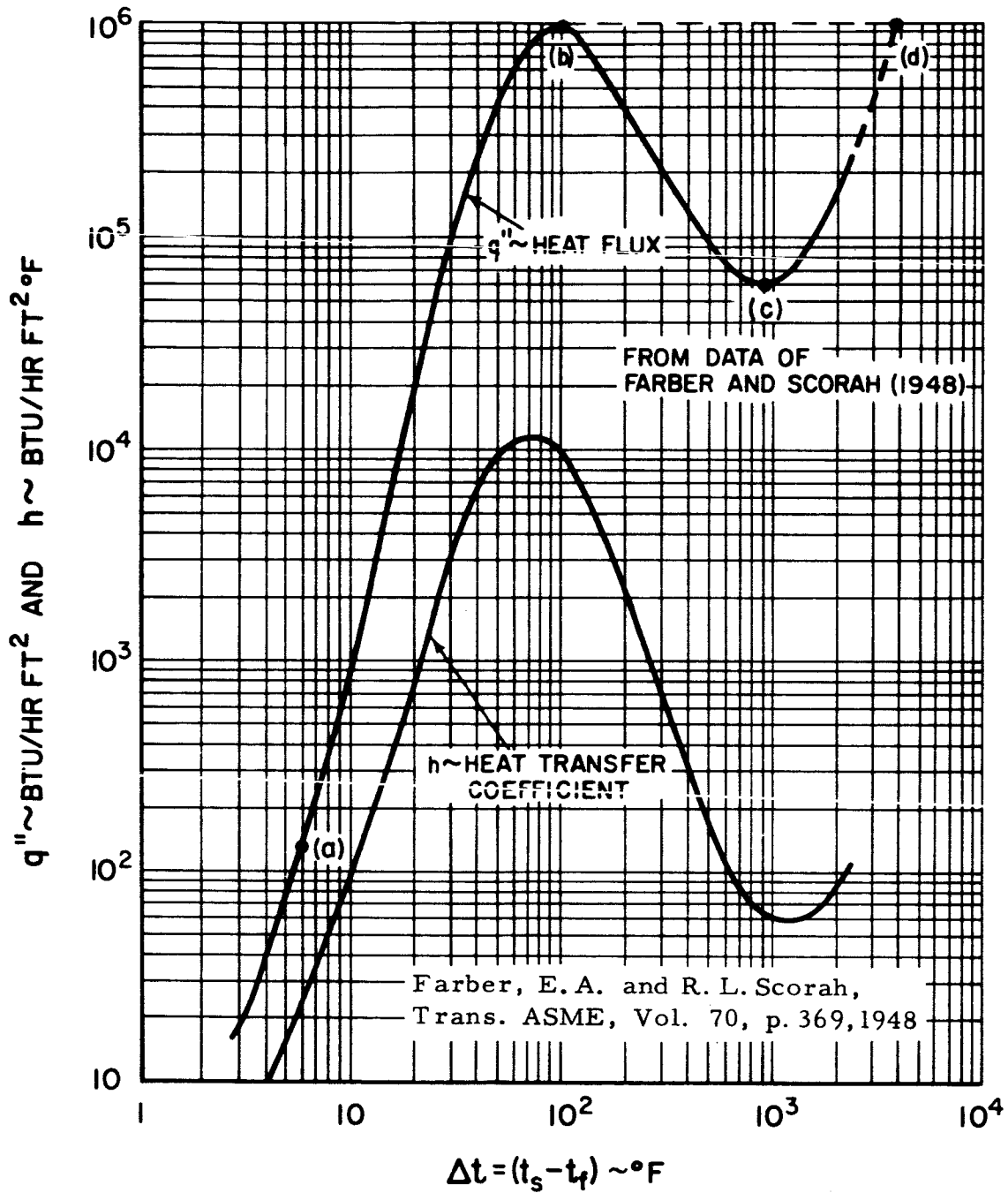


Figure 69 Heat Flux and Heat Transfer Coefficient vs  $\Delta T$  for Water at 14.7 psia Boiling on a Horizontal Chromel C Wire 0.040 Inch in Diameter



variation in heat transfer coefficient with the temperature difference is also shown in this figure. The heat flux curve of Figure 69 can be divided into four regions. At point (a) significant boiling begins. Small bubbles form at favored nucleation sites on the wire surface, and move by buoyant forces through the liquid to the upper surface of the liquid. This activity greatly increases the heat transfer coefficient. As the heat flux is further increased from (a), more and more nucleation sites become active, causing a rapid increase in the heat transfer coefficient with increasing heat flux. However, as more nucleation sites become active, the surface also tends to become blanketed with vapor. This occurrence impedes heat transfer. At point (b) the wire surface is completely blanketed by vapor, causing an increase in  $\Delta T$  along the dotted line to point (d) for a heating device of constant heat flux. The region bcd is not usually attained from a constant heat flux device such as an electrically heated surface, but would occur with a constant  $\Delta T$  device such as a surface heated by condensing vapor. Since the heater surface temperature for point (d) is usually beyond the melting point of metals, point (b) is called the burnout heat flux. It represents the maximum heat flux obtainable by nucleate boiling heat transfer and is the point at which transition to film boiling begins.

The general boiling regimes experienced in horizontal wire tests have also been shown to occur in tests with flat plates and other geometries. However, experimental values for burnout heat flux and heat transfer coefficients vary widely and are dependent upon such factors as the surface conditions, dissolved gases, and pressure level.

## 2. Test Results

Boiling tests in water at atmospheric pressure were run on a flat-plate sample, a 150-mesh sintered screen sample (M9), a 50-mesh sintered screen sample (M7) and a sintered nickel powder sample (M2). The results of the tests are presented below in terms of graphs of  $q$  vs  $\Delta T_{\text{sat}}$ . The method used for computing  $\Delta T_{\text{sat}}$  from measured temperatures is discussed in Section VI. B. 4. above. An approximate method was used to calculate the heat losses in order to obtain  $q$  from the power input to the heater. Hence, the data presented will be refined when the rig is calibrated for heat losses in the near future. However this calibration will not change most of the heat flux values given by more than 10 to 15 per cent, and will probably not affect any of the conclusions reached.

It should be noted that the water in the primary tank was below the saturated condition for most heat fluxes below 20,000 Btu/hr ft<sup>2</sup>. Hence,  $\Delta T_{\text{sat}}$  is negative for the low heat fluxes. Since the same degree of subcooling, for a given heat flux, was evident in almost all of the tests, this problem is not considered serious for a comparative study of the boiling characteristics of wicking materials.

Thermocouple No. 6 (see Figure A1 in Appendix A) was used as a representative value in the calculation of  $\Delta T_{\text{sat}}$  for the curves. The reason for choosing this thermocouple is that in all tests it read neither the highest nor the lowest value of temperature across the sample. A careful check was made to insure that none of the conclusions drawn from the curves would be altered if any of the other thermocouples had been used for the plots.

#### Flat Plate

Boiling heat transfer data was obtained for a stainless steel plate oriented horizontally and vertically. Figure 70 is a photograph of the sample tested. The dark edges along the sample are formed by the epoxy. The temperature distribution along the plate was very uniform when horizontal, seldom varying by more than a degree at the liquid-solid interface of the sample. For the vertical orientation, however, the temperature varied by as much as 17°F, with the mean temperature approximately the same as the horizontal plate temperatures. The temperature distribution across the sample face in the vertical test exhibited no explicable trends. Hence, it is assumed to have been due to either the random action of bubbles across the sample face, or deterioration of the sample-heater bond.

Figure 71 shows the results of the horizontal test on the flat-plate sample. Also shown in the figure are the results of flat-plate boiling obtained by Jakob and Linke. The difference between the two curves is explained by the difference in surface conditions. As shown in tests by Jakob and Fritz, a rougher surface contains more sites for nucleation, and hence during boiling has a lower  $\Delta T_{\text{sat}}$  for a given heat flux. For the test shown in Figure 71 the flat plate was rolled stainless steel with the surface unaltered, while for the test by Jakob and Linke the plate surface was classified as smooth. Hence, a higher  $\Delta T_{\text{sat}}$  was required for the same heat flux for the flat-plate test. The flat-plate results of the horizontal test (Test No. 9) shown in Figure 71 will be used as a basis for comparison in the discussions of the wick boiling samples that follow.

#### 150-Mesh Sintered Nickel Screen

Tests were run on the 150-mesh sintered nickel screen sample at various degrees of wick saturation and orientation with respect to gravity, as shown in the following table. The degree of saturation is the percentage of the distance

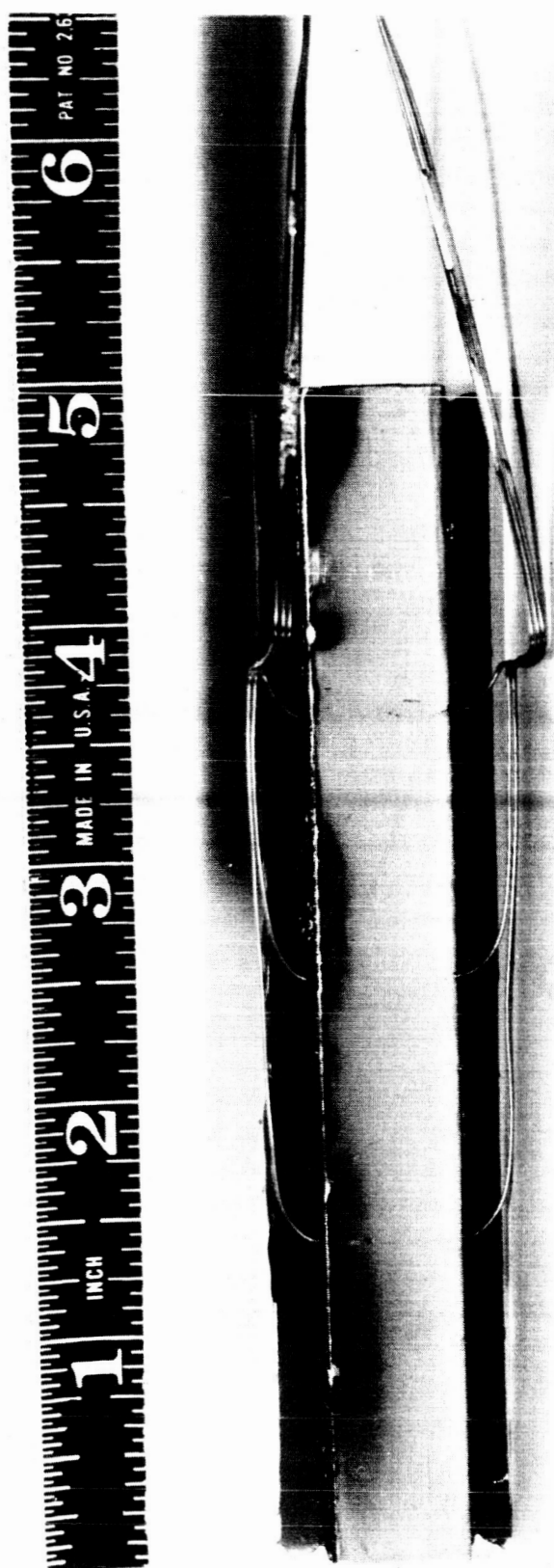


Figure 70 Flat-Plate Boiling Test Sample

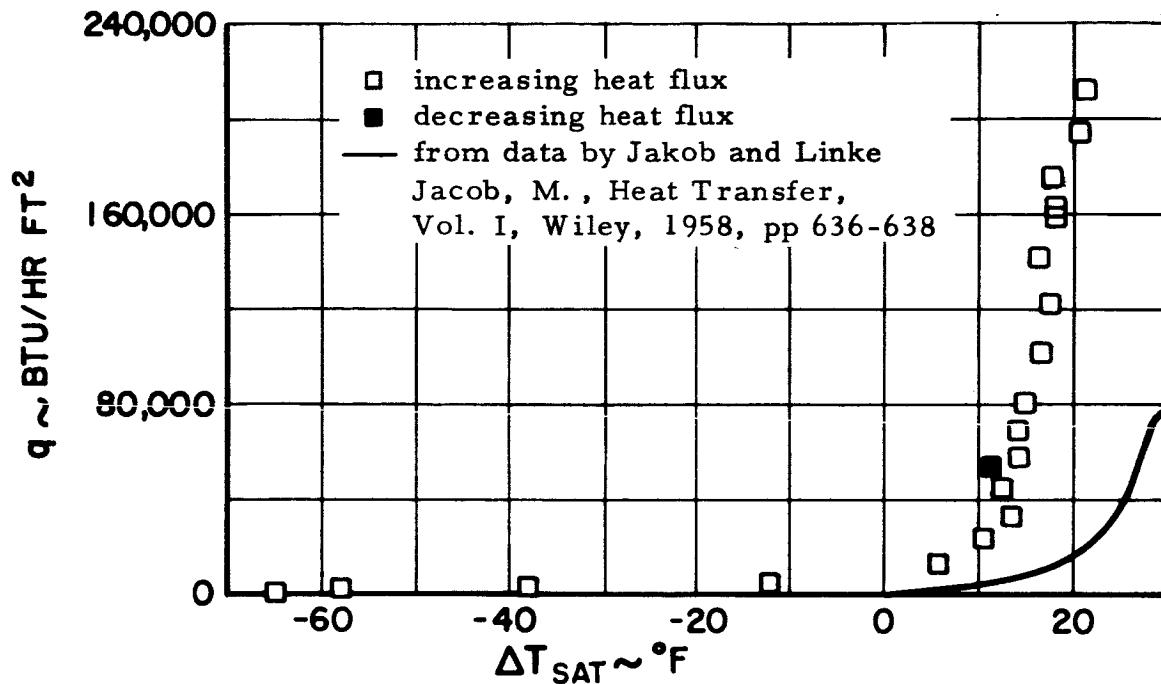


Figure 71 Heat Flux vs  $\Delta T_{sat}$  for Horizontal Flat Plate

across the thickness of the wick at which the free liquid level occurs. This was measured by means of a depth micrometer.

- Test No. 3 - 100 per cent saturation, horizontal
- Test No. 5 - 24-degree angle with horizontal, 5/8 inch of wick end submerged
- Test No. 6 - 45-degree angle with horizontal, 1/4 inch of wick end submerged
- Test No. 7-1 - 90-degree angle with horizontal, 0.4 inch of wick end submerged
- Test No. 7-2 - 90-degree angle, completely submerged
- Test No. 12 - 50 per cent saturation, horizontal
- Test No. 13 - 100 per cent saturation, horizontal
- Test No. 14 - 25 per cent saturation, horizontal

After Test No. 7-2 the sample was removed from the boiling apparatus and was separated from the heater to repair two thermocouples. It was cleaned and rebonded to the heater and the three remaining tests listed below 7-2 were run.

#### Horizontal Tests

A plot of  $q$  vs  $\Delta T_{sat}$  is shown in Figure 72 for the tests in which the wick was in the horizontal position. The following observations and conclusions can be made for these tests:

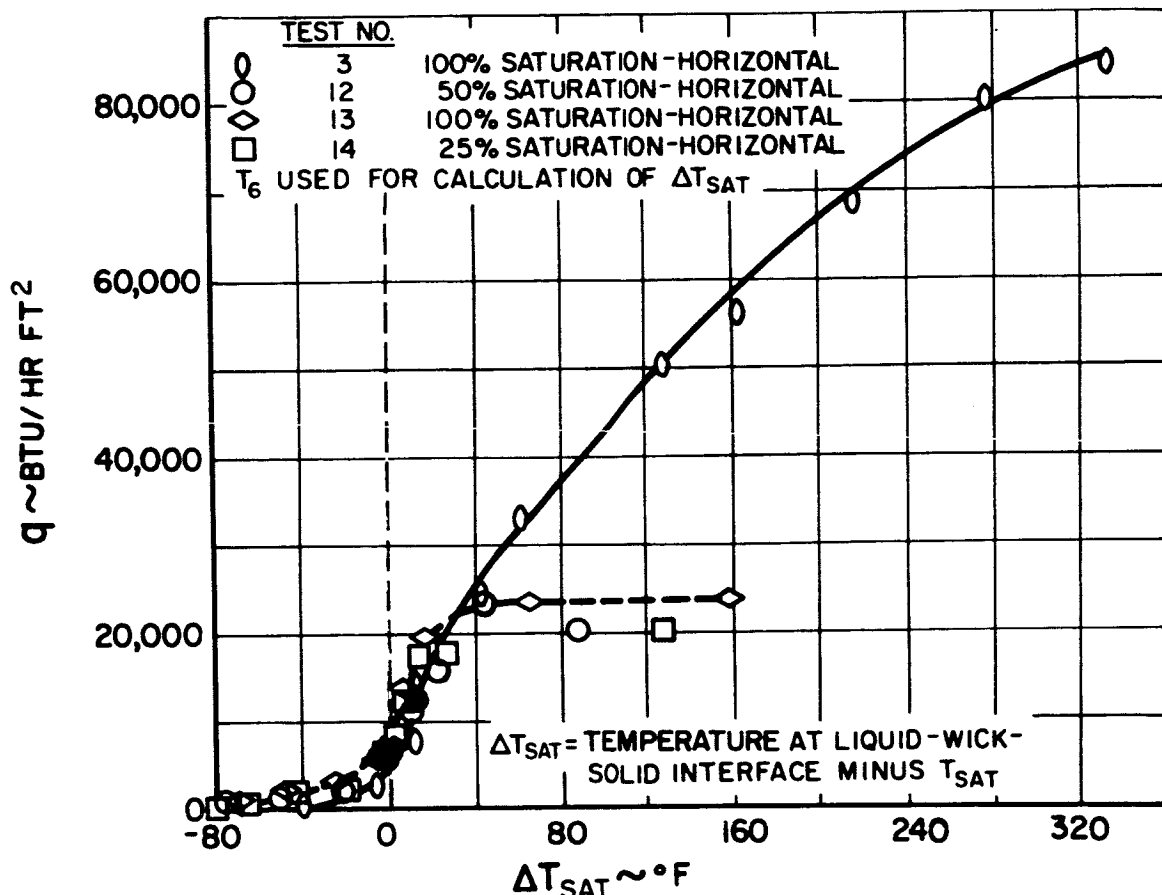


Figure 72 Heat Flux vs  $\Delta T_{sat}$  for 150-Mesh Sintered Nickel Screen

- 1) No vapor bubbles were observed at the top surface of the sample for any of the horizontal tests. Vapor evolution was only visible from the long edges of the sample at the higher heat fluxes.
- 2) Since nucleation occurs at preferred sites, depending upon surface conditions and preferred paths for vapor escape, an uneven temperature distribution was induced across the sample. For example, at a heat flux of 68,500 Btu/hr ft<sup>2</sup> two thermocouples gave temperatures differing by as much as 86°F (383 to 469°F).
- 3) From Figure 72, the two 100 per cent saturation curves follow approximately the same path up to a heat flux of 25,000 Btu/hr ft<sup>2</sup>, but then diverge from each other. This change is considered to be caused by a slight change in the wick properties that occurred during the rebonding process that occurred between Tests Nos. 7-2 and 12. As part of this process, the sample and heater are clamped together in a fixture while the epoxy dries. This clamping pressure on the wick probably closed some of the passages used for vapor escape through the edges. Hence, when a point was reached where the principle mode of heat transfer

was boiling through the edges, the sample required higher values of  $\Delta T_{\text{sat}}$  for a given heat flux in Test No. 13 than in Test No. 3. Visual observation also verified that there was not as much edge boiling in Test No. 13 as in Test No. 3. If boiling had occurred through the top surface rather than the sample edges, the effect of the slight change in wick properties due to clamping would probably have been much smaller.

- 4) As would be expected from the visual observations, the heat fluxes for all of the tests illustrated in Figure 72 are low for a given  $\Delta T_{\text{sat}}$ . For example, at a  $\Delta T_{\text{sat}}$  of 20°F the heat flux for the 150-mesh sample, at all degrees of saturation, is about 20,000 Btu/hr ft<sup>2</sup>, while for the flat plate (Figure 71) it is 200,000 Btu/hr ft<sup>2</sup>. Thus, the heat transfer coefficient for the flat plate is higher than that of the 150-mesh sample by a factor of 10 (10,000 versus 1000 Btu/hr ft<sup>2</sup>°F).
- 5) Comparison of Figures 69 and 72 shows that the shape of the heat flux curve is quite different for a multi-layered screen-covered surface than for an exposed surface. No burnout heat flux was evident for the 150-mesh screen sample. It is speculated that a gradual transition to film boiling occurs because of the difficulty of vapor egress from the region of vapor generation within the wick. From a magnified photograph of the 150-mesh sample shown in Figure 1, it appears that the layers of screen form an almost closed structure, with the wires of one layer filling in the holes in the above layer. Hence, the vapor bubbles formed at the liquid-wick-solid interface are trapped. This action would result in a vapor blanket across the backup plate, as evidenced by interface temperatures rising to over 300°F, well above the saturation temperature. This vapor-blanketing occurs even at lower levels of heat flux since the visual observations indicate vapor escape only through the edges of the sample. A limiting heat flux of about 25,000 Btu/hr ft<sup>2</sup> is evidenced for tests after Test No. 7-2. It is, therefore, the greater amount of boiling through the edges for Test No. 3 that prevents a distinct limiting heat flux point from appearing within the range investigated. A film boiling point should not be defined for the 150-mesh sintered screen sample since boiling from the top surface never occurred.
- 6) Reducing the degree of wick saturation from 100 to 25 per cent does not change the boiling characteristics of the 150-mesh sample significantly. From Figure 72 the curves from the 25 per cent saturation and 50 per cent saturation results follow about the same paths as the curve from Test No. 13 for 100 per cent saturation. Visual observation of Tests

Nos. 12 and 14 showed that no vapor bubbles penetrated the top wick surface.

It is concluded from the above results that the 0.100-inch thick 150-mesh sintered-nickel-screen wick is not feasible for use in a vapor-chamber fin.

#### Tests at Angle to Horizontal With End Submerged

Four tests were run with the top surface of the 150-mesh sintered screen sample at an angle to the horizontal. For three of these tests only a small portion of one end of the sample (about 1/4 inch) was submerged, and hence the water was vaporized as it wicked up the sample. The other test was run with the wick vertical and completely submerged, and is described in the next section.

For the tests with only one end of the specimen submerged, the fluid is vaporized as it wicks up the specimen. This type of test, therefore, should more closely simulate the heating region of a vapor-chamber fin than any of the other boiling tests. Since the liquid must be moved by capillary forces, the liquid front would be located in the smaller pores. This would perhaps result in better boiling heat transfer because the larger pores would then be open and available for vapor egress. The following tests were run in this manner:

Test No. 5	24-degree angle with horizontal
Test No. 6	45-degree angle with horizontal
Test No. 7-1	90-degree angle with horizontal

The results of these tests are shown in Figure 73. The following conclusions can be made with reference to the figure and from visual observation of the tests:

- 1) As the liquid progressed up the wick, the heat transfer process was one of evaporation rather than boiling. Bubbles leaving the wick surface and edges were not observed. Furthermore, the liquid in the wick appeared to be oscillating, with the liquid near the surface at one instant and away from it the next. The period of oscillation was in the order of one second.
- 2) Figure 73 shows plots of  $q$  vs  $\Delta T_{\text{sat}}$  where  $\Delta T_{\text{sat}}$  is computed both

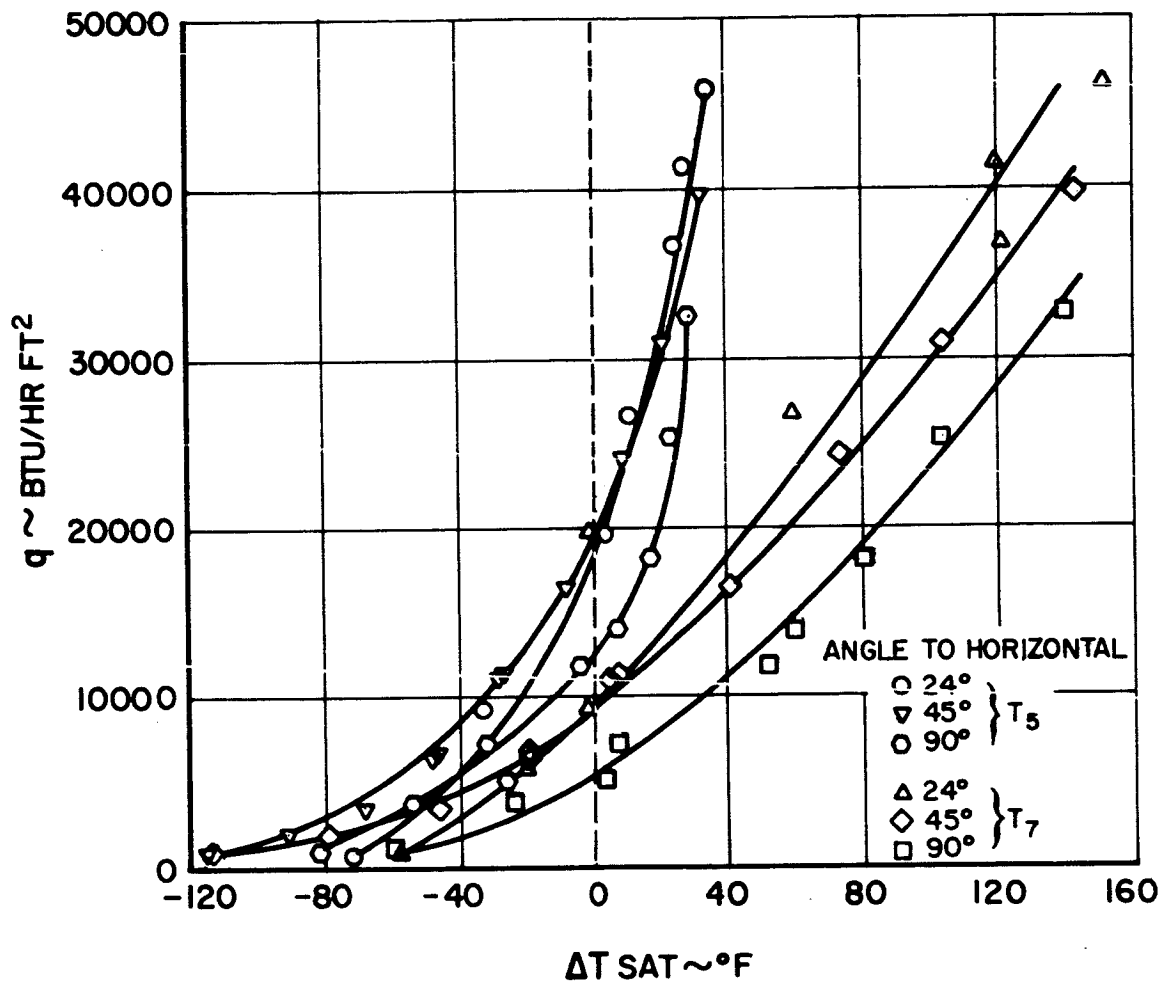


Figure 73 150-Mesh Sintered Nickel Screen. Tests at Angle to Horizontal



from  $T_5$ , the thermocouple closest to the water, (approximately 1/16 inch above the water level, except for Test No. 5 where  $T_5$  was submerged 1/16 inch below the water level) and  $T_7$ , the thermocouple furthest from the water (see Figure A1 in Appendix A). From Figure 73 it is observed that for the same test the heat flux obtained for a given  $\Delta T_{\text{sat}}$  at location  $T_7$  is less than at location  $T_5$ . This was also true in the horizontal test, but not to as high a degree. For example, at a heat flux of 30,000 Btu/hr ft<sup>2</sup> the difference between the readings of Thermocouples Nos. 5 and 7 was 65°F for the horizontal test, as opposed to between 85°F and 130°F for the angle tests. The additional temperature variation in the vertical case is expected since the water has to flow an additional 2 1/4 inches to arrive at location  $T_7$ . Hence, the wick is partially dried at this point, resulting in a higher temperature. In addition, the effect of gravity on reducing the liquid flow is shown by comparing  $T_7$  for the three tests. This temperature can be seen to become progressively higher as the angle is increased and the component of gravity force acting against the flow increased. For the wick end near the water, no substantial difference in temperature for a given heat flux is observed between the 45-degree and 24-degree tests. Hence, there is little flow limitation due to gravity at this point. For the 90-degree test, however, the wick appears to be drying out even at this location.

#### 50-Mesh Sintered Nickel Screen

Two tests were run on the 50-mesh sintered nickel screen sample. These were a horizontal 100 per cent saturation test on a 0.100-inch thick sample (Test No. 4), and a horizontal 100 per cent saturation test on the same sample with all but two layers of screen removed (Test No. 15). During the first test no bubbles were observed leaving the top surface of the sample. Instead, as in the 150-mesh test, vapor evolution occurred at only preferred sites along the edges of the sample. On the other hand, the test with two layers of screen showed boiling across the top surface of the sample at discrete nucleation sites.

The temperature variation across the sample during Test No. 4 was less than 10°F for the lower heat flux, and less than 20°F for the higher heat flux. This small variation as compared to the 150-mesh sample was probably due to more uniform vapor evolution from the edges. For Test No. 15 the maximum temperature variation, except for one point, was 25°F. Nonuniform boiling

probably occurred across the surface because of nonuniformity of the screen layers. Figure 74 shows the results of these tests in comparison to those for the flat plate.

For a given  $\Delta T_{\text{sat}}$  the two-layered screen sample has nearly the same heat flux as the flat plate, while the 0.100-inch thick sample has a considerably smaller heat flux than the flat plate. Furthermore, comparison of the 0.100-inch thick 50-mesh and 150-mesh results shows that the two samples have similar heat transfer characteristics. Also, as in the 150-mesh case, the high temperature at the interface of the wick and backup plate indicates that the interface is blanketed by vapor.

It is concluded that vapor cannot penetrate the top surface of the 0.100-inch thick 50-mesh sample. Hence, this design is not feasible for the boiling section of the vapor-chamber fin. However, the use of two layers of screen in the heat input section of the fin would result in excellent boiling characteristics. The limitation in this case would probably be the pumping capabilities of the wick. Similar conclusions could be drawn for the 150-mesh sample.

#### Sintered Nickel Powder Sample

A horizontal test on a sintered nickel powder sample (M2) was run at 100 per cent saturation of the wick. During the test, vapor evolution sites were observed across the surface of the wick, so that this construction and porosity allowed for some degree of vapor escape from the upper surface. The temperature variation across the face of the wick was usually less than ten degrees. Uniform boiling was observed, although the nucleation sites were scattered across the surface. Figure 75 shows a plot of  $q$  vs  $\Delta T_{\text{sat}}$  for this test, compared to the flat plate results. The sintered-powder sample can be seen to have a comparable heat flux for a given  $\Delta T_{\text{sat}}$  to the flat plate up to a heat flux of 50,000 Btu/hr ft<sup>2</sup>. After this point, the performance of Sample M-2 is inferior to that of the flat-plate sample. Because of the construction of the sintered-powder sample, it is probable that the wick contains a great number of sites for nucleation. This construction allows for vapor escape at lower heat fluxes, so that high performance results. At heat fluxes greater than 50,000 Btu/hr ft<sup>2</sup>, however, vapor entrapment becomes dominant, resulting in a degradation of performance. A limiting heat flux is reached for this sample at about 120,000 Btu/hr ft<sup>2</sup>. Figure 76 shows the results of the tests on Sample M-2 on a semi-log coordinate system.

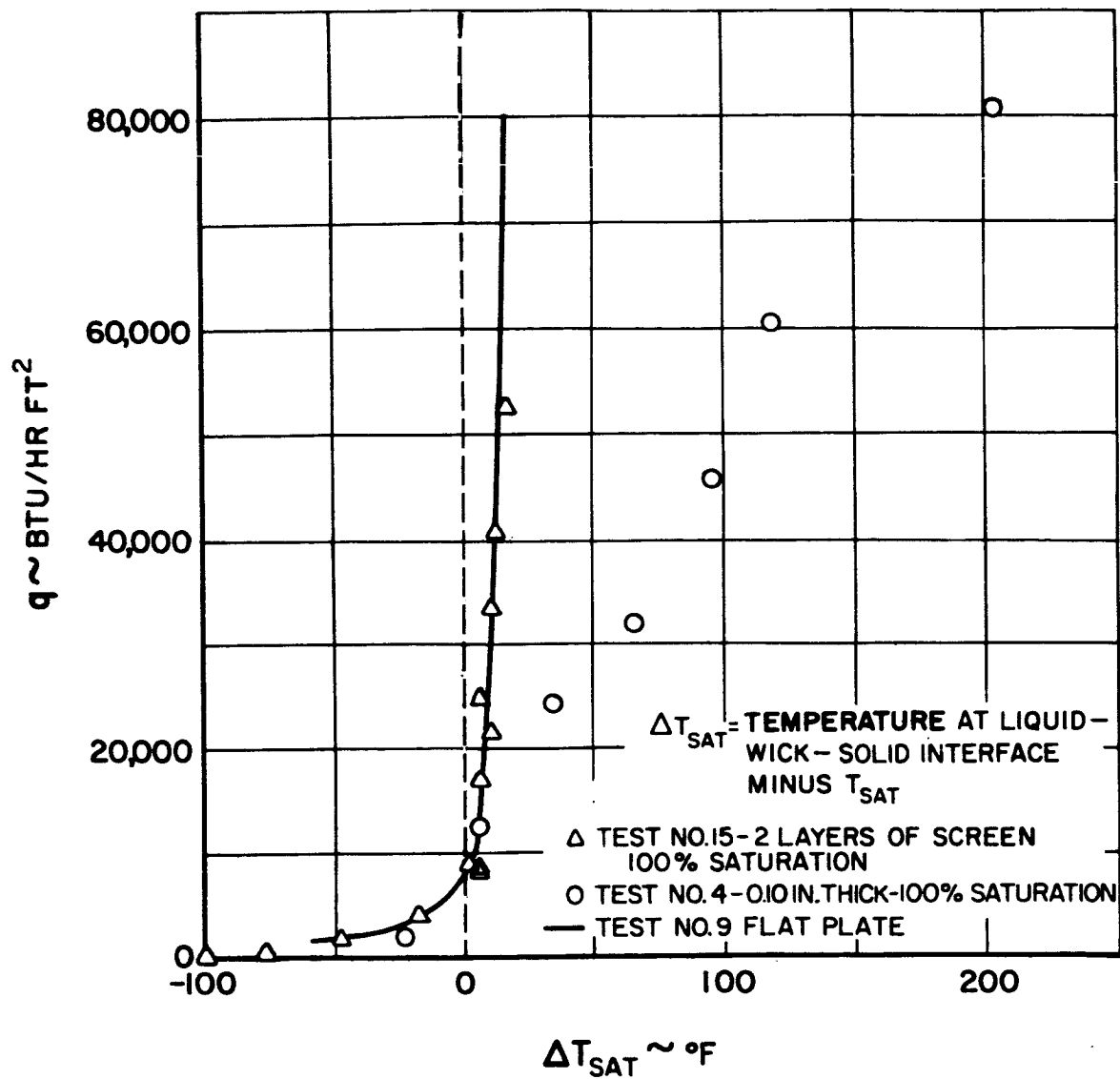


Figure 74 Heat Flux vs  $\Delta T_{\text{sat}}$  for 50-Mesh Sintered Nickel Screen Sample M7

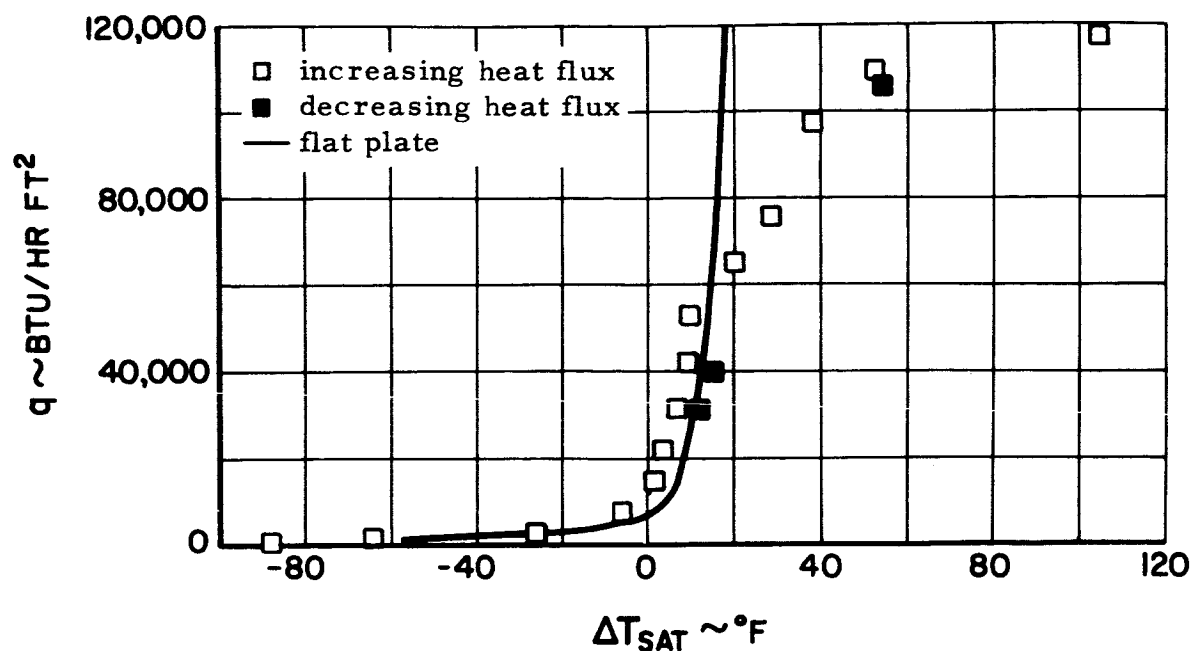


Figure 75 Heat Flux vs  $\Delta T_{\text{sat}}$  for Sintered Nickel Powder Wick Sample M2

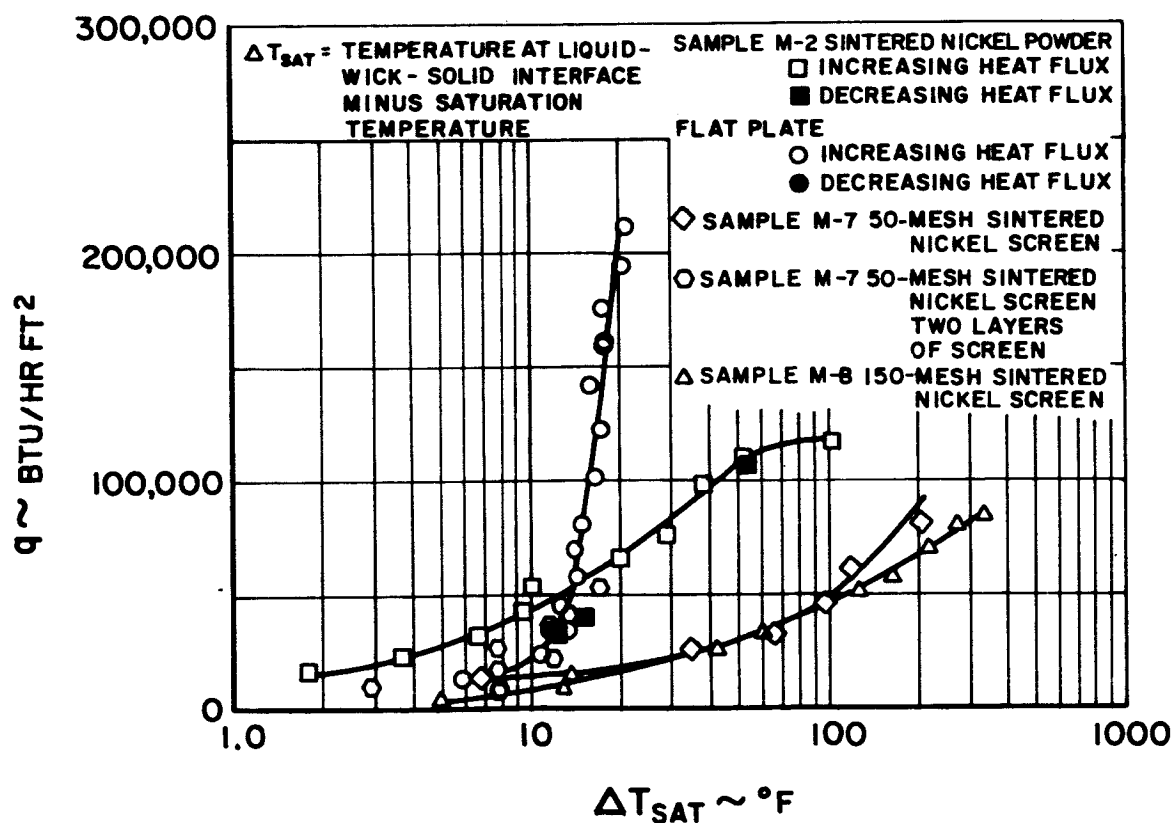


Figure 76 Comparison of Heat Flux vs  $\Delta T_{\text{sat}}$

In conclusion, Sample M2 exhibited heat transfer coefficients ( $q/\Delta T_{\text{sat}}$ ) comparable to a flat-plate sample up to a heat flux of 50,000 Btu/hr ft<sup>2</sup>; a degradation in performance occurred after this point. Since the heat flux range of interest in a vapor-chamber fin is from 10,000 to 30,000 Btu/hr ft<sup>2</sup>, this type of wick construction is promising.

#### Comparison of Results to Date

Figures 76 and 77 show the  $q$  vs  $\Delta T_{\text{sat}}$  curves obtained with a horizontal orientation and 100 per cent saturation for all of the samples tested so far. Samples M-2 and the two layers of 50-mesh screen are considered to have performed adequately from a boiling standpoint; the 0.100-inch thick 50 and 150-mesh samples did not.

#### D. Summary

The boiling heat transfer characteristics of three of the porous samples (M2, M7, and M9) listed in Section III were measured. All of the heat transfer characteristics were compared with data obtained from a smooth-surfaced, flat-plate sample.

In general it was found that all three of the porous samples had lower heat transfer coefficients than the flat plate. This was attributed to the premature occurrence of film boiling, caused by the entrapment of vapor bubbles in the wick matrix.

The variation of heat flux with  $\Delta T_{\text{sat}}$  for the 150-mesh sintered screen sample (M7) was measured for various angles, and various degrees of saturation in water at atmospheric conditions. The highest heat flux (84,000 Btu/hr ft<sup>2</sup> at  $\Delta T_{\text{sat}} = 332^\circ\text{F}$ ) was measured when the sample was in the horizontal position at 100 per cent saturation. Although vapor bubbles were emitted from the edges of the sample, at no time did boiling occur at the free surface of the sample.

A horizontal test at 100 per cent saturation in water was run on a 50-mesh sample (M9), resulting in a peak heat flux of 80,000 Btu/hr ft<sup>2</sup> at  $\Delta T_{\text{sat}} = 204^\circ\text{F}$ . As in the case of the other screen sample, no boiling occurred at the free surface. However, when all but two layers of screen were removed from the sample, the boiling characteristics of the resulting two-layer screen structure improved (50,000 Btu/hr ft<sup>2</sup> at  $\Delta T_{\text{sat}} = 17^\circ\text{F}$ ) with boiling occurring at the free surface of the sample.

Sintered Nickel Powder Sample M2      50-Mesh Sintered Nickel Screen Sample M7, 2 Layers  
□ increasing heat flux      of Screen      ○ increasing heat flux  
■ decreasing heat flux      ● decreasing heat flux  
Flat Plate      ◇ 50-Mesh Sintered Nickel Screen Sample M7  
○ increasing heat flux      ▲ 150-Mesh Sintered Nickel Screen Sample M8  
● decreasing heat flux

$\Delta T_{sat}$  = Temperature at liquid-wick-solid interface  
          minus saturation temperature

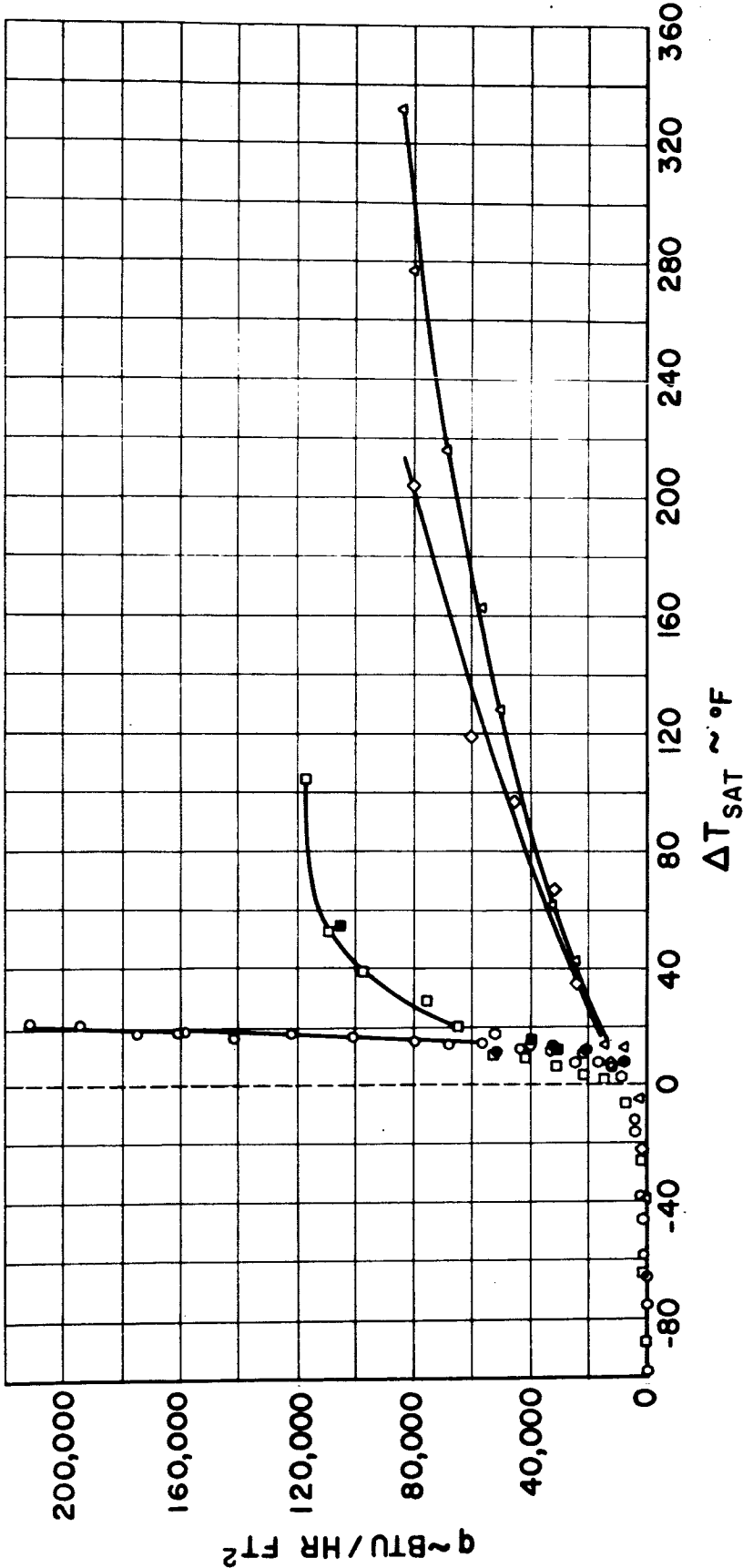


Figure 77 Comparison of Heat Flux vs  $\Delta T_{sat}$  for Wick Samples

The heat transfer characteristics of a sintered powder sample (M2) were measured in the horizontal position at 100 per cent saturation in water. This yielded better heat transfer characteristics than the screen samples (117,000 Btu/hr ft<sup>2</sup> at  $\Delta T_{\text{sat}} = 104^{\circ}\text{F}$ ) due to the fact that boiling occurred at selected sites on the top surface of the sample.

## VII. FIN STUDIES - TASKS 3 AND 4

A. Objective

The objective of the fin studies is to investigate and define the mechanism of heat transport in the vapor-chamber fin. While the studies presented in Sections III, IV, and V provide valuable information about the properties of vapor-chamber fin wicking materials, the purpose of the fin studies is to give direct experimental data on how the fin itself operates. In this way a more complete evaluation can be made of the fin and its applicability to radiators for space powerplants and other uses.

B. Fin Operation

A general description of the operation of the vapor-chamber fin was given in the first quarterly report. For purposes of discussion here the fin will be characterized in this and the following sections by the planar-wick vapor-chamber fin model shown in the sketch in Figure 78.

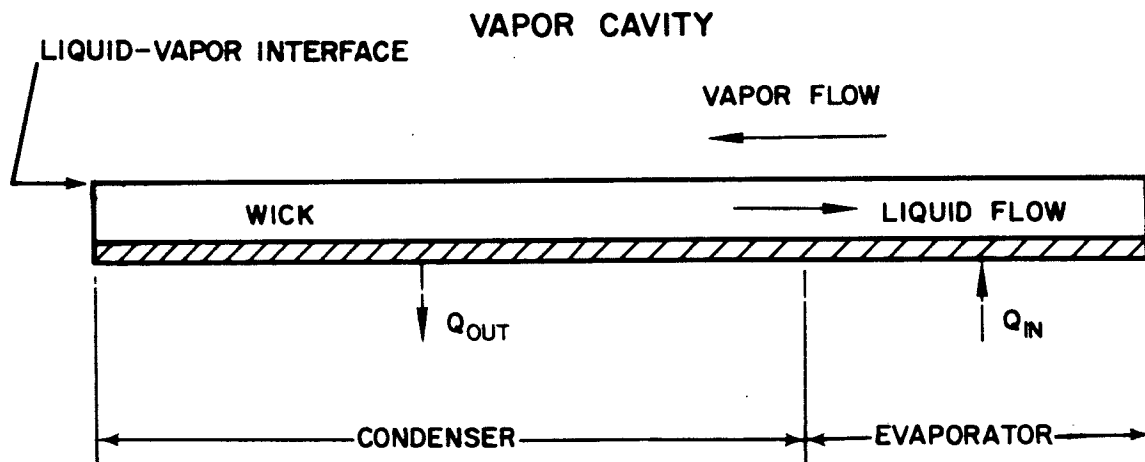


Figure 78 Planar-Wick Vapor-Chamber Fin Model

Basically, the vapor-chamber fin can be broken up into an evaporator, where heat is added to the fin, a condenser where heat is rejected from the fin, a vapor cavity in which the vapor flows from the evaporator to the condenser, and a wick, which acts as a capillary pump bringing condensed vapor from the condenser back to the evaporator.

These transport processes make the vapor-chamber fin an extremely effective heat rejection device, causing it to operate at nearly constant temperature when



there are no noncondensable gases present in the fin cavity<sup>1</sup>. Hereafter it will be assumed that the fin can be characterized by one temperature,  $T_f$ .

When the various transport processes that occur during fin operation are analyzed, it is found that there are probably two phenomena that limit the maximum rate of energy that the fin can transfer. They are:

- 1) The heat flux at which apparent film boiling occurs in the wick of the evaporator, and
- 2) The maximum liquid flow rate that the capillary pump (i. e., the wick) can provide to the evaporator.

When either 1) or 2) occurs during the test of a fin model, the result should be the same: any attempt to increase the net heat input to the fin would result in a large temperature rise in the evaporator, eventually causing a large degradation in fin performance. Thus any program designed to provide an understanding of the operation of the vapor-chamber fin should include an experimental investigation of the occurrence of each of these two limiting phenomena.

### C. General Experimental and Design Considerations

In planning an experimental model and program to evaluate the vapor-chamber fin, several constraints were imposed:

- 1) A temperature range of 200 to 500°F was chosen, so that conventional liquids could be used in any experimental models.
- 2) Water and Freon 113 were chosen as the conventional fluids to be studied because of their difference in properties.
- 3) Two wicking materials were chosen from those listed in Section III.

Another condition can be imposed on the temperature range for any fin test, without resorting to a detailed analysis of the vapor-chamber fin itself. Figure 79 is a plot of the saturated vapor pressure for both water and Freon 113. To prevent the necessity of an excessively heavy structure for any fin model; an upper limit of 150 psia on the internal pressure of the fin was imposed. This corresponds to an upper limit on fin temperature of 358°F for water and 288°F for Freon 113. The vapor pressure curves in Figure 79 show that the vapor pressure of each of the liquids increases prohibitively above these temperatures.

The choice of a heat sink to which any vapor-chamber fin experimental models

<sup>1</sup>Grover, G.M., T.P. Cotter, and G.F. Erickson, Structures of Very High Thermal Conductance, J. Appl. Phys., June 1964, 35, p. 1190

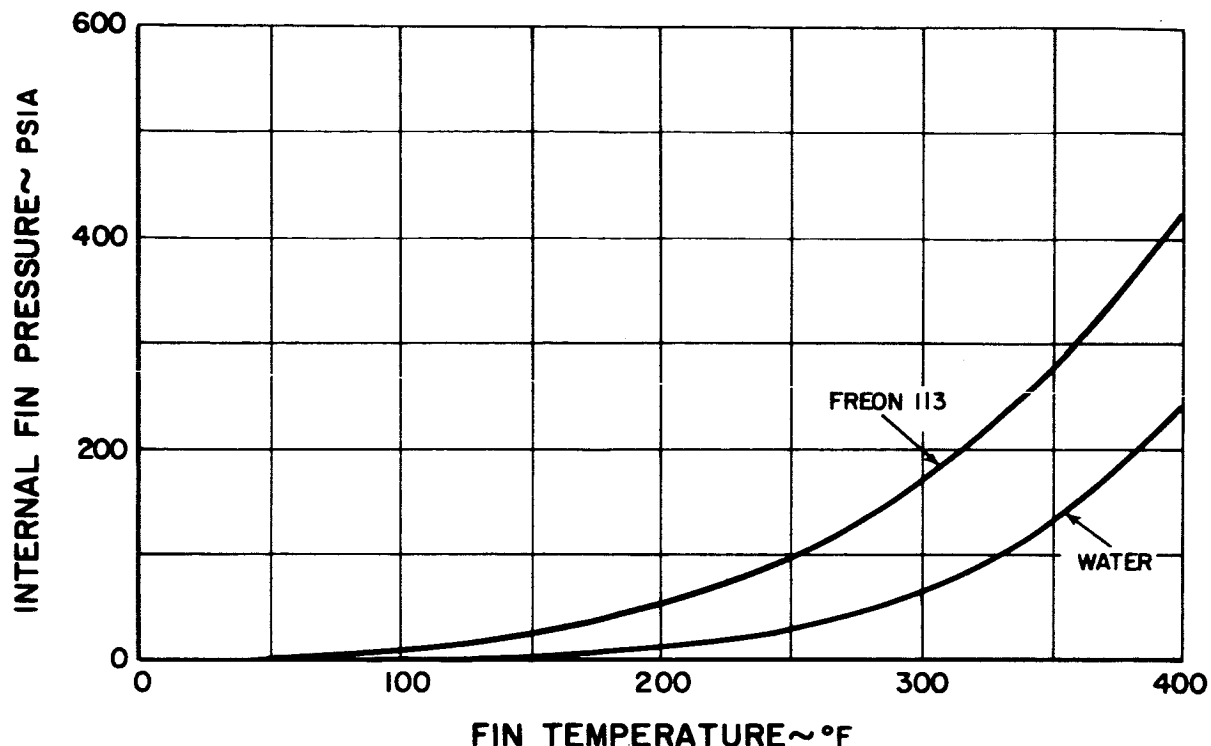


Figure 79 Pressure of Saturated Vapor as Function of Temperature for Water and Freon 113

will reject heat is of particular importance. Because the fin is inherently an efficient device for the transport of heat, care must be taken that the fin heat sink does not itself limit the range of experimental fin studies, and prevent the evaluation of the two limiting phenomena discussed in Section VII. B.

Figure 80 is a plot of the fin condenser heat flux as a function of fin temperature for the case of heat rejection by radiation, with an effective fin-heat sink emissivity of 0.9. The sink temperature shown as a parameter in Figure 80 does not have a great effect on the condenser heat flux in the temperature range shown. It can also be seen that heat rejection by radiation imposes relatively low condenser heat fluxes, in fact, no higher than 690 Btu/hr ft<sup>2</sup> at the upper limit of fin temperature (358°F). Values of heat flux that are this low not only increase experimental uncertainties, but also lead to large fin sizes, as will be shown in Section VII. D. However, heat rejection by forced convection presents a more flexible situation. The fin condenser heat flux as a function of fin temperature for the case of convective cooling is plotted in Figure 81, with the heat transfer coefficient as a parameter. In all cases the convective fluid temperature is taken to be 70°F. The heat transfer coefficient range shown (100-500 Btu/hr ft<sup>2</sup>°F) is one that is relatively easy to obtain by passing water through cooling tubes. In contrast to the case of radiation, a fin model that is convectively cooled could be tested up to a condenser heat flux of as high as 144,000 Btu/hr ft<sup>2</sup> with a heat transfer coefficient of 500 Btu/hr ft<sup>2</sup>.

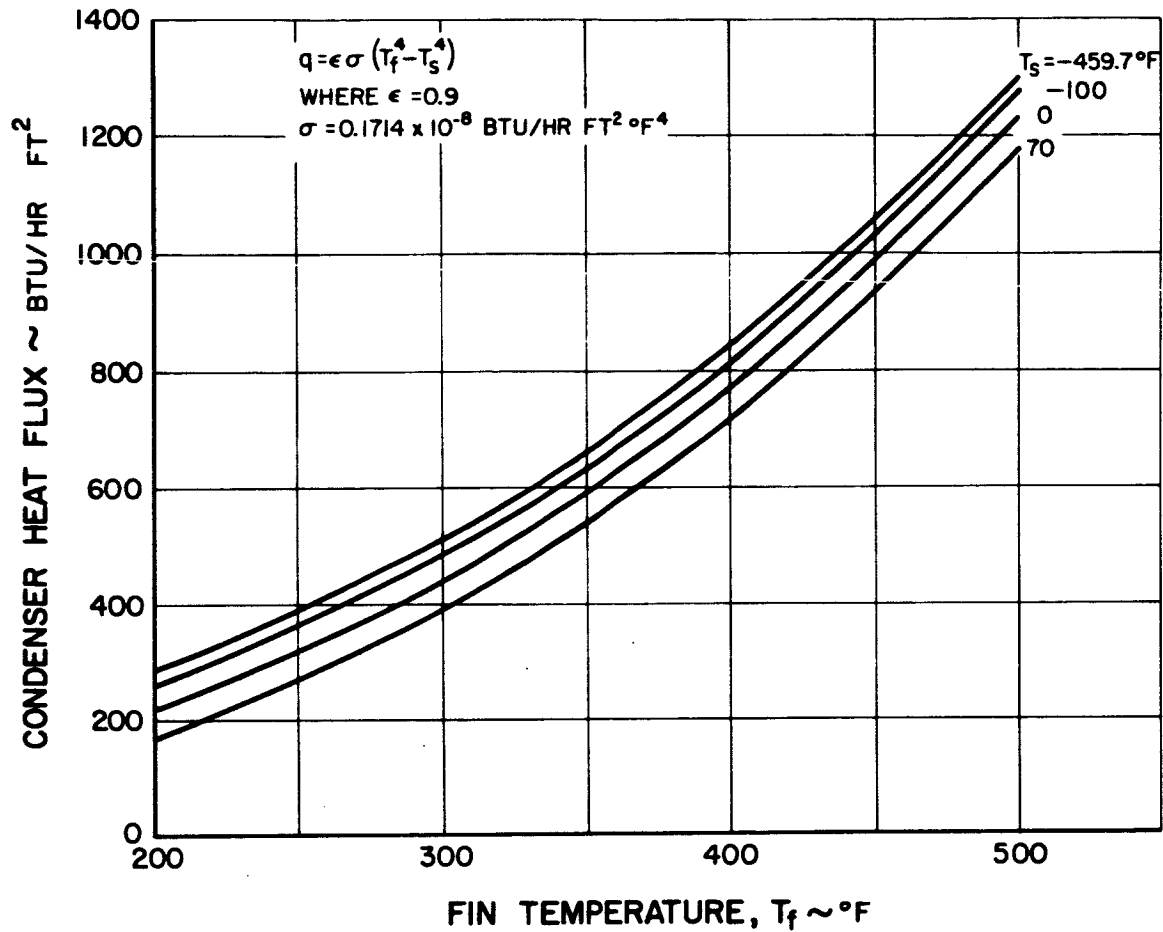


Figure 80 Condenser Heat Flux as Function of Fin Temperature and Sink Temperature for Radiatively-Cooled Fin

Another general consideration that can be dealt with without resorting to any analytical model of the vapor-chamber fin, is the size of the evaporator with respect to the condenser, and the values of heat flux in the evaporator.

The relative size of the condenser and evaporator can be defined as:

$$A^* = \frac{\text{area of condenser}}{\text{area of evaporator}}$$

Since the function of any fin is to effectively increase the primary surface area available for heat transfer, A\* will ordinarily be larger than 1. Because of

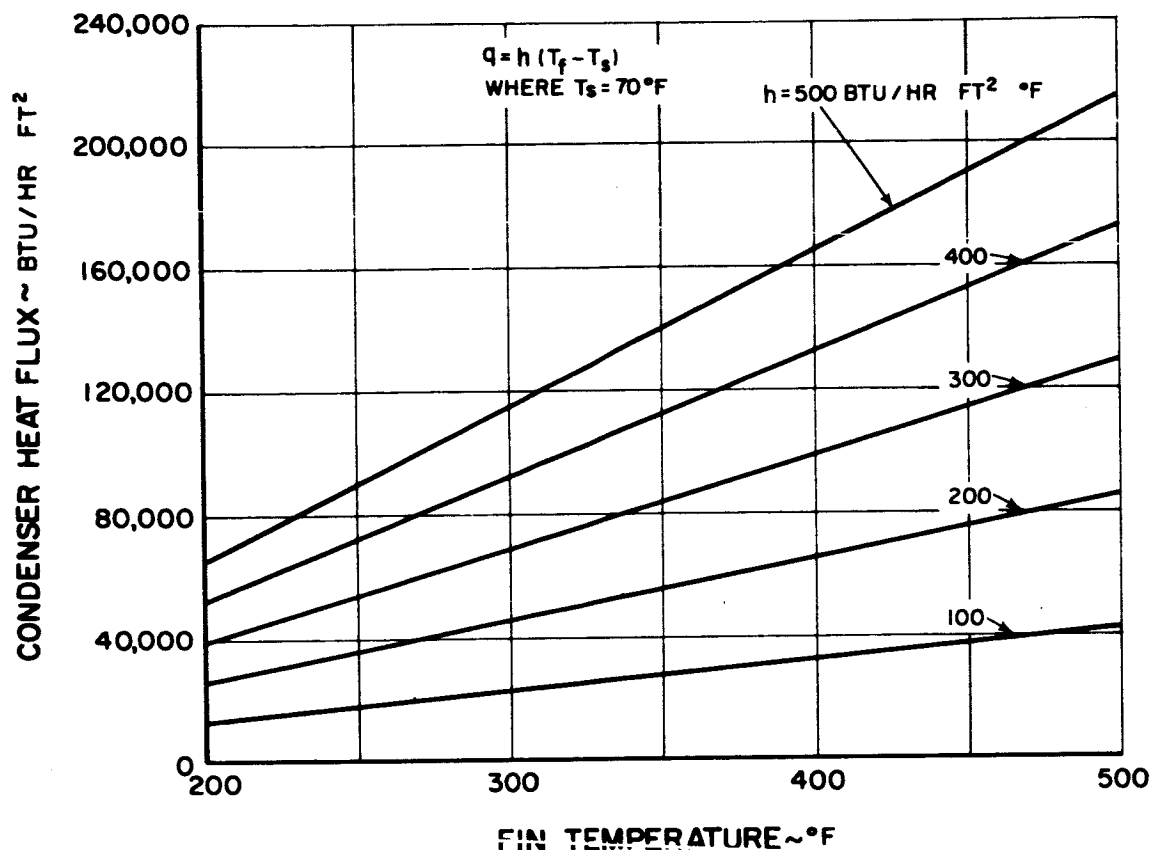


Figure 81 Condenser Heat Flux as Function of Fin Temperature and Heat Transfer Coefficient for Convectively-Cooled Fin

this, the heat flux values will be higher in the evaporator than in the condenser. Also, during any evaluation of a fin model, these heat fluxes should be high enough to insure that the apparent film boiling condition discussed in Section VII. C. can be reached. If electrical heating is used, there is no serious limitation to heating any given experimental fin model. However, the mode of fin cooling can affect the evaporator. For instance, the effect on the evaporator heat flux of cooling a fin using radiation is shown in Figure 82. In this figure, the evaporator heat flux is plotted as a function of fin temperature with  $A^*$  as a parameter. It is assumed that the sink temperature is at  $0^\circ\text{R}$  and that the effective sink-fin emissivity in the condenser is 0.90.

Thus far, the wick boiling studies have shown that the apparent film boiling

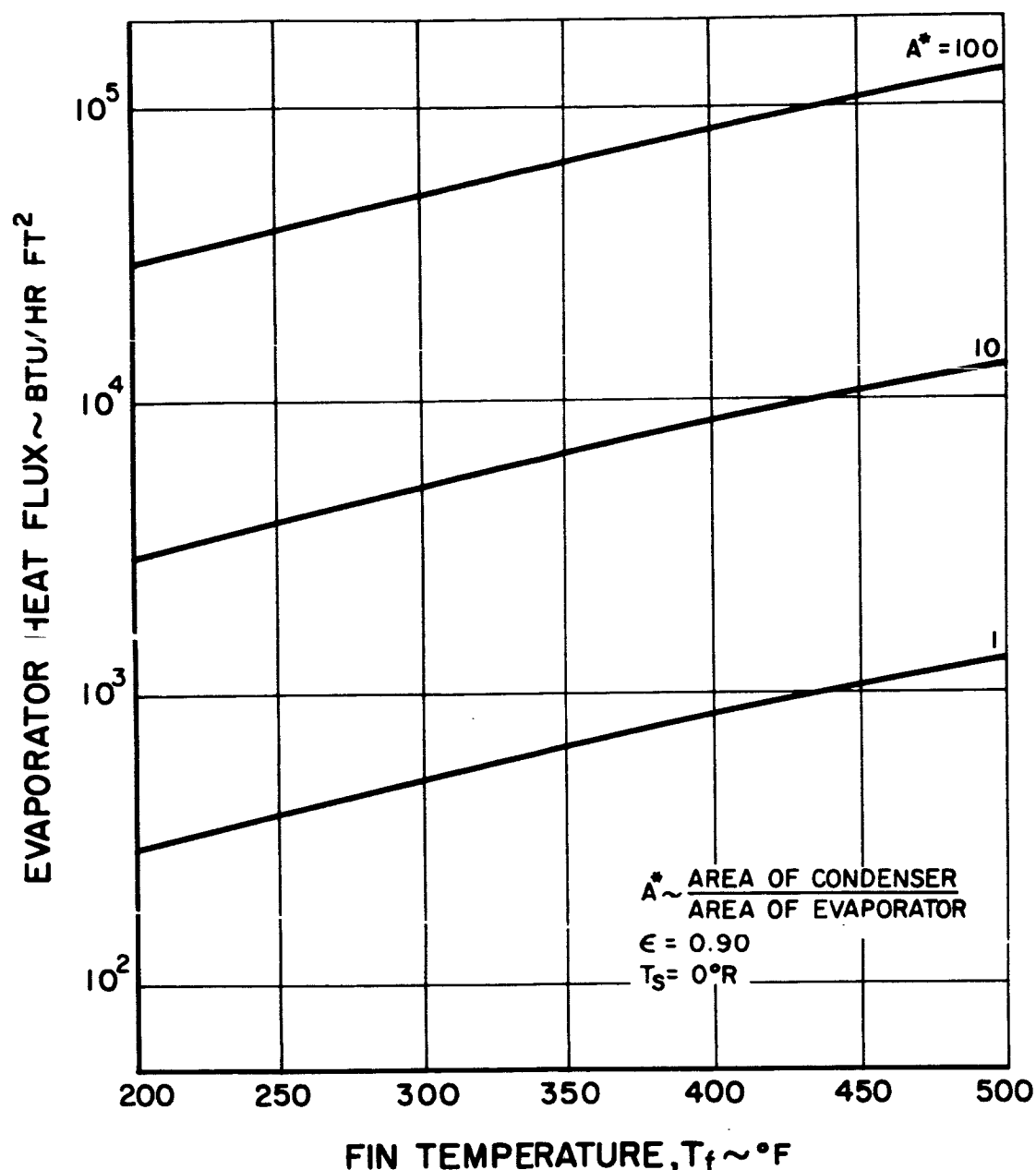


Figure 82 Evaporator Heat Flux as Function of Fin Temperature and Condenser-Evaporator Area Ratio for Radiative Heat Transfer

limitation occurs in the evaporator heat flux range of about  $10^4$  to  $10^5$  Btu/hr ft<sup>2</sup>. Figure 82 shows that this corresponds approximately to  $A^* = 100$  for a vapor-chamber fin that is cooled by radiation. This means that if the condenser section of such a fin were 10 inches long (assuming a planar wick), the evaporator would have to be 0.01 inch long or shorter to achieve apparent film boiling.

Such a short heated length would be difficult to achieve experimentally, due to the effects of conduction along the walls of the fin, which will be relatively thick to withstand internal pressure.

The evaporator characteristics of a convectively-cooled vapor-chamber fin are shown in Figure 83. The evaporator heat flux is plotted as a function of fin temperature. In this case the parameters are  $A^*$  and the heat transfer coefficient at the condenser. Again, it is seen that a fin model that is convectively cooled is more flexible from an experimental point of view. As shown in

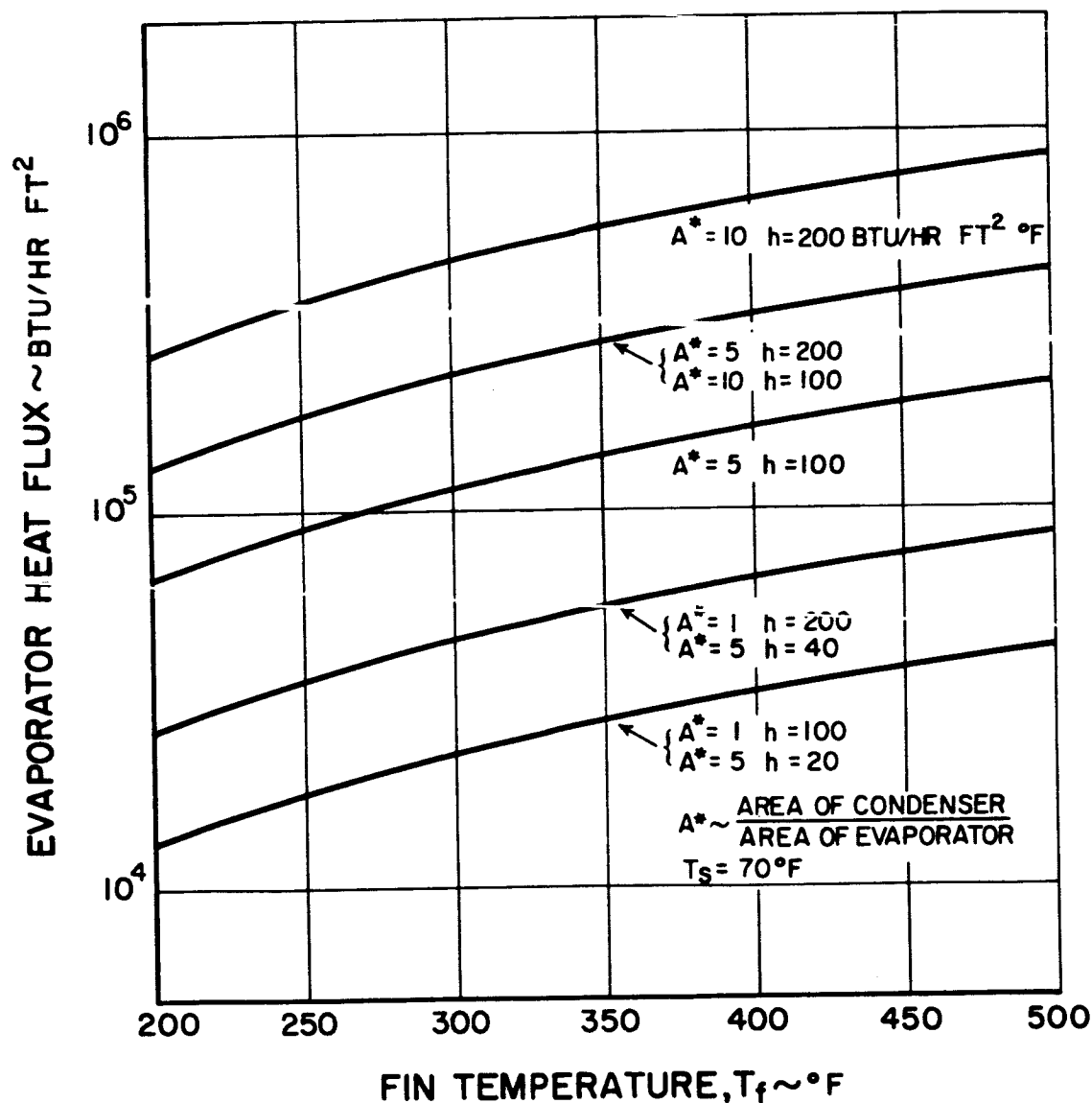


Figure 83 Evaporator Heat Flux as Function of Fin Temperature and Condenser-Evaporator Area Ratio for Convective Heat Transfer

Figure 83, the apparent film boiling heat flux range of  $10^4$  to  $10^5$  Btu/hr ft<sup>2</sup> can easily be achieved with  $A^* = 5$  and a value of the heat transfer coefficient between 20 and 100 Btu/hr ft<sup>2</sup>°F. A fin model with a value of  $A^*$  of 5 to 10 would be relatively easy to treat experimentally.

#### D. Calculations Based on Analytical Model

The discussion presented in Section VII. C. was not based on any knowledge of the internal transport processes in the fin itself. By considering the manner in which heat was rejected from the fin, it was shown what the relative size (i. e., value of  $A^*$ ) of a fin model had to be to achieve one of the two limiting phenomena, that of apparent film boiling in the evaporator section of the fin.

To design a fin model that will permit an evaluation of the second limiting phenomenon, that of capillary pump failure, recourse must be had to some analysis of the internal processes of the fin. Such an analysis was presented in the first quarterly report.

The analysis consisted of the derivation of a simplified model of the vapor-chamber fin, involving a planar wick such as that shown in Figure 78.

With the boundary condition of constant heat rejection along the planar-wick fin, the maximum length that the condenser section could have before the capillary pump failed to provide sufficient liquid to the evaporator, was calculated to be

$$x_m = \left[ \left( \frac{2g \rho_L h_{VL} \sigma}{g_o \mu_L} \right) \left( \frac{\delta}{q} \right) \left( \frac{\rho_L}{\sigma} \right)_{WR} \frac{l_m}{K_1} \right]^{1/2} \quad (26)$$

where

- $g$  = acceleration of gravity
- $g_o$  = Newton's second law proportionality constant
- $\rho_L$  = liquid density
- $h_{VL}$  = liquid latent heat of vaporization
- $\delta$  = liquid - wick thickness (constant)
- $l_m$  = equilibrium height of wick
- $\mu_L$  = liquid viscosity
- $q$  = specified heat flux rejection rate
- $K_1$  = wick friction factor

and where the subscript WR refers to wicking-rise test conditions.

Thus, within the assumptions made in the derivation of Equation (26), any fin with a condenser length greater than  $x_m$  will not supply a sufficient amount of liquid to the evaporator.

Figure 84 is a plot of Equation (26), where  $x_m$  is shown as a function of heat flux in the condenser section. In this plot the liquid-wick thickness is taken as 0.10 inch, the fin temperature is fixed at 350°F, the fin fluid is water, and the wick properties are accounted for by the parameter  $l_m/K_1$ . The latter was shown in the first quarterly report to be a measure of the ability of the fin wicking material to act as a capillary pump, i. e. ,

$$\text{capillary pump output} \propto \frac{l_m}{K_1}$$

The values of  $l_m/K_1$  for the materials listed in Section III. A. fall within the range presented in Figure 84.

In Section VII. C. it was shown that if an experimental fin model was radiation-cooled, the highest heat flux at the condenser would be about 690 Btu/hr ft<sup>2</sup> at a temperature of 358°F. From Figure 84 this heat flux corresponds to a condenser length of about 4 feet for the poorest wick (lowest value of  $l_m/K_1$ ) shown. Referring to Figure 82 it is seen that by assuming an apparent film boiling heat flux of about 80,000 Btu/hr,  $A^* = 100$ . Thus for a planar-wick fin model that is cooled by radiation, the condenser would have to be 48 inches long, while the evaporator could be as small as 0.48 inch, in order to have a fin model that would fail by both capillary pumping and the onset of apparent film boiling in the evaporator.

Clearly this total length of 48.5 inches is prohibitively large to put in a vacuum chamber for radiation cooling, and withstand an internal pressure of 150 psia. Also there is a limit to the size that the wicking materials listed in Section III. A. can be fabricated. In addition, the resulting fin model would have poor performance due to its low  $l_m/K_1$ . Using a wick with a larger value of  $l_m/K_1$  would make the fin model even larger, as evidenced by Equation (26) and Figure 84.

However, a convectively-cooled fin model can be made much smaller and much more flexible in operation. For instance, if a maximum condenser length of 16 inches is chosen for a wick with a value of  $0.242 \times 10^{-8}$  ft<sup>3</sup>, Figure 84 shows that this would correspond to maximum condenser heat flux of about 45,000 Btu/hr ft<sup>2</sup>. At the maximum temperature of 358°F, this corresponds to a convective heat transfer coefficient of about 150 Btu/hr ft<sup>2</sup>, as shown in Figure 81. If a peak heat flux of 80,000 Btu/hr ft<sup>2</sup> in the evaporator is again assumed, it can be seen from Figure 83 that  $A^*$  is about 1.8, neglecting any liquid pressure drop in the evaporator. The occurrence of the latter effect would make the value of  $A^*$  slightly higher than 1.8.



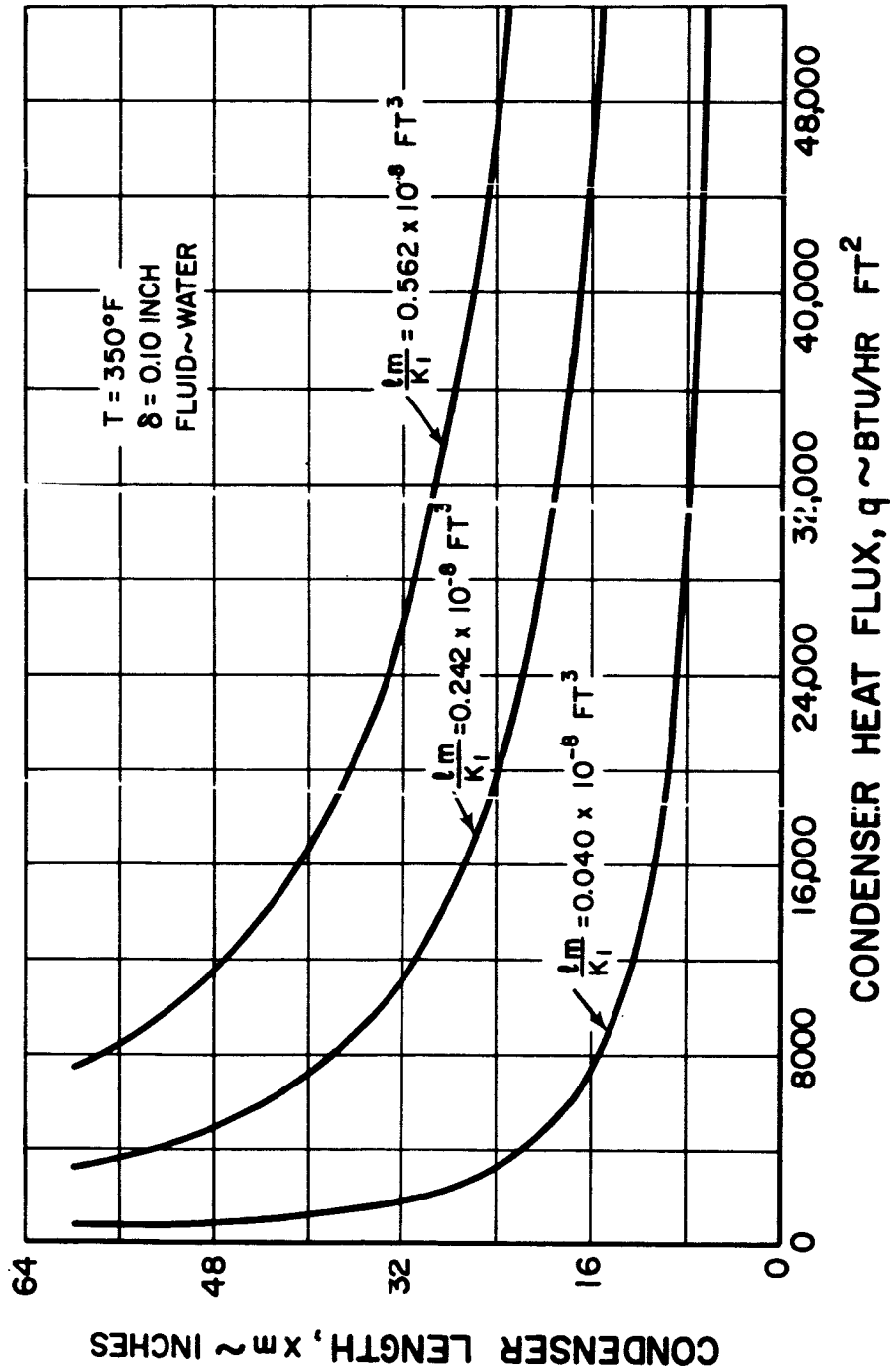


Figure 84 Condenser Length as Function of Condenser Heat Flux and Wick Properties. Computed from Equation (26)

Thus a convectively-cooled planar-wick fin model that would fail both by capillary pumping and the onset of apparent film boiling could be 25 inches long. Using a better wick (higher  $l_m/K_1$ ) would make the fin larger. The resulting fin model would be quite flexible in operation, because of the wide range of condenser heat flux values that could be covered.

#### E. Summary

Two fin fluids, water and Freon 113, were investigated for use in vapor-chamber fin tests. With an upper limit on internal fin pressure set at 150 psia, a maximum fin temperature of 358°F results for water and 288°F for Freon 113.

Because of these relatively low temperature ranges in which an experimental vapor-chamber fin model will be operated, a convectively-cooled model has definite advantages over a fin cooled by radiation. Among these advantages are smaller size and a wider operating range of heat fluxes.

## VIII. FUTURE WORK

### A. Task 1 - Wicking Studies

The experimental work on the wicking rise studies has been completed. The values of the equilibrium height obtained from this data will be interpreted with special reference to such properties as porosity and the pore size distribution function.

The determination of the wick friction factor for selected porous samples utilizing water has been finished. Permeability studies will continue with tests involving Freon 113. In these tests, one sample will be used, possibly H12. The flow rate of Freon 113 through the sample will be varied to insure that flow conditions fall in the Darcy flow regime. The object of this test will be to show that the wick friction factor is independent of the liquid used, and that  $K_1$  depends only on the internal structure of the porous sample.

The data obtained from both the wicking rise studies and the permeability studies will be combined to evaluate each of the wicking materials tested as a capillary pump.

### B. Task 2 - Boiling Studies

Tests on Sample M2 will be completed by running it at various angles and degrees of saturation with water. Boiling tests will also be run on Samples H6, H11, and H13 in the horizontal position. At least one of these samples will be run at various angles and degrees of saturation with water.

At least two of the porous samples listed above will be grooved to evaluate the effect of surface modification on the boiling characteristics of a given sample. These tests will be run in water.

Some boiling studies will be carried out in which Freon 113 is used. When compared to the results of the boiling tests utilizing water, the Freon 113 tests will show the effect of the liquid properties on the curves of heat flux vs  $\Delta T_{\text{sat}}$  for a given sample.

## APPENDIX A

### Test Procedure for Boiling Apparatus

## APPENDIX A

## Test Procedure for Boiling Apparatus

1. Tank Filling

The boiling tests begin by filling the secondary tank with the test fluid to the approximate level desired in the primary tank. The hose clamp in the line connecting the two tanks is then opened, allowing the fluid to flow from the secondary tanks through the heater to the primary tank. The heater is adjusted to fill the primary tank with fluid at a temperature just below saturation. Fine adjustments on the liquid level in the primary tank to change the degree of liquid saturation in the wick sample can be made by altering the adjustable feet on the primary tank or the level of liquid in the secondary tank.

2. Nucleate Boiling Region

Power to the primary heater is controlled by means of a motor-controlled powerstat to the 12 KVA rectifier unit. At low power levels (i. e., not near film boiling), the data points are taken at increasing intervals of 25,000 Btu/hr ft<sup>2</sup> in heat flux. At each point the guard heater is adjusted, by means of a 110V powerstat, until the temperatures of the top two Transite block thermocouples read the same as the bottom two (indicating zero heat loss from the bottom of the heater through the Textolite block). The temperatures are recorded after stabilizing to a point where there is no change over a three-minute period. The heater voltage, the current, and the guard heater current, are also recorded. Adjustments in the liquid level can be made between data points, if necessary. (The decrease in water level due to boil off is 0.018 inch for a 10-minute run at a heat flux of 500,000 Btu/hr ft<sup>2</sup>).

Repeatability of data points is spot-checked throughout the tests. Possible hysteresis effects are checked by approaching some data points from both a higher heat flux level and a lower level.

3. Film-Boiling Region

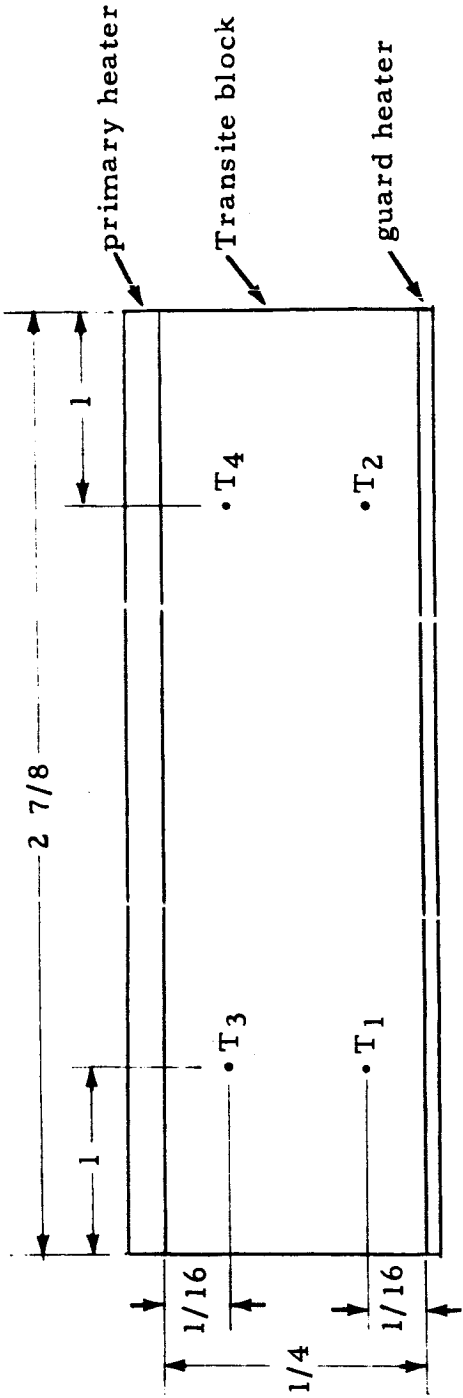
Approach to the film-boiling regime can be detected by visual observation of the bubbles in the nucleate-boiling regime (a relatively large number of nucleation sites with relatively large bubbles). From this point on, the power level interval at which data is recorded is decreased to 5000 Btu/hr ft<sup>2</sup>. At the onset of film boiling, as evidenced by a sharp rise in sample temperatures or the sample turning red in color, the test is terminated by shutting off the electrical power.

4. Instrumentation

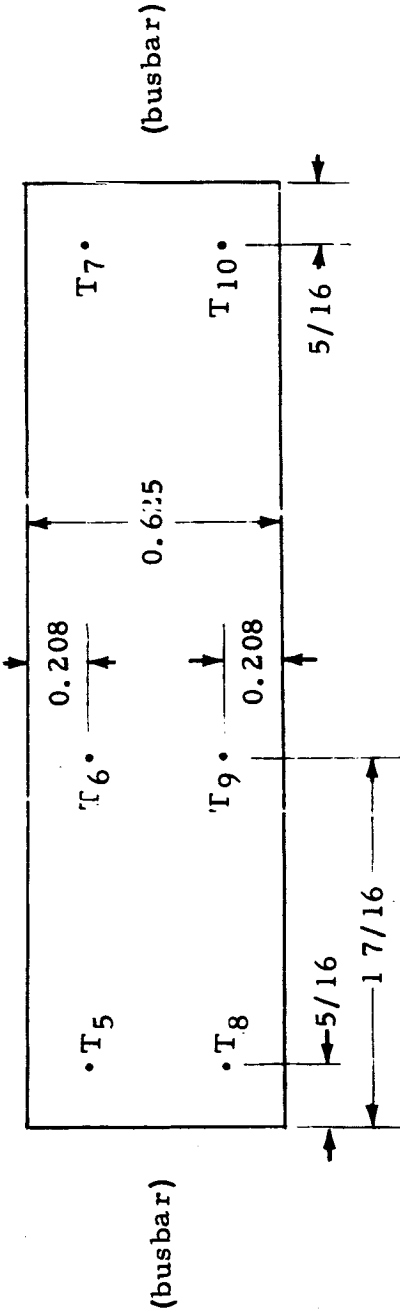
Table A1 presents a summary of the instrumentation used in the boiling rig.

TABLE A1  
Boiling Test Instrumentation

Instrument	Number and Measured Quantity	Location	Range of Meter	Range of Tests	Maximum Error
voltmeter	1, heater voltage, E	across heater	0-7.5v	0.5-4v	0.025v
ammeter	1, heater current, I	across heater	0-1000 amps	75-600 amps	5 amps
ammeter	1, guard heater, Ig current	across guard heater	0-30 amps	2 -10 amps	0.25 amps
C-A Thermocouple	4, guard heater, T <sub>1</sub> , T <sub>2</sub> block temp. T <sub>3</sub> , T <sub>4</sub>	(see Figure A1)	800°F	100-650°F	1.5°F
C-A Thermocouple	6, sample temp. T <sub>5</sub> , T <sub>6</sub> , T <sub>7</sub> , T <sub>8</sub> , T <sub>9</sub> , T <sub>10</sub>	(see Figure A1)	800°F	100-650°F	1.5°F
C-A Thermocouple	2, Primary Inlet T <sub>11</sub> , T <sub>12</sub> Temp.	Inlet tube to primary tank approx. 1 inch from tank wall	800°F	100-200°F	1.5°F
C-A Thermocouple	2, Vapor Temp. T <sub>13</sub> , T <sub>14</sub>	1/2 inch above sample 1/2 inch from either end, half way across in width direction	800°F	200-220°F	1.5°F
C-A Thermocouple	2, Primary Tank T <sub>15</sub> , T <sub>16</sub> Water Temp.	Adjacent to Textolite platforms, 1/2 inch from sample ends, immersed in water 3/4 inch	800°F	100-200°F	1.5°F
C-A Thermocouple	1, Busbar Temp. T <sub>17</sub>	Probe for busbar tem- perature at any location	800°F	100-650°F	1.5°F



a) Guard Heater Thermocouples (elevation view)



b) Sample Thermocouples (top view)

dimensions in inches

Figure A1 Location of Thermocouples for Sample and Guard Heater

## PRATT &amp; WHITNEY AIRCRAFT

Distribution List  
Contract NAS3-7622

National Aeronautics & Space Administration Washington, D. C. 20546		Brookhaven National Laboratory Upton, Long Island, New York	
Attention: Dr. F. Schulman, Code RNP	1	Attention: O. E. Dwyer	1
J. J. Lynch, Code RNP	1	Library	1
Bernard Leafer, Code RNP	1		
Herbert D. Rothen, Code RNP	1		
		Lawrence Radiation Laboratory Livermore, California	
National Aeronautics & Space Administration Lewis Research Center 21000 Brookpark Road Cleveland, Ohio 44135		Attention: Dr. J. Hadley	1
Attention: B. Lubarsky, MS 500-201	1	Los Alamos Scientific Laboratory P. O. Box 1663, Los Alamos, New Mexico 87544	
R. Mather, MS 500-309	1	Attention: Dr. E. Salmi	1
R. Weltmann, MS 500-309	1	Dr. G. Grover	1
J. J. Weber, MS 3-19	1	Library	1
M. U. Gutstein, MS 500-309	3		
H. O. Slone, MS 500-201	1	Oak Ridge National Laboratory P. O. Box X, Oak Ridge, Tennessee 37831	
N. D. Sanders, MS 302-1	1	Attention: Dr. H. W. Hoffman	1
F. Stenger, MS 500-201	1	T. G. Chapman, Bldg. 9201-3 Y-12	1
R. English, MS 500-201	1	Library	1
H. Haller, MS 7-1	1		
U. Von Glahn, MS 6-1	1	U. S. Atomic Energy Commission Technical Information Service Extension P. O. Box 62, Oak Ridge, Tennessee	2
L. Shure, MS 500-309	1		
S. Lieblein, MS 7-1	1	Advanced Research Projects Agency Pentagon, Washington 25, D. C.	
J. E. Dilley, MS 500-309	1	Attention: Library	1
J. Ward, MS 500-201	1		
Reports Control, MS 5-5	1	Aeronautical Systems Division Wright-Patterson AFB, Ohio 45433	
Library, MS 3-7	3	Attention: G. E. Thompson, APIP-1	1
		G. Sherman, API	1
National Aeronautics & Space Administration Ames Research Center Moffett Field, California 94035			
Attention: Library	1	Air Force Aero-Propulsion Laboratory Wright-Patterson AFB, Ohio 45433	
		Attention: A. E. Wallis	1
National Aeronautics & Space Administration Goddard Space Flight Center Greenbelt, Maryland 20771		C. Delaney	1
Attention: Library	1	Library	1
		Air Force Weapons Laboratory Kirtland AFB, New Mexico 87117	
National Aeronautics & Space Administration Langley Research Center Hampton, Virginia 23365		Attention: Lt. D. A. Brooks	1
Attention: Library	1	Library	1
		Battelle Memorial Institute 505 King Avenue, Columbus, Ohio 43201	
National Aeronautics & Space Administration Manned Spacecraft Center Houston, Texas 77001		Attention: D. Dingee	1
Attention: Library	1	Library	1
		The Rand Corporation 1700 Main Street, Santa Monica, California	
National Aeronautics & Space Administration George C. Marshall Space Flight Center Huntsville, Alabama 35812		Attention: B. Pinckel	1
Attention: E. Dungan	1		
Library	1	Institute for Defense Analysis 1666 Connecticut Avenue, N.W. Washington 9, D. C.	
		Attention: R. C. Hamilton	1
National Aeronautics & Space Administration Jet Propulsion Laboratory 2800 Oak Grove Drive Pasadena, California 91103		Library	1
Attention: P. Rouklove	1		
C. Rhodes	1	Massachusetts Institute of Technology Department of Mechanical Engineering Cambridge, Massachusetts 02139	
Library	1	Attention: Dr. P. Griffith	1
		North Carolina State University Department of Chemical Engineering Raleigh, North Carolina	
National Aeronautics & Space Administration Western Operations Office 150 Pico Boulevard Santa Monica, California 90406		Attention: Dr. J. K. Ferrell	1
Attention: J. Keeler	1		
		The Ohio State University Research Foundation 1314 Kinnear Road Columbus, Ohio 43212	
National Aeronautics & Space Administration Scientific and Technical Information Facility P. O. Box 33, College Park, Maryland 20740		Attention: Library	1
Attention: Acquisitions Branch, SQT-34054	2 + repro.		
		City University of New York Department of Chemical Engineering 140th Street and Convent Avenue New York, New York 10031	
U. S. Atomic Energy Commission Germantown, Maryland		Attention: Dr. R. Pfeffer	1
Attention: H. D. Rothen	1		
Col. E. L. Douthett	1	Aerojet-General Corporation P. O. Box 296, Azusa, California	
Cmdr. M. Prosser	1	Attention: Library	1
		Aerojet-General Nucleonics San Ramon, California	
U. S. Atomic Energy Commission Division of Reactor Development & Technology Washington, D. C. 20545		Attention: K. Johnson	1
Attention: R. Scroggins	2	Library	1
U. S. Atomic Energy Commission Division of Space Nuclear Systems Washington, D. C. 20545			
Attention: Dr. L. Topper	1		
G. Leighton	1		



# PRATT & WHITNEY AIRCRAFT

AiResearch Manufacturing Company  
Sky Harbor Airport  
402 South 36th Street, Phoenix, Arizona  
Attention: J. Dannan  
Library

Allison Division  
General Motors Corporation  
Indianapolis 6, Indiana  
Attention: T. L. Rosebrock  
Library

American-Standard  
Advanced Technology Laboratories Division  
369 Whisman Road  
Mountain View, California 94042  
Attention: Library

Atomics International  
P. O. Box 309, Canoga Park, California  
Attention: C. K. Smith  
Library

Douglas Aircraft Corporation  
Missiles and Space Systems Division  
3000 Ocean Park Boulevard  
Santa Monica, California  
Attention: B. Holl  
D. Knapp  
Library

Electro-Optical Systems, Inc.  
300 North Halstead Avenue  
Pasadena, California 91107  
Attention: A. Jensen  
Library

Fairchild Hiller Corporation  
Stratos Division, Orinoco Drive  
Bay Shore, Long Island, New York  
Attention: Library

Ford Instrument Company  
32-36 47th Avenue  
Long Island City, New York  
Attention: A. Medica  
Library

The Garrett Corporation  
AiResearch Manufacturing Company  
9851-9951 Sepulveda Boulevard  
Los Angeles, California 90009  
Attention: Library

General Atomic Division  
P. O. Box 608, San Diego, California  
Attention: L. Perry  
Library

General Dynamics Corporation  
P. O. Box 748, Fort Worth 1, Texas  
Attention: Library

General Electric Company  
Missile and Space Division  
Cincinnati, Ohio 45215  
Attention: R. Brooks

General Electric Company  
Missile and Space Division  
P. O. Box 8555, Philadelphia 1, Pennsylvania  
Attention: E. Ray  
Library

General Electric Company  
Special Purpose Nuclear System Operations  
Vallecitos Atomic Laboratory  
P. O. Box 846, Pleasanton, California  
Attention: D. Francis  
Library

General Instrument Company  
65 Gouverneur Street  
Newark 4, New Jersey  
Attention: M. Barmat

Geoscience Limited  
410 S. Adros Avenue  
Solana Beach, California  
Attention: H. F. Poppendiek  
Library

IIT Research Institute  
10 West 35th Street  
Chicago, Illinois 60616  
Attention: Library

Lockheed Missiles & Space Division  
P. O. Box 504, Sunnyvale, California  
Attention: Library

S. V. Manson and Company, Inc.  
2420 Wilson Boulevard  
Arlington, Virginia 22201  
Attention: S. V. Manson

Martin-Nuclear Division  
Martin-Marietta Corporation  
P. O. Box 5042, Middle River 3, Maryland  
Attention: W. J. Levedahl  
Dr. W. Bienert  
Library

MSA Research Corporation  
Callery, Pennsylvania 16024  
Attention: Library

North American Aviation, Inc.  
Parker-Dwyne Division  
6633 Canoga Avenue  
Canoga Park, California  
Attention: Library

Radio Corporation of America  
Electron Tube Division  
Lancaster, Pennsylvania 17604  
Attention: F. Block  
Library

Radio Corporation of America  
Astro Electronics Division  
Box 800, Princeton, New Jersey 08540  
Attention: Harold Strickberg

Republic Aviation Corporation  
Farmingdale, Long Island, New York  
Attention: A. Schock  
Library

Space Dynamics Corporation  
Plasmajet Systems Division  
2215 Florence Avenue  
Cincinnati, Ohio  
Attention: Library

Space Technology Laboratories, Inc.  
One Space Park  
Redondo Beach, California  
Attention: B. Marcus  
Library

TRW, Inc.  
23555 Euclid Avenue  
Cleveland, Ohio 44117  
Attention: A. Koestel  
Library

Thermo Electron Engineering Corporation  
85 First Avenue  
Waltham 54, Massachusetts  
Attention: R. Howard

Westinghouse Electric Corporation  
Astronuclear Laboratory  
P. O. Box 10864  
Pittsburgh, Pennsylvania 15236  
Attention: Library